ISBN 0208 189X (print)
ISSN 1736-7492 (electronic)

Oil Shale

CONTENTS

2026 V.43 N.1

Tallinn 2026

Open access journal of
the Estonian Academy of Sciences
published in collaboration with
Tallinn University of Technology
and the Estonian University of Life Sciences

Published since 1984

OIL SHALE 2026, Vol. 43, No. 1

Abstracted/indexed in Science Citation Index Expanded (Web of Science), Current Contents – Engineering, Computing & Technology (Web of Science), Scopus, EBSCO, The Gale Group Inc., ProQuest LLC, Airiti Inc., Scilit, Directory of Open Access Journals (DOAJ)

Full texts available at www.eap.ee/oilshale

Executive Editor: Hedi Tõnso, hedi.tonso@eap.ee
Copyeditor: Kadri Põdra
Layout: Ulla Säre
Consultant: Peet M. Sööt (USA), peet@cmmenergy.com

The journal is published quarterly

Printed by Alfapress OÜ, Reti tee 8, 75312 Peetri, Estonia

Oil Shale, 2026, 43, 1, 1–30 https://doi.org/10.3176/oil.2026.1.01

Environmental advantages of oil shale ash as a secondary raw material: a focus on dioxin levels

Mari-Liis Ummik*, Oliver Järvik, Alar Konist

Department of Energy Technology, Tallinn University of Technology, Ehitajate tee 5, 19086 Tallinn, Estonia

Received 6 June 2025, accepted 23 January 2026, available online 29 January 2026

Abstract. *Secondary raw materials, such as ashes from the combustion of various fuels, are frequently used as alternatives to virgin raw materials. Among these, oil shale ash, a residue from oil shale power production and the shale oil industry, presents significant potential for use in sectors such as construction and agriculture. However, these materials might contain hazardous substances, such as dioxins, which are by-products of thermal treatment and other industrial processes. To date, the dioxin content in oil shale ash has been insufficiently examined. This article provides a comprehensive analysis of the dioxin content in oil shale ash from both a pilot unit and full-scale facilities. Additionally, the study compares the dioxin concentrations in oil shale ash with those in other types of ash and evaluates compliance with regulatory limits. The results showed that dioxin concentrations in the ash were below the limit of detection, regardless of the combustion technology, plant capacity, use of supplementary fuels, or utilisation of wastewater. The findings contribute new knowledge by highlighting the environmental advantages of oil shale ash as a secondary raw material, particularly due to its comparatively lower dioxin content relative to other types of ash.*

Keywords: *oil shale ash, secondary raw material, dioxins, PCDD, PCDF, PCB.*

1. Introduction

The world population has increased rapidly in the last five decades, reaching over 8.2 billion in 2025 and causing massive demand for natural resources [1]. With limited resources and a growing population, the linear business model (produce, use, dispose) is not sustainable. In 2020, the European Commission adopted the new Circular Economy Action Plan (CEAP) [2]. The main principles of the circular economy are sustainable production and consumption. The CEAP ensures that waste is prevented and that resources are used fully

---

* Corresponding author, mariliis.ummik@taltech.ee

and for as long as possible. Finally, waste that cannot be prevented is recycled and used instead of virgin materials.

In the energy sector, combustion processes – whether from fossil fuels, biomass, or waste incineration – produce significant quantities of ash and gas-cleaning residues. These by-products have traditionally been treated as waste, but growing research has focused on how they can be recovered and repurposed [3–10]. Combustion residues can be used as construction materials [11], as sources for extracting valuable elements [4], as soil amendment components [12], or as fertilisers [13]. By converting these residues into useful products, the demand for virgin raw materials can be reduced, supporting a more circular economy. In 2023, the American Coal Ash Association [14] reported that the United States generated 66.7 million tonnes of coal combustion residues, with 69% of that beneficially recovered – a sign of progress toward more sustainable waste management.

While waste recovery offers clear environmental benefits, it also raises concerns, as several toxic compounds are produced in combustion processes. Pollution is one of the triple planetary crises, along with climate change and biodiversity loss, so it is crucial to achieve a circular economy without generating hazardous pollutants.

Dioxins represent a category of persistent organic pollutants (POPs) [15] of particular concern in the context of waste management, especially regarding the residues generated from waste incineration. Even at lower concentrations than those found in waste incineration residues, dioxins can also form during the combustion of traditional fuels such as biomass, coal, and oil shale.

The formation of dioxins in combustion systems occurs primarily through two mechanisms: *de novo* and precursor pathways. *De novo* formation is regarded as the dominant route at post-combustion temperatures between 200–400 °C. In this process, dioxins are generated from unburned carbonaceous material such as soot or fly ash through oxidation and chlorination on particle surfaces in the presence of oxygen, chlorine, and metal catalysts. This heterogeneous mechanism is highly sensitive to temperature, fuel composition, and the availability of chlorine species [16, 17].

In contrast, the precursor pathway involves the transformation of chemically related compounds such as chlorophenols and chlorobenzenes. These compounds undergo condensation and subsequent reactions either in the gas phase or on particle surfaces, leading to the formation of polychlorinated dibenzo-*p*-dioxins (PCDDs) and dibenzofurans (PCDFs). Both mechanisms can occur simultaneously and independently in different regions of the combustion system. At higher temperatures (500–800 °C), homogeneous gas-phase reactions dominate, but overall dioxin formation is greatly reduced compared with the cooler post-combustion zone, where conditions strongly favour *de novo* synthesis [17].

The term ‘dioxins’ is a general term used to describe 75 polychlorinated PCDDs, 135 PCDFs, and sometimes also 209 polychlorinated biphenyls

(PCBs) [18]. Not all dioxin congeners are considered toxic; so far, 10 PCDFs, 7 PCDDs, and 12 PCBs out of the 419 dioxin congeners have been recognised by the World Health Organisation (WHO) as having toxic effects on humans [19]. The congeners of dioxins exhibit varying toxic effects.

The International Toxic Equivalency Factor (I-TEF) system, established in the late 1980s, was an early method to assess the toxicity of dioxins and furans by assigning toxic equivalency factors (TEFs) to various congeners relative to 2,3,7,8-tetrachlorodibenzodioxin (2,3,7,8-TCDD), the most toxic dioxin. Within this system, the overall toxic equivalent (TEQ) is calculated by multiplying the concentration of each congener by its assigned TEF and summing the results across all congeners. In 1998, and again in 2005, the WHO updated this approach, resulting in the WHO (2005) TEQ system (see Table 1). This revision incorporated new scientific data, leading to adjustments in TEFs for certain congeners and the inclusion of dioxin-like PCBs. Consequently, the WHO (2005) TEQ provides a more comprehensive assessment of toxicity by considering a broader range of compounds and reflecting updated toxicological understanding [19, 20]

Studies have shown that TEQ values calculated using the WHO (2005) TEFs can be approximately 20% lower than those calculated with the older I-TEQ system, due to the revised TEFs and the inclusion of additional compounds [21]. In 2022, the WHO reviewed and updated the TEF values, further refining the toxicity assessment framework [22].

Table 1. Summary of toxic equivalency factors (TEFs) [22–24]

Compound	**I-TEF**	**1998 WHO-TEF**	**2005 WHO-TEF**	**2022 WHO-TEF**
Dioxins				
2,3,7,8-TCDD	1	1	1	1
1,2,3,7,8-PeCDD	0.5	1	1	0.4
1,2,3,4,7,8-HxCDD	0.1	0.1	0.1	0.09
1,2,3,6,7,8-HxCDD	0.1	0.1	0.1	0.07
1,2,3,7,8,9-HxCDD	0.1	0.1	0.1	0.05
1,2,3,4,6,7,8-HpCDD	0.01	0.01	0.01	0.05
OCDD	0.001	0.0001	0.0003	0.001
Furans				
TCDF	0.1	0.1	0.1	0.07
1,2,3,7,8-PeCDF	0.05	0.05	0.03	0.01
2,3,4,7,8-PeCDF	0.5	0.5	0.3	0.1

Continued on the next page

Table 1. *Continued*

Compound	I-TEF	1998 WHO-TEF	2005 WHO-TEF	2022 WHO-TEF
1,2,3,4,7,8 HxCDF	0.1	0.1	0.1	0.3
1,2,3,6,7,8-HxCDF	0.1	0.1	0.1	0.09
1,2,3,7,8,9-HxCDF	0.1	0.1	0.1	0.2
2,3,4,6,7,8-HxCDF	0.1	0.1	0.1	0.1
1,2,3,4,6,7,8-HpCDF	0.01	0.01	0.01	0.02
1,2,3,4,7,8,9-HpCDF	0.01	0.01	0.01	0.1
OCDF	0.001	0.0001	0.0003	0.002
Non-ortho-substituted PCBs				
3,3’,4,4’-tetraCB (PCB77)		0.0001	0.0001	0.0003
3,4,4’,5-tetraCB (PCB81)		0.0001	0.0003	0.006
3,3’,4,4’,5-pentaCB (PCB126)		0.1	0.1	0.05
3,3’,4,4’,5,5’-hexaCB (PCB169)		0.01	0.03	0.005
Mono-ortho-substituted PCBs				
2,3,3’,4,4’-pentaCB (PCB105)		0.0001	0.00003	0.00003
2,3,4,4’,5-pentaCB (PCB114)		0.0005	0.00003	0.00003
2,3’,4,4’,5-pentaCB (PCB118)		0.0001	0.00003	0.00003
2’,3,4,4’,5-pentaCB (PCB123)		0.0001	0.00003	0.00003
2,3,3’,4,4’,5-hexaCB (PCB156)		0.0005	0.00003	0.00003
2,3,3’,4,4’,5’-hexaCB (PCB157)		0.0005	0.00003	0.00003
2,3’,4,4’,5,5’-hexaCB (PCB167)		0.00001	0.00003	0.00003
2,3,3’,4,4’,5,5’-heptaCB (PCB189)		0.0001	0.00003	0.00003

Oil shale is a sedimentary rock, with over 600 known deposits worldwide. However, only 33 countries have deposits that are considered to have potential economic value. The estimation of oil shale resources is typically expressed in terms of barrels of oil, indicating how much oil can be extracted from the rock. Estimates suggest that there are between 5 and 6 trillion barrels (760–960 billion cubic metres) of shale oil, of which approximately 1.0 to 1.6 trillion barrels (160–300 billion cubic metres) may be technically recoverable. The largest oil shale resources are concentrated in a few key countries. The United States holds the most significant reserves, estimated at around 6 trillion barrels, followed by China with 330 billion barrels, Russia with 270 billion barrels, and Israel with 250 billion barrels. Jordan and the Democratic Republic of the Congo each possess approximately 100 billion barrels, while Estonia has an estimated 16 billion barrels [25–27].

Oil shales can be classified using various methods. Hutton [27] categorises them into three groups based on their depositional environment: terrestrial, lacustrine, and marine. Marine oil shales are further classified by location into marinite, tasmanite, and kukersite. Alternatively, Tissot and Welte [28] classify oil shales based on their organic matter, specifically kerogen, using its hydrogen-to-carbon (H/C) and oxygen-to-carbon (O/C) ratios. The Van Krevelen diagram is introduced to distinguish between type I, type II, and type III kerogens. The oil shale found in Estonia is sometimes also referred to as type II, close to type I, and it is called kukersite. Kukersite has a high content of hydrogen and oxygen, a low nitrogen content, and significant amounts of organic sulphur and chlorine [29, 30].

In Estonia, oil shale is used in power plants to produce electricity and heat, and in the shale oil industry, where the rock is pyrolysed (i.e. thermally treated at around 500 °C in the absence of oxygen) to produce oil. During shale oil production, retort gas is also produced, which serves as a fuel in power plants. Retort gas primarily consists of light hydrocarbons, hydrogen, carbon monoxide, and carbon dioxide [31]. In Estonia, power production and shale oil production generate about 5 million tonnes of ash per year [32], although in the past it has been twice as much.

The oil shale ash generated in Estonia has been very well studied [11, 33–39] and it has great potential as a raw material. One of the main characteristics of oil shale ash is its pozzolanic and latent hydraulic properties, which make it a suitable substitute for conventional cementitious materials [40]. Studies have shown that oil shale ash-based concrete can achieve compressive strengths of up to 25 MPa within 28 days, making it a viable material for low-strength concrete applications and backfilling in mining operations [41, 42]. Furthermore, oil shale ash-based concrete has exhibited enhanced water resistance and reduced expansion, particularly when circulating fluidised bed (CFB) ash with a higher active silica content is incorporated [40].

In addition to its use in concrete, oil shale ash has been proven to be an effective material for road construction and soil stabilisation. Studies of road sections constructed with oil shale ash have shown improved soil strength and reduced settlement, particularly in peat-rich environments [43]. In addition, oil shale ash has been tested as a soil amendment for acidic peatlands, where its alkaline properties help to raise soil pH, improving nutrient availability for plants [44]. The granulated form of oil shale ash has also been investigated to control the mobility of potentially hazardous elements, with results indicating minimal leaching of heavy metals such as cadmium (Cd), mercury (Hg), and lead (Pb) under controlled conditions [45]

Dioxin content can be a limiting factor when it exceeds regulatory limits, rendering the ash material unsuitable for recovery or further use. Dioxins are classified as unintentional POPs under the Stockholm Convention [15]. The Stockholm Convention requires the destruction of POPs wastes and bans the recycling of wastes contaminated with POPs. Low POPs content levels define whether certain wastes should be categorised as POPs waste or not. In the general technical guidelines on the environmentally sound management of wastes consisting of, containing or contaminated with persistent organic pollutants [46] the low POPs content levels are set. The current low POPs content for PCDD/PCDFs is up to 15 μg TEQ/kg, while the discussion is still ongoing, with several stakeholders requesting the value to be 5 μg TEQ/kg or even 1 μg TEQ/kg [47].

The EU has established stringent regulations to control the presence of dioxins and other POPs in materials such as waste and ash, particularly under the EU POPs Regulation [48] and the EU Fertilisers Regulation [49]. These regulations set specific concentration limits for dioxins to ensure the protection of human health and the environment. Any waste, including ash, that exceeds 5 μg TEQ/kg total dioxin content cannot be recovered and must be disposed of in a controlled manner. The dioxin threshold for fertilising materials is even stricter. Specifically, for Component Material Category (CMC) 15, which includes ashes, the regulation stipulates the concentration limit for PCDDs/PCDFs at 20 ng TEQ/kg dry matter.

The generation of dioxins in the oil shale industry was investigated 20 years ago [50, 51]. The results showed that most of the dioxin congeners in oil shale fly ash were below the detection limit, indicating that the dioxins were not a cause for concern. However, the oil shale industry has changed significantly over the past 20 years. New technologies have been introduced, and the focus has shifted from power production to shale oil production. Oil shale is often co-combusted with biomass or with the retort gas from the shale oil industry. A thorough research study was conducted to evaluate the dioxin content across different fractions of oil shale ash and to assess the potential influence of the technologies utilised in its production. In this study, PCDDs, PCDFs, and PCBs refer to those congeners listed in the EU POPs Regulation. The term ‘dioxin’ is used here as a general term to describe these PCDDs, PCDFs, and PCBs.

2. Methods and materials

2.1. Samples from pilot unit

Dioxin content in oil shale ash, as well as in the flue gas, was investigated in a 60 kW_{th} CFB pilot unit. A detailed description of the pilot unit is given by Baqain et al. [52]. Figure 1 shows a schematic of the pilot unit, including ash sampling points.

The combustion process was carried out under conditions comparable to those of the Enefit280 shale oil plant, where semi-coke is incinerated in a circulating fluidised bed combustion (CFBC) boiler. Since semi-coke alone was unable to sustain stable combustion due to its relatively low calorific value, co-firing with oil shale was employed to enhance the overall energy

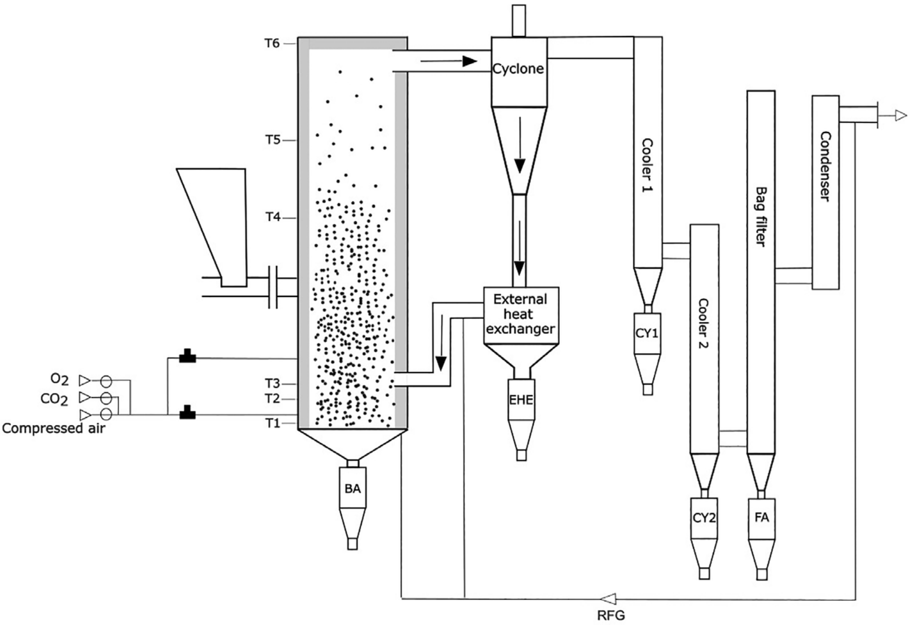

Fig. 1. Schematic of the 60 kW_{th} circulating fluidised bed pilot unit, including temperature measurement points (T1–T6) and ash sampling points: bottom ash (BA), ash from the external heat exchanger (EHE), cyclone ash (CY1 and CY2), and ash from the bag filter (FA) (adapted from [52]). RFG – recycled flue gas.

input. The fuel blend, consisting of semi-coke and oil shale in a mass ratio of 4:1, was combusted for five hours. The elemental composition of the fuel is shown in Table 2. Ash samples were collected from different collection points, as shown in Figure 1. Samples were taken several times during the process to obtain an average sample for each collection point. The combustion chamber operating temperatures, which are critical for evaluating co-firing performance and ash behaviour, are summarised in Table 3.

Table 2. Elemental composition of the oil shale fuel mixture (oil shale + semi-coke) used in the incineration test, wt%

C	H	S	Inorganic C	Organic C
8.22	0.62	0.82	3.01	6.13

Table 3. Measured temperatures (°C) at different heights in the combustion chamber

T1 0.11 m	T2 0.9 m	T3 1.17 m	T4 2.145 m	T5 3.22 m	T6 4.37 m	T (EHE)
658–663	653–656	661	699–674	699–763	753–797	579–581

Dioxin samples from the flue gas were collected isokinetically by experts from the Estonian Environmental Research Centre. The dioxins were captured using a heated sampling probe. Solid particles were separated from the sample using a glass fibre plane filter located at the outlet of the heated sampling probe. After passing through the filter, the gas flowed through a spiral cooler and the XAD2 adsorbent column, which captured contaminants in the gas phase. After passing through the XAD2, the gas was dried and then routed to a gas clock to determine its volume.

The sample was collected on the pre-filter, the XAD2 adsorbent, and in the washing solution. To obtain the washing solution, the gas path passing through the equipment was cleaned afterwards. The total amount of compounds per sample was obtained as a result of the analysis. When calculating the concentration, the mass obtained was divided by the gas volume measured using the gas clock.

2.2. Samples from full-scale facilities

Oil shale ash was collected from the installations of the main oil shale users. The covered plants were Auvere Power Plant (Auvere PP), the pulverised combustion (PC) unit and the CFB unit of Eesti Power Plant (Eesti PP), and the shale oil production installations Enefit280, Enefit140, and Petroter. At least two different ash samples were collected from each installation. In total, twenty ash samples were analysed for dioxin content (see Table 4). A detailed description of the technologies and ashes produced in the Estonian oil shale industry can be found in an article by Ummik et al. [53].

In shale oil plants, oil shale ash is produced when a mixture of semi-coke and recirculated ash (solid heat carrier) from the retort is combusted in either a lift-pipe combustor (used in the Enefit140 and Petroter technologies) or CFB combustor (used in the Enefit280 technology). This means that the ash originates from oil shale. In oil shale power plants, retort gas from shale oil production or biomass is co-combusted with oil shale. Pyrolytic wastewater originating from shale oil production (Enefit140 and Enefit280) is also sometimes incinerated in power plant boilers [54]. To better understand whether these additional fuels or pyrolytic wastewater might affect dioxin formation, ashes generated under different conditions were investigated.

Ash from the Auvere PP CFB boiler was collected during the co-combustion of oil shale, retort gas, and biomass (wood chips). The boiler has a gross electrical capacity of 305 MW_e and was operating at 233 MW_e during sampling. The fuel mix was based on heat input as follows: 60% oil shale, 30% retort gas, and 10% biomass. Ash samples were collected from three locations: the bottom of the boiler (bottom ash, BA), the first field of the electrostatic precipitator (ESP), and the fabric filter (FF).

In the Eesti PP CFB unit, oil shale and retort gas were co-combusted at a heat input ratio of 50% oil shale and 50% retort gas. The boiler operated at

Table 4. Characteristics of plants and ash samples used in the study

Sample	**Sample collection area**	**Technology**	**Rated capacity (gross), MW$_e$**	**Capacity during sampling, MW$_e$**	**Fuel mix (based on heat input)**	**Waste-water, t/h**
Auvere PP BA	Bottom of the boiler	Power plant, CFBC	305	233	Oil shale 60%, biomass 10%, retort gas 30%	0
Auvere PP ESP	Electrostatic precipitator (ESP)					
Auvere PP FF	Fabric filter (FF)					
Eesti PP PC BA	Bottom of the boiler	Power plant, PC	185–195	165	Oil shale 20%, retort gas 80%	0, 8, 16
Eesti PP PC FF	FF		185–195	165		
Eesti PP CFBC BA	Bottom of the boiler	Power plant, CFBC	215	215	Oil shale 50%, retort gas 50%	0, 8, 16
Eesti PP CFBC FF	FF		215	215		
Enefit280 CY	Cyclone (CY)	Shale oil plant, SHC + CFBC			Oil shale 100%	0
Enefit280 ESP	ESP					
Enefit140 total	Bunker of total ash	Shale oil plant, SHC + lift-pipe combustor			Oil shale 100%	0
Enefit140 ESP	ESP					
Petroter CY	CY	Shale oil plant, SHC + lift-pipe combustor			Oil shale 100%	0
Petroter ESP	ESP					

Abbreviations: PP – power plant, BA – bottom ash, CFBC – circulating fluidised bed combustion, PC – pulverised combustion, SHC – solid heat carrier, FF – fabric filter ash, ESP – electrostatic precipitator ash, CY – cyclone ash.

full capacity, i.e. 215 MW$_e$. Ash samples were collected from the bottom of the boiler (BA) and the first field of the ESP. Additionally, ash samples were collected when pyrolytic wastewater was added to the boiler at mass flow rates of 8 t/h and 16 t/h. The composition and characteristics of the pyrolytic wastewater are described in detail by Konist et al. [54].

In the Eesti PP PC unit, oil shale and retort gas were co-combusted, with oil shale accounting for 20% of the heat input and retort gas accounting for 80%. The boiler operated at a capacity of 165 MW_e, slightly below its full capacity of 185–195 MW_e. Ash samples were collected from the bottom of the boiler (BA) and from the novel integrated desulphurisation (NID) fabric filter (FF). Additionally, ash samples were collected when pyrolytic wastewater was added to the boiler at mass flow rates of 8 t/h and 16 t/h.

Ashes from the Enefit280 and Petroter shale oil production units were collected from the cyclone (CY) and the ESP. As with the Enefit140 unit, ash was collected from the total ash bunker and the ESP.

2.3. Dioxin analysis

The concentrations of seven PCDDs, ten PCDFs, and twelve PCBs listed in the EU POPs Regulation were analysed at the accredited ALS Laboratory in the Czech Republic. The quantification of tetra- to octa-chlorinated dioxins and furans was carried out using the isotope dilution technique HRGC-HRMS (high-resolution gas chromatography/high-resolution mass spectrometry), in accordance with the US EPA 1613B and ČSN EN 16190 standards. Similarly, PCBs were quantified using HRGC-HRMS in accordance with the ČSN EN 1948-4+A1 and US EPA TO-4A standards. A detailed description of the analysis can be found in Ummik et al. [55].

For PCDDs/PCDFs, the limit of detection (LOD) was defined as the concentration corresponding to a signal-to-noise ratio (S/N) ≥ 3, while the limit of quantification (LOQ) was set at twice the detection limit. In contrast, for PCBs, the LOQ was established on the basis of the blank level, and the LOD was similarly defined using an S/N ≥ 3 criterion. In most cases, concentrations were reported as the LOQ; however, for certain PCB congeners, results were only available at the LOD level. Measurement uncertainty was estimated at approximately 30% for individual congeners, with values validated through the analysis of certified reference materials under reproducibility-controlled conditions.

The dioxin concentrations presented in this study are based on dry weight and expressed in ng/kg and ng TEQ/kg. All dioxin concentrations expressed in ng TEQ/kg were calculated in accordance with the POPs Regulation [48], using the TEFs outlined therein. The TEF values in the EU POPs Regulation are identical to the 2005 WHO-TEFs [19]. To provide a conservative estimate of the potential maximum concentrations, the upper-bound approach [56] was applied, whereby all results below the LOQ are assumed to be equal to the LOQ value.

3. Results and discussion

3.1. Dioxins from oil shale pilot unit

There is a noticeable lack of information regarding the dioxin content of Estonian oil shale ashes. The only exception is a study by Roots [50], which focused on analyses conducted in 1998 of fly ash from the PC unit of Balti Power Plant. On average, oil shale organic matter contains 0.75% chlorine [29], an essential component for dioxin formation. Dioxins can form during any type of combustion process when carbon, chlorine, and oxygen are present. They form most readily within two temperature ranges: 500–800 °C and 200–400 °C [16, 17]. The temperature in a PC boiler can reach 1400 °C [36], meaning that dioxins form only when the ash cools. However, the temperature in a CFB boiler is approximately 800 °C [57], and the fly ash leaving the boiler is cooling along the gas passage, creating favourable conditions for dioxin formation.

The incineration conditions in the pilot unit closely mirrored those of the full-scale Enefit280 facility, particularly in terms of temperature distribution and oxygen concentration. This alignment supports the validity of extrapolating the results to full-scale operations. The temperature in the pilot unit was in the range of 579–797 °C, which is suitable for the formation of dioxins. However, all the measured dioxin congeners in both the ash samples and the flue gas were below the LOQ.

Although all measured dioxin congeners in the ash and flue gas samples were below the LOQ, this outcome does not confirm their complete absence. Even with state-of-the-art HRGC methods [58, 59], which can detect at the parts-per-trillion range [60], trace concentrations below quantifiable levels may still be present. This highlights an inherent limitation in dioxin analysis: analytical methods cannot guarantee absolute absence but can only establish that concentrations fall below a defined threshold of quantification. The use of the upper-bound approach offers a worst-case estimate of possible dioxin content in the samples. However, it should be noted that no official guidance currently supports this approach for waste or for secondary uses such as fertilisers.

Table 5 presents the concentrations of dioxin congeners in the oil shale ash from the pilot unit using the upper-bound approach. While this ensures a worst-case estimate, it also means that apparent variations between samples, or between the present results and previously published datasets, cannot be interpreted as true differences in dioxin content. Such discrepancies arise primarily from differences in LOQ values, which are influenced by matrix effects, background noise, and blank levels during analysis, rather than reflecting real changes in concentration.

Table 5. Dioxin content of the oil shale ash from the pilot unit calculated using the upper-bound approach, ng/kg DW

Ash sampling point	**BA**	**EHE**	**CY1**	**CY2**	**FA1**	**FA2**
PCB 105	180	160	220	93	120	150
PCB 114	7.5	13	3	2.1	8.1	16
PCB 118	770	650	950	760	750	510
PCB 123*	7.2	11	3.1	2.1	7	16
PCB 126	7.3	7	5.3	7.4	6.6	3.9
PCB 156	160	140	110	130	100	120
PCB 157*	12	16	26	9.7	7.7	20
PCB 167	71	59	74	24	62	52
PCB 169	8.8	11	11	8.6	7.8	2.2
PCB 170	150	170	330	150	220	250
PCB 180	460	430	560	350	490	420
PCB 189*	9.4	24	8.5	5.5	16	22
PCB 77	35	53	21	37	57	61
PCB 81	23	19	6.6	15	11	5.1
∑ PCB	1291	1163	1438	1094	1153	978
∑ TEQ PCB	**1.04**	**1.07**	**0.9**	**1.04**	**0.93**	**0.49**
1234678-HpCDD	2.7	3.7	2	2.3	2.3	1.8
1234678-HpCDF	2.4	4	4.4	2	2.6	5.6
123478-HxCDD	2.8	2.7	2.6	2.6	2.7	2.4
123478-HxCDF	1.8	1.9	1.5	1.6	1.4	1.2
1234789-HpCDF	5.5	18	2.9	2.8	16	6.5
123678-HxCDD	2	2	1.7	2.1	2.2	2
123678-HxCDF	1.9	1.8	1.4	1.5	1.2	1.2
12378-PeCDD	0.96	1.2	1.7	1.7	0.71	1.4
12378-PeCDF	1.4	1	1.5	1.5	1	1.1
123789-HxCDD	1.9	1.9	1.6	2	2.1	1.9
123789-HxCDF	3.7	3.2	1.6	2.3	6.6	2.5
234678-HxCDF	2.6	2.2	1.2	1.5	1.7	1.4
23478-PeCDF	1.8	1.4	1.3	1.5	1.8	1.4
2378-TCDD	0.58	0.64	1	0.72	0.58	0.84
2378-TCDF	1.3	0.79	0.89	0.86	1	2.2

Continued on the next page

Table 5. *Continued*

Ash sampling point	**BA**	**EHE**	**CY1**	**CY2**	**FA1**	**FA2**
OCDD	7.4	15	23	4.9	7.1	2.7
OCDF	5.7	11	1.8	3.8	5.5	6.4
∑PCDD	10.9	12.1	10.6	11.4	10.6	10.3
∑PCDF	28.1	45.29	18.49	19.36	38.8	29.5
∑ TEQ PCDD	**2.23**	**2.53**	**3.31**	**3.11**	**2.01**	**2.90**
∑ TEQ PCDF	**1.79**	**1.66**	**1.16**	**1.32**	**1.94**	**1.43**
∑ TEQ dioxins	**5.07**	**5.27**	**5.38**	**5.47**	**4.90**	**4.80**

* Limit of detection was used instead of limit of quantification.
Abbreviations: BA – bottom ash, EHE – external heat exchanger ash, CY – cyclone ash, FA – bag filter ash, TEQ – toxic equivalent.

As EU air emission regulations such as the Industrial Emissions Directive [61] and the Best Available Technique for Large Combustion Plants [62] only cover PCDDs and PCDFs, PCBs were not measured. The dioxin concentrations in the flue gas were below the detection limit (see Table 6), indicating that dioxins are not forming during oil shale combustion.

Table 6. Dioxin content in the flue gas, pg/Nm^3

Compound	**Concentration**
2378-TCDD	< 1.92
12378-PeCDD	< 2.35
123478-HxCDD	< 4.32
123678-HxCDD	< 4.32
123789-HxCDD	< 4.32
1234678-HpCDD	< 4.32
OCDD	< 10.32
2378-TCDF	< 9.38
12378-PeCDF	< 3.89
23478-PeCDF	< 3.89
123478-HxCDF	< 4.64
123678-HxCDF	< 4.64
123789-HxCDF	< 4.64
234678-HxCDF	< 4.64
1234678-HpCDF	< 6.10
1234789-HpCDF	< 6.10
OCDF	< 7.51

3.2. Total dioxin content analysis from full-scale facilities

While the incineration conditions in the pilot unit were similar to those of the full-scale Enefit280 facility, the resulting pollutant concentrations may not be entirely representative. This discrepancy primarily arises from physical differences, particularly in the size of the combustion chambers and the gas flow pathways. In the full-scale facility, the larger gas passage results in a longer residence time for the flue gases, facilitating a slower cooling rate of the ash. This extended cooling period may promote the formation of dioxins, potentially resulting in higher concentrations than those observed under pilot-scale conditions.

To evaluate the influence of combustion temperature and technology on dioxin formation under real conditions, ash samples were collected from various operating oil shale plants and subsequently analysed. The concentrations of dioxin congeners in all samples were found to be below the analytical detection limits (Appendices 1 and 2). This correlates with the pilot tests but differs from the findings reported by Roots [50]. According to Roots' study, the total concentrations of PCDDs, PCDFs, and PCBs in one fly ash sample were 32 ng/kg, 26 ng/kg, and 2400 ng/kg, respectively. A second sample from the same study showed lower concentrations. However, it was not specified which dioxin congeners were included in the total concentrations. Of the dioxin congeners considered toxic, only four were above the detection limit in Roots' study: OCDD, 1,2,3,4,6,7,8-HpCDD, 2,3,4,6,7,8-HxCDF, and 1,2,3,4,6,7,8-HpCDF. Even though they were present in very low concentrations and the congeners had low TEF values, their presence indicates that oil shale fly ash contained trace levels of toxic dioxins in 1998.

The absence of detectable dioxin congeners in the current study may be due to technological advancements. In 1998, PC technology was used, and fly ash was collected from electrostatic precipitators (ESPs). Today, PC units are equipped with NID units, and the fly ash is collected from fabric filters. As Roots' study [50] did not provide detailed information on ash formation conditions or collection methods, it is not possible to make a direct comparison of the conditions influencing dioxin formation in the two studies.

The current study thoroughly investigated ash samples to determine whether different conditions could affect dioxin formation. Ash was collected from power plants operating at varying capacities. While partial capacities compared to nominal have been shown to influence the mineral decomposition, the particle-size distribution, and bulk density of ash [36], this variation did not affect the dioxin content.

In Estonian oil shale power plants, oil shale is co-combusted with biomass and/or retort gas. According to Ummik et al. [55], the chlorine content in biomass ranges from 0.006% to 0.016%, which is generally lower than that of oil shale. Retort gas from oil shale pyrolysis contains no measurable chlorine [31]. Given the low chlorine content of these supplementary fuels, their influence on dioxin formation is unlikely – a conclusion supported by our results (Table 5).

In oil shale power plants, wastewater generated during shale oil production is utilised by injecting it into the combustion chamber, facilitating its elimination through thermal degradation. Although water does not directly form or eliminate dioxins, it can affect their formation. Li et al. [63] observed that at higher temperatures, the presence of moisture can promote dioxin formation. In this study, the addition of water to the oil shale combustion process increased the flue gas moisture content by approximately 0.7–2.8%, a relatively modest rise. Under these conditions, our findings showed that the increased moisture had no observable effect on dioxin formation. As presented in Table 7, the dioxin concentrations remained relatively consistent regardless of whether wastewater was added.

Table 7. Dioxin content in ash samples (upper-bound approach) in relation to plant capacity, fuel type, and wastewater addition

Sample	**Type**	**Rated capacity (gross), MW_e**	**Capacity during sampling, MW_e**	**Fuel**	**Wastewater, t/h**	**∑ dioxins, TEQ ng/kg DW**
Auvere PP BA	CFBC	305	233	Oil shale, biomass, retort gas	0	5.75
Auvere PP ESP						5.6
Auvere PP FF						5.81
Eesti PP PC BA	PC	185–195	165	Oil shale, retort gas	0	5.46
					16	5.69
Eesti PP BC FF	PC	185–195	165		0	5.44
					8	5.12
					16	5.44
Eesti PP CFBC BA	CFBC	215	215	Oil shale, retort gas	0	5.49
					8	5.69
					16	5.74
Eesti PP CFBC FF	CFBC	215	215		0	5.41
					8	5.31
					16	5.71
Enefit280 CY	SHC + CFBC			Oil shale	0	7.97
Enefit280 ESP						5.42
Enefit140 total	SHC			Oil shale	0	5.48
Enefit140 ESP						5.26
Petroter CY	SHC			Oil shale	0	4.93
Petroter ESP						5.23

Abbreviations: PP – power plant, BA – bottom ash, CFBC – circulating fluidised bed combustion, PC – pulverised combustion, SHC – solid heat carrier, FF – fabric filter ash, ESP – electrostatic precipitator ash, CY – cyclone ash, TEQ – toxic equivalent, DW – dry weight.

The results reveal that, even in the worst-case scenario, the total TEQ concentration of dioxins is around 5 ng TEQ/kg. The limit value for dioxins in the EU POPs Regulation is 5 µg TEQ/kg, which is 1000 times higher. The limit value in the EU Fertilisers Regulation is 20 ng TEQ/kg, which is also four times higher.

Oil shale ash contains significantly lower concentrations of dioxins than other combustion residues (see Table 8). Ash from municipal solid waste incineration (MSWI) has been found to contain high levels of dioxins, which vary widely depending on the incineration technology used, the pollution control devices employed, the chlorine content, and the operational conditions. TEQ levels for fly ash from MSWIs are high, reaching up to 2500 ng WHO (2005) TEQ/kg [64, 65]. Bottom ash typically contains lower concentrations of PCDDs/PCDFs than fly ash [65]. Biomass ashes, particularly fly ash, also exhibit higher dioxin TEQ values than oil shale ash, reaching up to 1139 ng TEQ/kg [66]. Ummik et al. [55] investigated biomass ashes from different biomass combustion plants using wood chips as fuel. While the dioxin content was generally below the detection limit, some fly ashes still had dioxin concentrations that exceeded the limit set for fertilisers in the EU [49]. PCDD/PCDF levels in fly ash from coal-fired power plants are reported to be significantly lower than in MSWI ash. Fly ash from a coal-fired power plant contained PCDD/PCDF levels ranging from 0.1 to 78 ng TEQ/kg [67]. Fly ash samples from coal and sewage sludge co-combustion contained dioxin levels between 1.32 and 5.78 ng TEQ/kg [68].

While chlorine is an essential component for dioxin formation, variations in fuel chlorine content alone cannot fully account for the observed patterns in dioxin concentrations. Oil shale typically contains around 0.75 wt% chlorine [29], yet its ashes show very low dioxin concentrations, suggesting that its mineral matrix and combustion conditions suppress dioxin formation. Wood, in contrast, has very low chlorine contents (0.001–0.006 wt% [55]), but its fly ashes may still contain elevated dioxin levels. Municipal solid waste is especially complex: its chlorine content is highly variable, depending on the waste origin [69], which partly explains the wide range of dioxin concentrations observed in MSWI residues. Coal occupies an intermediate position, with chlorine contents ranging from 0.01 wt% in low-rank coals up to 0.5 wt% or more in some bituminous coals, and occasionally above 1 wt% [70, 71]. Nevertheless, coal fly ash typically contains only 0.1–78 ng TEQ/kg, much lower than MSWI ashes.

Table 8. PCDD, PCDF, PCB, and total dioxin concentrations in different types of ashes

Fuel	**Sample ID**	**ng/kg**					**I-TEQ, ng/kg**			**TEQ (WHO 2005), ng/kg**				
		PCDD	**PCDF**	**∑PCCD/F**	**PCB**	**∑dioxin**	**PCDD**	**PCDF**	**∑PCCD/F**	**PCDD**	**PCDF**	**∑PCCD/F**	**PCB**	**∑dioxin**
Oil shale	Range current stay	22–275	21–103	43–378	269–2603	312–2981				2.37–3.97	0.65–1.72	3.02–5.69	0.63–1.18	3.65–6.87
MSW [64]	Chuzhou						35.9	95.8	131.7					
	Jilin						11.0	24.3	35.3					
	Zhengzhou						82.3	298.9	381.2					
	Zibo						109.4	453	562.4					
MSW [65]	BA			262	114				7.36			7.8	0.83	8.578
	SH			205	37.7				13.3			14.7	0.63	15.326
	HE			62851	1554				1210			1297	33.5	1330.5
	SDA			4306	154				99.4			107	3.09	110.09
	BF			27463	3097				981			1069	64.5	1133.5
	FAP			27185	1544				781			836	30.9	866.9

Continued on the next page

Table 8. *Continued*

Fuel	Sample ID	ng/kg					I-TEQ, ng/kg			TEQ (WHO 2005), ng/kg				
		PCDD	**PCDF**	**∑PCCD/F**	**PCB**	**∑dioxin**	**PCDD**	**PCDF**	**∑PCCD/F**	**PCDD**	**PCDF**	**∑PCCD/F**	**PCB**	**∑dioxin**
MSW [72]	FA1	51000	79000	130000	2300	132300								1800
	FA2	1100	1600	2700	95	2795								34
	FA3	59000	34000	93000	2900	95900								1000
	FA4	38000	24000	62000	1400	63400								710
	FA5	10000	31000	41000	500	41500								550
	FA6	28000	35000	63000	1700	64700								1000
	FA7	100000	73000	173000	9300	182300								2500
	FA8	39000	16000	55000	370	55370								560
	FA9	5600	4200	9800	210	10010								110
	FA10	20000	18000	38000	1900	39900								580
	FA11	26000	24000	50000	1500	51500								640
	FA12	10000	17000	27000	360	27360								440
Coal + 10% SS [68]	Coal FA	195.21	56.72	251.93			0.72	2.71	3.43					
	Coal BA	4.76	0.34	5.1			0.025	0.039	0.064					
Coal [67]	Coal FA	1.57	0.46	2.03						0.038	0.043	0.081		
	Coal boiler FA	334	439	773						32.1	46.3	78.4		
	Coal + wood BA	6.58	158	164						0.002	11.7	11.7		

Continued on the next page

Table 8. *Continued*

Fuel	Sample ID	ng/kg					I-TEQ, ng/kg			TEQ (WHO 2005), ng/kg				
		PCDD	**PCDF**	**∑PCCD/F**	**PCB**	**∑dioxin**	**PCDD**	**PCDF**	**∑PCCD/F**	**PCDD**	**PCDF**	**∑PCCD/F**	**PCB**	**∑dioxin**
Biomass [73]	Agric. residue FA											63	0.04	63.04
	Agric. residue BA/total											5.5	0.18	5.68
	Wood FA											121	25	146
	Wood BA/total											2.3	0.14	2.44
	Waste wood FA											3133		
	Waste wood BA/total											22	3	25
Biomass (woodchips) [55]	1 BA									6.15	8.19	14.34	5.11	19.45
	1 CY									11.38	15.99	27.37	1.8	29.17
	1 ESP									169.63	107.18	276.81	2.08	278.89
	4 BA									6.57	4.27	10.84	1.73	12.57
	4 CY									7.82	38.58	46.4	2.8	49.2
	5 BA									6.7	2.96	9.66	1.43	11.09
	5CY									12.68	4.32	17	2.44	19.44
	6BA									6.7	2.78	9.48	1.21	10.69
	6 CY									4.11	11.19	15.3	1.42	16.72
	8 BA									6.55	4.48	11.03	1.88	12.91
	8 ESP									78.99	45.98	124.97	1.48	126.45
Biomass (forest biomass residues) [66]	BFB1 BA	626.8	129	755.8					18.4			19.7		
	BFB1 FA	668	63	731					35.9			34.6		
	BFB4 BA	0	0	0					11.9			13.5		
	BFB4 FA	1504	1639	3143					224			207		
	GF BA	141	0	141					12.2			13.8		
	GF FA	19336	4716	24052					1144			1139		

Abbreviations: MSW – municipal solid waste, SS – sewage sludge, agric. – agricultural.

Conclusion

This article provides a comprehensive overview of the dioxin content in oil shale ash from various facilities and combustion conditions. Despite concerns about dioxins as hazardous by-products of combustion processes, this analysis found that dioxin concentrations in oil shale ash were below the detection limit and remained significantly lower than regulatory thresholds, even in a worst-case scenario using the upper-bound approach.

The study showed that for oil shale, the combustion technology and production scale – whether pilot-scale, partial load, or nominal capacity – had no discernible effect on dioxin formation in the resulting ashes. Likewise, the utilisation of pyrolytic wastewater and supplementary fuels such as biomass and retort gas did not influence dioxin concentrations.

Compared to other combustion residues such as municipal solid waste, biomass, and coal ash, oil shale ash demonstrates substantially lower levels of dioxins. In this study, the dioxin concentrations in oil shale ash were consistently below the limit of quantification, corresponding to around 5 ng TEQ/kg in a worst-case upper-bound estimate. For comparison, municipal solid waste fly ash can reach values up to 2500 ng TEQ/kg, biomass fly ash up to 1100 ng TEQ/kg, and coal fly ash typically ranges between 0.1 and 78 ng TEQ/kg. Given its low dioxin content, oil shale ash has significant potential for utilisation in the construction, agriculture, and resource recovery sectors without presenting any dioxin-related risks.

Data availability statement

Data are available from the authors upon request.

Acknowledgements

This article was supported by the Ministry of Climate of Estonia and the Estonian Research Council (project No. TEM-TA73). The publication costs of this article were partially covered by the Estonian Academy of Sciences.

References

1. UNEP (United Nations Environment Programme). *Global Resources Outlook 2024: Bend the Trend – Pathways to a Liveable Planet as Resource Use Spikes*. UNEP, 2024. https://www.unep.org/resources/Global-Resource-Outlook-2024 (accessed 2025-03-25).
2. European Commission. *A New Circular Economy Action Plan for a Cleaner and More Competitive Europe*. https://eur-lex.europa.eu/legal-content/EN/TXT/?qid=1583933814386&uri=COM:2020:98:FIN (accessed 2024-11-07).

3. Mary Joseph, A., Snellings, R., Nielsen, P., Matthys, S., De Belie, N. Pre-treatment and utilisation of municipal solid waste incineration bottom ashes towards a circular economy. *Construction and Building Materials*, 2020, **260**, 120485. https://doi.org/10.1016/J.CONBUILDMAT.2020.120485
4. Fernández-Pereira, C., Leiva, C., Luna-Galiano, Y., Vilches, L. F., Arroyo, F. Improved recycling of a gasification fly ash: an integrated waste management approach within the framework of a Circular Economy. *Waste Management*, 2024, **187**, 31–38. https://doi.org/10.1016/J.WASMAN.2024.06.029
5. Predeanu, G., Slăvescu, V., Bălănescu, M., Dorina Mihalache, R., Mihaly, M., Marin, A. C. et al. Coal bottom ash processing for capitalization according to circular economy concept. *Minerals Engineering*, 2021, **170**, 107055. https://doi.org/10.1016/J.MINENG.2021.107055
6. Marinina, O., Nevskaya, M., Jonek-Kowalska, I., Wolniak, R., Marinin, M. Recycling of coal fly ash as an example of an efficient circular economy: a stakeholder approach. *Energies*, 2021, **14**(12), 3597. https://doi.org/10.3390/EN14123597
7. Saldarriaga, J. F., Gaviria, X., Gene, J. M., Aguado, R. Improving circular economy by assessing the use of fly ash as a replacement of lime pastes reducing its environmental impact. *Process Safety and Environmental Protection*, 2022, **159**, 1008–1018. https://doi.org/10.1016/J.PSEP.2022.01.074
8. Quina, M. J., Bontempi, E., Bogush, A., Schlumberger, S., Weibel, G., Braga, R. et al. Technologies for the management of MSW incineration ashes from gas cleaning: new perspectives on recovery of secondary raw materials and circular economy. *Science of The Total Environment*, 2018, **635**, 526–542. https://doi.org/10.1016/J.SCITOTENV.2018.04.150
9. Nayak, D. K., Abhilash, P. P., Singh, R., Kumar, R., Kumar, V. Fly ash for sustainable construction: a review of fly ash concrete and its beneficial use case studies. *Cleaner Materials*, 2022, **6**, 100143. https://doi.org/10.1016/j.clema.2022.100143
10. Kumar, A., Abbas, S., Saluja, S. Utilization of incineration ash as a construction material: a review. *Materials Today: Proceedings*, 2023. https://doi.org/10.1016/j.matpr.2023.05.577
11. Usta, M. C., Yörük, C. R., Hain, T., Paaver, P., Snellings, R., Rozov, E. et al. Evaluation of new applications of oil shale ashes in building materials. *Minerals*, 2020, **10**(9), 765. https://doi.org/10.3390/MIN10090765
12. Demeyer, A., Voundi Nkana, J. C., Verloo, M. G. Characteristics of wood ash and influence on soil properties and nutrient uptake: an overview. *Bioresource Technology*, 2001, **77**(3), 287–295. https://doi.org/10.1016/S0960-8524(00)00043-2
13. Silva, F. C., Cruz, N. C., Tarelho, L. A. C., Rodrigues, S. M. Use of biomass ash-based materials as soil fertilisers: critical review of the existing regulatory framework. *Journal of Cleaner Production*, 2019, **214**, 112–124. https://doi.org/10.1016/J.JCLEPRO.2018.12.268

14. ACAA (American Coal Ash Association). *Coal Ash Recycling Rate Increased in 2023; Ash Harvesting Continued Rapid Growth*. ACAA, 2023. https://acaa-usa.org/wp-content/uploads/2025/05/News-Release-Coal-Ash-Production-and-Use-2023.pdf (accessed 2025-05-27).
15. Stockholm Convention. Stockholm Convention on Persistent Organic Pollutants (POPs) and Annexes Revised in 2019. Stockholm Convention, 2001. https://pops.int (accessed 2025-04-23).
16. Tame, N. W., Dlugogorski, B. Z., Kennedy, E. M. Formation of dioxins and furans during combustion of treated wood. *Progress in Energy and Combustion Science*, 2007, **33**(4), 384–408. https://doi.org/10.1016/j.pecs.2007.01.001
17. Stanmore, B. R. The formation of dioxins in combustion systems. *Combustion and Flame*, 2004, **136**(3), 398–427. https://doi.org/10.1016/j.combustflame.2003.11.004
18. Li, Z., Chen, L., Liu, S., Ma, H., Wang, L., An, C. et al. Characterization of PAHs and PCBs in fly ashes of eighteen coal-fired power plants. *Aerosol and Air Quality Research*, 2016, **16**(12), 3175–3186. https://doi.org/10.4209/AAQR.2016.10.0430
19. Van den Berg, M., Birnbaum, L. S., Denison, M., De Vito, M., Farland, W., Feeley, M. et al. The 2005 World Health Organization reevaluation of human and mammalian toxic equivalency factors for dioxins and dioxin-like compounds. *Toxicological Sciences*, 2006, **93**(2), 223–241. https://doi.org/10.1093/toxsci/kfl055
20. Barnes, D. G. Toxicity equivalents and EPA's risk assessment of 2,3,7,8-TCDD. *Science of The Total Environment*, 1991, **104**(1–2), 73–86. https://doi.org/10.1016/0048-9697(91)90008-3
21. Bhavsar, S. P., Reiner, E. J., Hayton, A., Fletcher, R., MacPherson, K. Converting Toxic Equivalents (TEQ) of dioxins and dioxin-like compounds in fish from one Toxic Equivalency Factor (TEF) scheme to another. *Environment International*, 2008, **34**(7), 915–921. https://doi.org/10.1016/J.ENVINT.2008.02.001
22. DeVito, M., Bokkers, B., van Duursen, M. B. M., van Ede, K., Feeley, M., Antunes Fernandes Gáspár, E. et al. The 2022 World Health Organization reevaluation of human and mammalian toxic equivalency factors for polychlorinated dioxins, dibenzofurans and biphenyls. *Regulatory Toxicology and Pharmacology*, 2024, **146**, 105525. https://doi.org/10.1016/J.YRTPH.2023.105525
23. Dyke, P. H., Stratford, J. Changes to the TEF schemes can have significant impacts on regulation and management of PCDD/F and PCB. *Chemosphere*, 2002, **47**(2), 103–116. https://doi.org/10.1016/S0045-6535(01)00219-3
24. Hong, B., Garabrant, D., Hedgeman, E., Demond, A., Gillespie, B., Chen, Q. et al. Impact of WHO 2005 revised toxic equivalency factors for dioxins on the TEQs in serum, household dust and soil. *Chemosphere*, 2009, **76**(6), 727–733. https://doi.org/10.1016/J.CHEMOSPHERE.2009.05.034
25. Knaus, E., Killen, J., Biglarbigi, K., Crawford, P. An overview of oil shale resources. In *Oil Shale: A Solution to the Liquid Fuel Dilemma* (Ogunsola, O. I.,

Hartstein, A. M., Ogunsola, O., eds). ACS Symposium Series, 2010, **1032**, 3–20. https://doi.org/10.1021/bk-2010-1032.ch001

26. Yihdego, Y., Salem, H. S., Kafui, B. G., Veljkovic, Z. Economic geology value of oil shale deposits: Ethiopia (Tigray) and Jordan. *Energy Sources, Part A: Recovery, Utilization, and Environmental Effects*, 2018, **40**(17), 2079–2096. https://doi.org/10.1080/15567036.2018.1488015
27. Dyni, J. R. Geology and resources of some world oil-shale deposits. *Oil Shale*, 2003, **20**(3), 193–252. https://doi.org/10.3176/oil.2003.3.02
28. Tissot, B. P., Welte, D. H. *Petroleum Formation and Occurrence*. Springer-Verlag, Berlin, Heidelberg, 1984. https://doi.org/10.1007/978-3-642-87813-8
29. Ots, A. Estonian oil shale properties and utilization in power plants. *Energetika*, 2007, **4**(2), 8–18.
30. Lille, Ü. Current knowledge on the origin and structure of Estonian kukersite kerogen. *Oil Shale*, 2003, **20**(3), 253–263. https://doi.org/10.3176/oil.2003.3.03
31. Nešumajev, D., Pihu, T., Siirde, A., Järvik, O., Konist, A. Solid heat carrier oil shale retorting technology with integrated CFB technology. *Oil Shale*, 2019, **36**(2S), 99–113. https://doi.org/10.3176/oil.2019.2S.02
32. Estonian Environment Agency. Waste statistics. https://tableau.envir.ee/views/Avalikud_pringud_2020-2022/Riigitasand?%3Aembed=y&%3Aiid=4&%3AisGuestRedirectFromVizportal=y (accessed 2023-12-19).
33. Kuusik, R., Uibu, M., Kirsimäe, K. Characterization of oil shale ashes formed at industrial-scale-CFBC boilers. *Oil Shale*, 2005, **22**(4), 407–419. https://doi.org/10.3176/oil.2005.4S.04
34. Usta, M. C., Yörük, C. R., Uibu, M., Hain, T., Gregor, A., Trikkel, A. CO_2 curing of Ca-rich fly ashes to produce cement-free building materials. *Minerals*, 2022, **12**(5), 513. https://doi.org/10.3390/MIN12050513
35. Bityukova, L., Mõtlep, R., Kirsimäe, K. Composition of oil shale ashes from pulverized firing and circulating fluidized-bed boiler in Narva thermal power plants, Estonia. *Oil Shale*, 2010, **27**(4), 339–353. https://doi.org/10.3176/oil.2010.4.07
36. Konist, A., Pihu, T., Neshumayev, D., Siirde, A. Oil shale pulverized firing: boiler efficiency, ash balance and flue gas composition. *Oil Shale*, 2013, **30**(1), 6–18. https://doi.org/10.3176/oil.2013.1.02
37. Ummik, M.-L., Järvik, O., Reinik, J., Konist, A. Ecotoxicity assessment of ashes from calcium-rich fuel combustion: contrasting results and regulatory implications. *Environmental Science and Pollution Research*, 2024, **31**, 48523–48533. https://doi.org/10.1007/s11356-024-34387-3
38. Arro, H., Pihu, T., Prikk, A., Rootamm, R., Konist, A. Comparison of ash from PF and CFB boilers and behaviour of ash in ash fields. *Proceedings of the 20th International Conference on Fluidized Bed Combustion*, 2009, 1054–1060. https://doi.org/10.1007/978-3-642-02682-9_164
39. Uibu, M., Tamm, K., Viires, R., Reinik, J., Somelar, P., Raado, L.-M. et al. The composition and properties of ash in the context of the modernisation of oil shale industry. *Oil Shale*, 2021, **38**(2), 155–176. https://doi.org/10.3176/oil.2021.2.04

40. Raado, L.-M., Hain, T., Liisma, E., Kuusik, R. Composition and properties of oil shale ash concrete. *Oil Shale*, 2014, **31**(2), 147–160. https://doi.org/10.3176/oil.2014.2.05
41. Uibu, M., Somelar, P., Raado, L.-M., Irha, N., Hain, T., Koroljova, A. et al. Oil shale ash based backfilling concrete – strength development, mineral transformations and leachability. *Construction and Building Materials*, 2016, **102**, 620–630. https://doi.org/10.1016/J.CONBUILDMAT.2015.10.197
42. Paaver, P., Järvik, O., Kirsimäe, K. Design of high volume CFBC fly ash based calcium sulphoaluminate type binder in mixtures with ordinary Portland cement. *Materials*, 2021, **14**(19), 5798. https://doi.org/10.3390/MA14195798
43. Reinik, J., Irha, N., Koroljova, A., Meriste, T. Use of oil shale ash in road construction: results of follow-up environmental monitoring. *Environmental Monitoring and Assessment*, 2018, **190**, 59. https://doi.org/10.1007/s10661-017-6421-5
44. Triisberg-Uljas, T., Vellak, K., Karofeld, E. Application of oil-shale ash and straw mulch promotes the revegetation of extracted peatlands. *Ecological Engineering*, 2018, **110**, 99–106. https://doi.org/10.1016/J.ECOLENG.2017.10.006
45. Reinik, J., Irha, N., Ots, K. Effect of Ca-rich granulated oil shale ash amendment on leaching properties of peat soil: experimental and field study. *Eurasian Soil Science*, 2021, **54**, 1097–1106. https://doi.org/10.1134/S1064229321070115
46. UNEP. *General Technical Guidelines on the Environmentally Sound Management of Wastes Consisting of, Containing or Contaminated with Persistent Organic Pollutants*. UNDP, 2023. https://www.basel.int/Implementation/TechnicalMatters/DevelopmentofTechnicalGuidelines/TechnicalGuidelines/tabid/8025/Default.aspx (accessed 2025-03-19).
47. Basel Convention on the Control of Transboundary Movements of Hazardous Wastes and their Disposal. Low POP content. https://www.basel.int/Implementation/POPsWastes/TechnicalGuidelines/LowPOPcontent/tabid/6360/Default.aspx (accessed 2025-01-29).
48. EU. Regulation (EU) 2019/1021 of the European Parliament and of the Council of 20 June 2019 on persistent organic pollutants. *Official Journal of the European Union*, 2019, L 169, 45–77.
49. EU. Regulation (EU) 2019/1009 of the European Parliament and of the Council of 5 June 2019 laying down rules on the making available on the market of EU fertilising products and amending Regulations (EC) No 1069/2009 and (EC) No 1107/2009 and repealing Regulation (EC) No 2003/2003. *Official Journal of the European Union*, 2019, L 170, 1–114.
50. Roots, O. Polychlorinated biphenyls (PCB), polychlorinated dibenzo-*p*-dioxins (PCDD) and dibenzofurans (PCDF) in oil shale and fly ash from oil shale-fired power plant in Estonia. *Oil Shale*, 2004, **21**(4), 333–339. https://doi.org/10.3176/oil.2004.4.06
51. Schleicher, O., Roots, O., Jensen, A. A., Herrmann, T., Tordik, A. Dioxin emission from two oil shale fired power plants in Estonia. *Oil Shale*, 2005, **22**(4S), 563–570. https://doi.org/10.3176/oil.2005.4s.15

52. Baqain, M., Yörük, C. R., Nešumajev, D., Järvik, O., Konist, A. Ash characterisation formed under different oxy-fuel circulating fluidized bed conditions. *Fuel*, 2023, **338**, 127244. https://doi.org/10.1016/J.FUEL.2022.127244
53. Ummik, M.-L., Tamm, K., Järvik, O., Nešumajev, D., Roosalu, K., Pihu, T. et al. Quantification of oil shale industry ash flows – their chemical and mineralogical composition. *Oil Shale*, 2025, **42**(2), 129–166. https://doi.org/10.3176/oil.2025.2.01
54. Konist, A., Järvik, O., Pikkor, H., Neshumayev, D., Pihu, T. Utilization of pyrolytic wastewater in oil shale fired CFBC boiler. *Journal of Cleaner Production*, 2019, **234**, 487–493. https://doi.org/10.1016/j.jclepro.2019.06.213
55. Ummik, M.-L., Järvik, O., Konist, A. Dioxin concentrations and congener distribution in biomass ash from small to large scale biomass combustion plants. *Environmental Science and Pollution Research*, 2024, **31**, 58946–58956. https://doi.org/10.1007/S11356-024-35141-5
56. EU. Commission Regulation (EU) 2017/644 of 5 April 2017 laying down methods of sampling and analysis for the control of levels of dioxins, dioxin-like PCBs and non-dioxin-like PCBs in certain foodstuffs and repealing Regulation (EU) No 589/2014. *Official Journal of the European Union*, 2017, L 92, 9–34.
57. Hotta, A., Parkkonen, R., Hiltunen, M., Arro, H., Loosaar, J., Parve, T. et al. Experience of Estonian oil shale combustion based on CFB technology at Narva power plants. *Oil Shale*, 2005, **22**(4S), 381–397. https://doi.org/10.3176/oil.2005.4s.02
58. Jo, J., Son, Y., Park, M.-K., Lee, J. Y., Chu, H., Ahn, Y. G. Statistical comparison for assessing agreement between two mass spectrometric methods for the analysis of polychlorinated dibenzo-*p*-dioxins and furans (PCDDs/Fs) in contaminated soils. *Chemosphere*, 2024, **363**, 142806. https://doi.org/10.1016/J.CHEMOSPHERE.2024.142806
59. Ábalos, M., Cojocariu, C. I., Silcock, P., Roberts, D., Pemberthy, D. M., Sauló, J. et al. Meeting the European Commission performance criteria for the use of triple quadrupole GC-MS/MS as a confirmatory method for PCDD/Fs and dl-PCBs in food and feed samples. *Analytical and Bioanalytical Chemistry*, 2016, **408**(13), 3511–3525. https://doi.org/10.1007/s00216-016-9428-9
60. Kitamura, K., Takazawa, Y., Takei, Y., Zhou, X., Hashimoto, S., Choi, J.-W. et al. Development of a method for dioxin analysis of small serum samples with reduced risk of volatilization. A*nalytical Chemistry*, 2005, **77**(6), 1727–1733. https://doi.org/10.1021/AC0486387
61. EU. Directive 2010/75/EU of the European Parliament and of the Council of 24 November 2010 on industrial emissions (integrated pollution prevention and control). *Official Journal of the European Union*, 2010, L 334, 17–119.
62. EU. Commission Implementing Decision (EU) 2021/2326 of 30 November 2021 establishing best available techniques (BAT) conclusions, under Directive 2010/75/EU of the European Parliament and of the Council, for large combustion plants. *Official Journal of the European Union*, 2021, L 469, 1–81.
63. Li, X.-D., Zhang, J., Yan, J.-H., Chen, T., Lu, S.-Y., Cen, K.-F. Effect of water

on catalyzed de novo formation of polychlorinated dibenzo-*p*-dioxins and polychlorinated dibenzofurans. *Journal of Hazardous Materials*, 2006, **137**(1), 57–61. https://doi.org/10.1016/J.JHAZMAT.2006.01.068

64. Sun, J., Hu, J., Zhu, G., Zhang, D., Zhu, Y., Chen, Z. et al. PCDD/Fs distribution characteristics and health risk assessment in fly ash discharged from MSWIs in China. *Ecotoxicology and Environmental Safety*, 2017, 139, 83–88. https://doi.org/10.1016/j.ecoenv.2017.01.015
65. Wang, M. S., Chen, S. J., Lai, Y. C., Huang, K. L., Chang-Chien, G. P. Characterization of persistent organic pollutants in ash collected from different facilities of a municipal solid waste incinerator. *Aerosol and Air Quality Research*, 2010, **10**(4), 391–402. https://doi.org/10.4209/aaqr.2010.01.0001
66. Lopes, H., Proença, S. Insights into PCDD/Fs and PAHs in biomass boilers envisaging risks of ash use as fertilizers. *Applied Sciences*, 2020, **10**(14), 4951. https://doi.org/10.3390/APP10144951
67. Pham, M. T. N., Hoang, A. Q., Nghiem, X. T., Tu, B. M., Dao, T. N., Vu, D. N. Residue concentrations and profiles of PCDD/Fs in ash samples from multiple thermal industrial processes in Vietnam: formation, emission levels, and risk assessment. *Environmental Science and Pollution Research*, 2019, **26**(17), 17719–17730. https://doi.org/10.1007/s11356-019-05015-2
68. Zhang, G., Hai, J., Ren, M., Zhang, S., Cheng, J., Yang, Z. Emission, mass balance, and distribution characteristics of PCDD/Fs and heavy metals during cocombustion of sewage sludge and coal in power plants. *Environmental Science & Technology*, 2013, **47**(4), 2123–2130. https://doi.org/10.1021/es304127k
69. Ma, W., Hoffmann, G., Schirmer, M., Chen, G., Rotter, V. S. Chlorine characterization and thermal behavior in MSW and RDF. *Journal of Hazardous Materials*, 2010, **178**(1–3), 489–498. https://doi.org/10.1016/J.JHAZMAT.2010.01.108
70. Yudovich, Y. E., Ketris, M. P. Chlorine in coal: a review. *International Journal of Coal Geology*, 2006, **67**(1–2), 127–144. https://doi.org/10.1016/J.COAL.2005.09.004
71. Spears, D. A. A review of chlorine and bromine in some United Kingdom coals. *International Journal of Coal Geology*, 2005, **64**(3–4), 257–265. https://doi.org/10.1016/J.COAL.2005.04.002
72. Pan, Y., Yang, L., Zhou, J., Liu, J., Qian, G., Ohtsuka, N. et al. Characteristics of dioxins content in fly ash from municipal solid waste incinerators in China. *Chemosphere*, 2013, **92**(7), 765–771. https://doi.org/10.1016/j.chemosphere.2013.04.003
73. Zhai, J., Burke, I. T., Stewart, D. I. Potential reuse options for biomass combustion ash as affected by the persistent organic pollutants (POPs) content. *Journal of Hazardous Materials Advances*, 2022, **5**, 100038. https://doi.org/10.1016/j.hazadv.2021.100038

Appendix 1. Dioxin congeners and total concentrations in the ashes from shale oil production plants and Auvere Power Plant, ng/kg

	Enefit280 CY	**Enefit280 ESP**	**Enefit140 total**	**Enefit140 ESP**	**Petroter CY**	**Petroter ESP**	**Auvere BA**	**Auvere ESP**	**Auvere FF**
PCB 105	<200	<300	<220	<790	<480	<360	<87	<66	<120
PCB 114	<14	<14	<11	<46	<24	<12	<4.8	<5.5	<6
PCB 118	<260	<340	<300	<1000	<550	<380	<100	<84	<150
PCB 123	<4.7	<12	<3.9	<27	<17	<15	<5	<5.5	<6
PCB 126	<7.8	<6.9	<7.7	<3.9	<5.6	<7.2	<8.4	<8.5	<8.2
PCB 156	<31	<67	<49	<140	<160	<63	<19	<18	<34
PCB 157	<8.3	<15	<9	<23	<14	<6.5	<12	<17	<14
PCB 167	<5.9	<19	<15	<40	<47	<21	<6.9	<8.2	<8.5
PCB 169	<7.7	<6.4	<7	<4.2	<7.2	<7.8	<11	<10	<9.8
PCB 189	<7.5	<25	<9.5	<43	<43	<16	<91	<12	<35
PCB 77	<140	<190	<150	<470	<220	<170	<52	<30	<69
PCB 81	<v5	<9.4	<8	<16	<17	<16	<4	<4.3	<4.4
∑ UB PCB	691.9	1004.7	790.1	2603.1	1584.8	1074.5	401.1	269	464.9
∑ TEQ PCB	**1.04**	**0.93**	**1.02**	**0.63**	**0.84**	**1.0**	**1.18**	**1.16**	**1.13**
1,2,3,4,6,7,8-HpCDD	<3.8	<4.2	<3.3	<83	<29	<6.1	<6.4	<5.9	<5.9
1,2,3,4,6,7,8-HpCDF	<2.4	<6.6	<4.9	<10	<28	<4.6	<5.6	<4.6	<10
1,2,3,4,7,8-HxCDD	<2.1	<2.1	<2.1	<1.9	<1.9	<2.8	<3	<2.6	<2
1,2,3,4,7,8-HxCDF	<1.9	<1.5	<1.3	<1.3	<1.1	<1.4	<1.4	<1.7	<2

Appendix 1. (continued)

	Enefit280 CY	**Enefit280 ESP**	**Enefit140 total**	**Enefit140 ESP**	**Petroter CY**	**Petroter ESP**	**Auvere BA**	**Auvere ESP**	**Auvere FF**
1,2,3,4,7,8,9-HpCDF	<5.2	<5.1	<3.3	<3.3	<31	<4.8	<5.7	<7	<3.1
1,2,3,6,7,8-HxCDD	<2.1	<2.1	<2.1	<4.1	<1.7	<2.5	<2.9	<2.8	<2.1
1,2,3,6,7,8-HxCDF	<1.8	<1.8	<1.6	<0.6	<0.98	<1.6	<1.4	<1.7	<2.1
1,2,3,7,8-PeCDD	<1.6	<1.5	<1.2	<1.6	<0.8	<1.2	<1.7	<1.3	<1.8
1,2,3,7,8-PeCDF	<0.91	<0.91	<0.95	<0.62	<0.34	<1.2	<0.95	<0.84	<0.7
1,2,3,7,8,9-HxCDD	<2.3	<2.3	<2.3	<4.4	<1.9	<2.7	<3.2	<3.1	<2.3
1,2,3,7,8,9-HxCDF	<2.4	<2.2	<2	<0.7	<4.9	<1.7	<2	<2.5	<1.3
2,3,4,6,7,8-HxCDF	<2.1	<1.6	<1.9	<0.66	<1.7	<2.2	<1.7	<2.1	<1.1
2,3,4,7,8-PeCDF	<0.9	<0.96	<0.97	<0.4	<0.65	<1.6	<1.1	<0.97	<0.91
2,3,7,8-TCDD	<1	<1	<1.4	<0.45	<0.7	<0.79	<0.7	<0.92	<1
2,3,7,8-TCDF	<0.82	<1.5	<0.96	<0.5	<0.49	<0.73	<0.56	<0.68	<0.89
OCDD	<11	<19	<9.6	<180	<110	<20	<18	<11	<43
OCDF	<3.6	<6.1	<3.1	<14	<34	<6.4	<12	<7.1	<14
∑ UB PCDD	23.9	32.2	22	275.45	146	36.09	35.9	27.62	58.1
∑ UB PCDF	22.03	28.27	20.98	32.08	103.16	26.23	32.41	29.19	36.1
∑ TEQ PCDD	**3.29**	**3.20**	**3.28**	**3.97**	**2.37**	**2.86**	**3.38**	**3.13**	**3.51**
∑ TEQ PCDF	**1.28**	**1.29**	**1.18**	**0.65**	**1.72**	**1.37**	**1.18**	**1.30**	**1.17**
∑ TEQ dioxins	**7.97**	**5.42**	**5.48**	**5.26**	**4.93**	**5.23**	**5.75**	**5.60**	**5.81**

Abbreviations: CY – cyclone ash, ESP – electrostatic precipitator ash, BA – bottom ash, FF – fabric filter ash, UB – upper-bound approach, TEQ – toxic equivalent.

Appendix 2. Dioxin congeners and total concentrations in the ashes from Eesti Power Plant, ng/kg

	Eesti PC FF	**Eesti PC BA**	**Eesti PC FF**	**Eesti PC BA**	**Eesti PC FF**	**Eesti CFBC ESP**	**Eesti CFBC BA**	**Eesti CFBC ESP**	**Eesti CFBC BA**	**Eesti CFBC ESP**	**Eesti CFBC BA**
Wastewater, t/h	0	0	16	16	8	0	0	16	16	8	8
PCB 105	<290	<230	<160	<210	<140	<140	<120	<200	<98	<170	<150
PCB 114	<13	<11	<11	<9.4	<7.7	<4.9	<6	<13	<4.2	<11	<12
PCB 118	<300	<280	<180	<210	<160	<180	<160	<230	<130	<210	<180
PCB 123	<5.4	<4.9	<5.8	<5.8	<5.7	<5.9	<3.1	<5.8	<3.9	<6.5	<4.6
PCB 126	<7.2	<7.8	<7.9	<8.2	<8.3	<8.5	<8.2	<8	<9.1	<8.5	<7.9
PCB 156	<67	<39	<33	<59	<62	<35	<23	<58	<21	<44	<30
PCB 157	<7	<9.2	<4.9	<7.6	<17	<5.9	<1.6	<8	<11	<8.7	<7.2
PCB 167	<20	<15	<12	<18	<17	<7.8	<7.4	<18	<4.7	<12	<12
PCB 169	<9.2	<6.1	<9	<6.3	<6.5	<4.7	<10	<6.3	<5.3	<5.7	<10
PCB 189	<43	<17	<9.9	<33	<32	<15	<8.1	<17	<11	<15	<18
PCB 77	<160	<140	<100	<120	<82	<75	<110	<140	<60	<100	<110
PCB 81	<15	<4.9	<24	<5.9	<7.1	<7.5	<13	<5.1	<4	<5.9	<4.2
∑ UB PCB	936.8	764.9	557.5	693.2	545.3	490.2	470.4	709.2	362.2	597.3	545.9
∑ TEQ PCB	**1.04**	**1.0**	**1.09**	**1.04**	**1.05**	**1.01**	**1.14**	**1.02**	**1.08**	**1.05**	**1.11**
1,2,3,4,6,7,8-HpCDD	<4.8	<3.6	<3.7	<5.3	<4.4	<4.7	<10	<4.2	<17	<20	<5.4
1,2,3,4,6,7,8-HpCDF	<6	<7.3	<5.8	<26	<5.4	<6.2	<13	<5.4	<27	<28	<4
1,2,3,4,7,8-HxCDD	<2.6	<1.4	<1.6	<0.75	<1.9	<1.9	<2.5	<2.4	<3.3	<1.3	<2.5
1,2,3,4,7,8-HxCDF	<1.7	<0.77	<1.7	<2.7	<1.4	<1.4	<1.6	<2	<1.3	<1	<1.8

Appendix 2. (continued)

	Eesti PC FF	Eesti PC BA	Eesti PC FF	Eesti PC BA	Eesti PC FF	Eesti CFBC ESP	Eesti CFBC BA	Eesti CFBC ESP	Eesti CFBC BA	Eesti CFBC ESP	Eesti CFBC BA
1,2,3,4,7,8,9-HpCDF	<4.5	<2.6	<2.8	<3.2	<4.1	<3.3	<4.2	<3.2	<2.1	<2.1	<6.1
1,2,3,6,7,8-HxCDD	<2.5	<1.2	<2	<0.8	<1.7	<1.8	<2	<2.6	<1.5	<1.6	<2.2
1,2,3,6,7,8-HxCDF	<1.8	<0.85	<2	<1.1	<1.3	<1.8	<1.5	<2.1	<1.1	<1.1	<1.7
1,2,3,7,8-PeCDD	<1.4	<1.8	<1.2	<2.1	<1.5	<1.3	<1.3	<1.9	<1.8	<1.4	<1.7
1,2,3,7,8-PeCDF	<0.96	<0.89	<1.3	<1.1	<0.97	<0.8	<1.1	<0.97	<0.86	<1	<1.2
1,2,3,7,8,9-HxCDD	<2.7	<1.3	<2.2	<0.87	<1.9	<2	<2.1	<2.8	<1.6	<1.7	<2.4
1,2,3,7,8,9-HxCDF	<2.3	<1	<2.4	<1.4	<2	<1.7	<2.1	<2.1	<2.2	<1.9	<2.5
2,3,4,6,7,8-HxCDF	<1.8	<1.2	<1.5	<1.2	<1.5	<1.8	<2.1	<2.1	<1.7	<1.4	<2.6
2,3,4,7,8-PeCDF	<1.3	<2.1	<1.5	<1.5	<1.2	<1	<1.2	<1.1	<0.97	<1.1	<1.1
2,3,7,8-TCDD	<0.8	<1	<1.1	<0.73	<0.8	<1.3	<0.91	<0.65	<0.73	<0.86	<0.71
2,3,7,8-TCDF	<0.81	<0.88	<0.89	<0.97	<0.68	<0.73	<0.73	<0.33	<0.68	<0.82	<0.65
OCDD	<19	<27	<28	<44	<11	<28	<14	<23	<35	<200	<24
OCDF	<6.3	<6	<6.2	<18	<7.2	<18	<9.4	<3.1	<11	<16	<15
∑ PCDD	33.8	37.3	39.8	54.55	23.2	41	32.81	37.55	60.93	226.86	38.91
∑ PCDF	27.47	23.59	26.09	57.17	25.75	36.73	36.93	22.4	48.91	54.42	36.65
∑ TEQ PCDD	**3.03**	**3.23**	**2.92**	**3.13**	**2.90**	**3.22**	**3.0**	**3.38**	**3.35**	**2.98**	**3.18**
∑ TEQ PCDF	**1.37**	**1.23**	**1.42**	**1.51**	**1.17**	**1.17**	**1.31**	**1.31**	**1.31**	**1.29**	**1.40**
∑ TEQ dioxins	**5.44**	**5.46**	**5.44**	**5.69**	**5.12**	**5.41**	**5.49**	**5.71**	**5.74**	**5.31**	**5.69**

Abbreviations: PC – pulverised combustion, FF – fabric filter ash, BA – bottom ash, CFBC – circulating fluidised bed combustion, ESP – electrostatic precipitator ash, UB – upper-bound approach, TEQ – toxic equivalent.

Oil Shale, 2026, 43, 1, 31–53 https://doi.org/10.3176/oil.2026.1.02

Reservoir characteristics and influencing factors of multi-lithofacies shales in the Lianggaoshan Formation, Northeast Sichuan Basin

Yuhang Zhou(a), Xin Tang(a)*, Mian Li(a,b)*, Qiuqi Chen(a), Zhangping Yan(a), Haoran Jiang(c), Ruiyu He(a), Linyan Li(a), Xiaoyi Zhou(a)

(a) School of Civil Engineering, Chongqing Three Gorges University, Chongqing 404100, China
(b) Chongqing Vocational Institute of Safety & Technology, Chongqing 404160, China
(c) Chongqing JUNENG Construction (Group) Co., Ltd., Chongqing 401120, China

Received 23 January 2025, accepted 23 January 2026, available online 29 January 2026

Abstract. *This study focuses on the shale of the Lianggaoshan Formation in the Northeast Sichuan Basin, aiming to analyze the pore structure characteristics and influencing factors of its lithofacies – critical for shale oil exploration, as the area has seen major shale oil and gas exploration breakthroughs. Fresh outcrop shale samples were collected in the field, followed by experiments including polarized-light microscope thin-section identification, X-ray diffraction, total organic carbon analysis, gas adsorption, high-pressure mercury intrusion, and scanning electron microscopy. Four lithofacies were classified. Results show the shale contains micropores, mesopores, and macropores; total organic carbon correlates positively with micropore/mesopore parameters but negatively with macropores, while quartz content shows the opposite. The Frenkel–Halsey–Hill fractal dimension correlates positively with total organic carbon, feldspar, and clay minerals, and negatively with quartz. This provides a key theoretical basis for local Lianggaoshan Formation shale oil exploration.*

Keywords: *Northeast Sichuan Lianggaoshan Formation, shale lithofacies, pore structure, TOC, mineral composition.*

1. Introduction

Since the North American shale oil and gas revolution, the global oil and gas resource pattern has undergone major changes. As a major contributor to today’s oil and gas resources, shale oil and gas has driven a continuous

---

* Corresponding author, mikechouzyh@foxmail.com

increase in global demand [1–3]. In recent years, China has steadily increased its shale oil exploitation intensity. China's recoverable shale oil volume grew from 4.37 × 10^9 tons in 2015 to 1.45 × 10^{10} tons in 2020, ranking third in the world [4–6]. Compared with North American marine shale reservoirs, most of China's shale reservoirs are formed in lacustrine environments and exhibit a series of unique geological characteristics. The single-layer thickness of China's lacustrine shale reservoirs is relatively thin. The sedimentary environment shows a high degree of complexity, with lithofacies changing rapidly over short distances. Reservoir heterogeneity is extremely prominent [7–9]. This complexity exerts an important restrictive influence on the enrichment of shale oil resources and the enhancement of exploration levels. It also gives rise to a diversity of lithofacies types and intensifies heterogeneity among lithofacies, thereby rendering it difficult to determine pore structure characteristics corresponding to different lithofacies [10, 11]. Consequently, undertaking systematic research on the basis of lithofacies units is of pivotal importance for shale oil exploration and evaluation. Notably, pore structure acts as the core "storage and migration channel" of shale oil – its type, size distribution, and connectivity directly determine the reservoir's oil-bearing capacity and fluid flow efficiency, which are essential prerequisites for accurately evaluating the recoverable potential of shale oil in the Lianggaoshan Formation (Fm).

The evolution of shale pore structure is influenced by a multitude of factors, including total organic carbon (TOC) content, mineral composition, structural deformation, water saturation, and lamina morphology. Zheng et al. [12] proposed that organic matter, along with components such as quartz and clay minerals, significantly impacts the pore structure of the Longmaxi Fm shale in the Sichuan Basin. Cheng et al. [13] indicated that structural deformation leads to the development of additional pores and fractures in shale. Specifically, intergranular pores, interlayer pores, and microfractures among mineral fragments represent the primary contributors to the expansion of the pore structure. Wang et al. [14] exemplified this in the Bossier shale of eastern Texas, USA, and analyzed the characteristics of lamina morphology and pore structure through thin-section petrography.

Previous investigations have predominantly focused on analyzing the pore structure characteristics of black lacustrine shales with high TOC content. However, the sedimentary environment of most lacustrine shale formations is intricate, and lithology changes rapidly. This complexity severely restricts our understanding of shale reservoir characteristics and their formation mechanisms. Hence, elucidating the influencing factors of pore structure across different lithofacies is crucial for exploring the shale reservoir potential of the Lianggaoshan Fm in the Northeast Sichuan Basin [15–17].

Since 2017, China National Petroleum Corporation and China Petroleum & Chemical Corporation have achieved significant new breakthroughs in the shale reservoirs of the Lianggaoshan Fm in the Northeast Sichuan Basis. These achievements indicate that the northeastern Sichuan region is likely to emerge as a crucial new lacustrine shale oil and gas production area in China [18, 19].

The shale strata of the Lianggaoshan Fm exhibit a broad maturity range (Ro: 0.9–1.9%), leading to distinct differences in micropore structures at various stages of maturity evolution [20–22]. To a large extent, the characteristics of the reservoir space in the study area remain unclear, which severely restricts exploration progress.

Consequently, this study focuses on shale samples from the Lianggaoshan Fm in the Northeast Sichuan Basin. Based on lamina characteristics identified through thin-section analysis and results from various geochemical experiments, the lithofacies are classified. By leveraging multiple pore-characterization techniques, such as gas adsorption, high-pressure mercury intrusion, and scanning electron microscopy (SEM), the pore structures of shale reservoirs with different lithofacies are systematically characterized. Moreover, the pore genesis of shale reservoirs in different lithofacies is analyzed, and the key controlling factors of the pore structures across lithofacies are disclosed.

2. Geological survey and experiments

2.1. Geological overview

The research area of this study is situated in the Qilixiang area of the Lianggaoshan Fm within the Northeast Sichuan Basin. This formation is characterized by a series of faults, uplifts, and depressions [23]. Based on geomorphological characteristics, the region can be further classified into the low-and-gentle structural belt in northern Sichuan, the low-and-steep structural belt in western Sichuan, the low-and-steep structural belt in southern Sichuan, and the high-and-steep structural belt in eastern Sichuan [24].

The Lianggaoshan Fm in the Northeast Sichuan Basin predominantly represents delta-lacustrine facies, with a thickness ranging from 1500 to 4000 meters. During the sedimentary period of the Lianggaoshan Fm, a large-scale lake transgression event took place. The internal terrain slope increased, and the surrounding structures rose rapidly [25]. Overall, the formation is mainly composed of semi-deep to deep lake deposits. Additionally, there are some delta deposits in the northwest and east, which supplied clastic materials to the lacustrine facies.

With the successful development of Well Ping’an 1 (yielding a daily output of 112.8 cubic meters), the shale oil of the Lianggaoshan Fm in the Northeast Sichuan Basin achieved a historic breakthrough in 2020. This milestone marks the Sichuan Basin as poised to become the core of China’s future shale oil exploration and development [26]. Actual exploration has demonstrated that shale oil production in the study area has reached a historic breakthrough, fully highlighting extensive shale oil resource prospects. This not only contributes to the evaluation of lacustrine shale oil exploration in China but also underscores the strategic significance of this region in the context of national shale oil development [23].

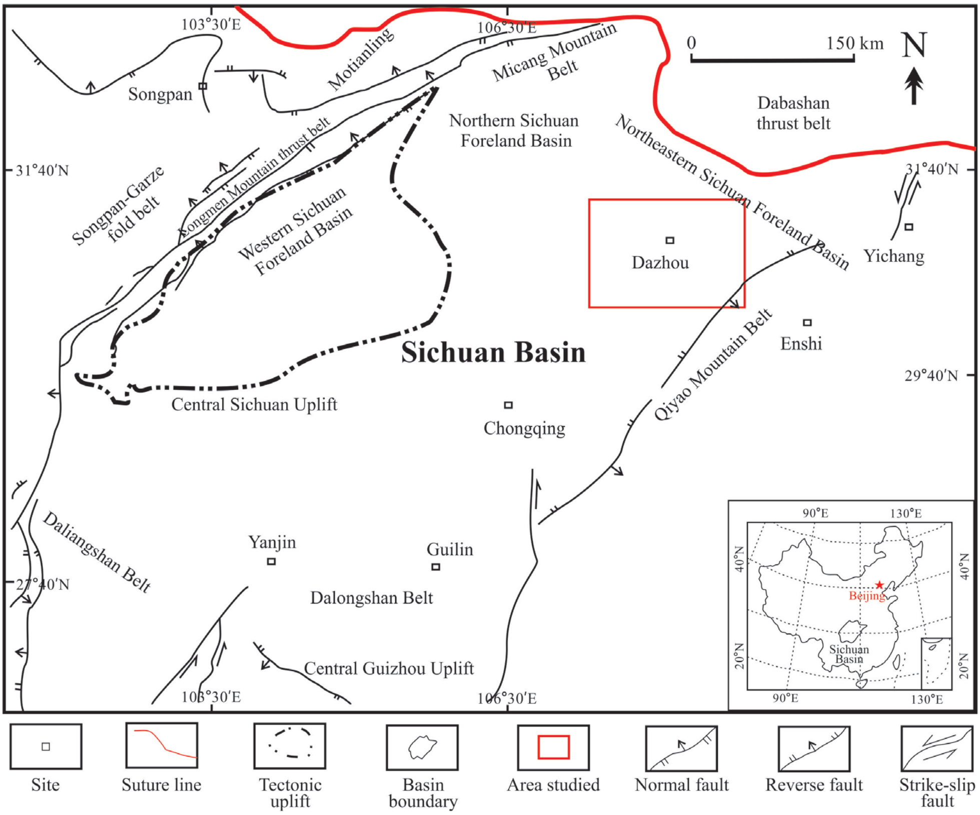

Fig. 1. Geological overview map of the Lianggaoshan Formation study area in the Northeast Sichuan Basin.

2.2. Research methods

A total of 20 fresh outcrop shale samples were collected from the Lianggaoshan Fm in the Northeast Sichuan Basin, and 15 valid samples were selected for subsequent experiments after preliminary screening (excluding samples with obvious weathering, fractures, or impurity contamination to ensure experimental reliability). Rock thin-sections were prepared from the collected samples for identification under a polarized-light microscope. The collected samples were manually ground into powder and sieved to a standard of 80–100 mesh. These powder samples were then utilized for geochemical experiments, including X-ray diffraction (XRD), TOC analysis, carbon dioxide (CO$_2$) adsorption, and nitrogen adsorption experiments. For the high-pressure mercury intrusion experiment and SEM analysis, block samples measuring 0.5c × 0.5 × 0.5 cm were fabricated.

For thin-section identification under polarized-light microscopy, a Leica DM4 P polarizing microscope was employed. Observation magnifications of 100× were used for overviews of bedding morphology, while 400× magnification was applied for characterizing mineral/pore details. Five fields of view were selected from each thin section for bedding type classification to ensure representativeness. XRD analysis was performed using a Rigaku Ultima IV diffractometer with a Cu Kα radiation source ($\lambda = 1.5406$ Å). The scan range was 5–80° (2θ) with a step size of 0.02° and a scan speed of 5°/min. Mineral content was calculated using the Rietveld refinement method via MDI Jade 6.5 software.

TOC analysis employed a RIKEN CS744 analyzer. Samples underwent 10% hydrochloric acid pretreatment to remove inorganic carbon, followed by analysis at 950 °C in an oxygen flow of 200 mL/min. TOC content was determined by quantifying CO_2 produced from organic carbon combustion. Gas adsorption experiments (CO_2/N_2) employed a JW-BK 132F analyzer. Samples were vacuum-dried at 105 °C for one hour to remove adsorbed water. CO_2 adsorption was conducted at 0 °C (30-second equilibration at each pressure point), while N_2 adsorption occurred at –196 °C (60-second equilibration at each pressure point). Pore parameters were calculated using the Dubinin–Radushkevich (DR) model and Barrett–Joyner–Halenda (BJH) model, respectively.

High-pressure mercury porosimetry was performed using a McMurry AutoPore IV porosimeter (pressure range: 0.001–414 MPa, mercury contact angle: 140°, density: 13.546 g/cm^3). Mercury intrusion/evacuation curves

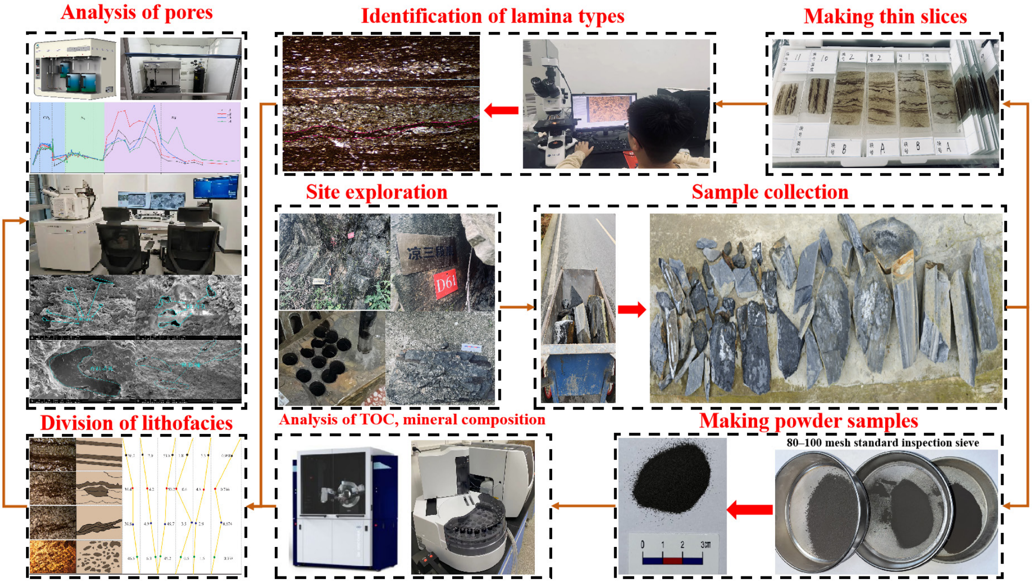

Fig. 2. Experimental workflow for shale samples from the Lianggaoshan Formation.

were automatically recorded to calculate macropore volume. SEM analysis employed a Zeiss Gemini SEM 360 operating in secondary electron mode at 10–20 kV, with a working distance of 8–12 mm and magnification ranging from 500× to 50 000×. Specimens were sputter-coated with a 5 nm gold layer prior to observation to enhance conductivity.

Statistical analysis of experimental data was conducted using Origin 2024 software. Pearson correlation coefficient analysis was applied to evaluate the relationships between TOC/mineral composition and pore-structure parameters (e.g., pore volume, specific surface area), with the coefficient of determination (R^2) indicating fitting quality. For fractal dimension calculation (FHH model), linear fitting of low-temperature nitrogen adsorption data was performed. Each experiment was repeated three times, and the arithmetic mean with standard deviation was reported (relative standard deviation, RSD $< 5\%$) to ensure data reliability.

3. Experimental results

3.1. Classification of shale lithofacies

Through thin-section analysis, and based on the morphology of laminated sedimentary structures, the shale laminations in the study area were classified into three microscopic morphologies: straight, corrugated, and graded types. Straight laminations display continuous development in the form of straight stripes. Corrugated laminations generally present continuous wavy development. Graded laminations bear resemblance to straight laminations; however, the thickness variation between the bright and dark layers is significant, and the change in grain size is prominent. XRD analysis reveals that straight laminations possess the highest clay-mineral content, with corrugated laminations having a slightly lower content, and graded laminations having the lowest. In contrast, the content of quartz and feldspar is highest in graded laminations, followed by corrugated and then straight laminations. In terms of TOC content, straight laminations exhibit the highest values, corrugated laminations have lower values, and graded laminations have the least.

This study integrates the research methodologies proposed by previous scholars [27, 28]. In light of the multi-type lamina characteristics of shale within the Lianggaoshan Fm in the Northeast Sichuan Basin, a lithofacies classification scheme founded on “mineral composition–TOC-lamina morphology” was formulated [29–31]. Among these factors, TOC content serves as a crucial parameter for differentiating lithofacies and can be categorized into four grades: high-carbon (TOC content > 1.5%), medium-carbon (TOC 1.0–1.5%), low-carbon (TOC 0.5–1.0%), and carbon-poor (TOC < 0.5%). Minerals are designated as single-lithology when a single component exceeds 50%, and as mixed-lithology when no dominant component exists (with each component ranging from 25% to 50%).

Table 1. Characteristics of shale lithofacies in the Qilixiang area of the Lianggaoshan Formation, Northeast Sichuan Basin

Lithofacies types	Laminated forms	Average mineral composition, %					Average TOC, %
		Quartz	Feldspar	Clay	Carbonate	Others	
L1 - low-carbon straight-laminated clay shale	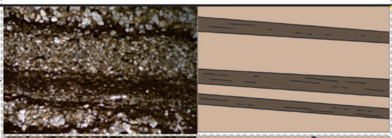	36.2	2.9	53.8	1.8	5.3	0.968
L2 - low-carbon wavy-laminated clay shale	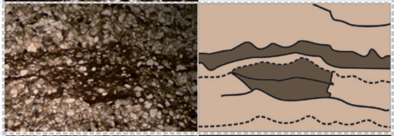	39.4	4.2	50.2	0.6	4.8	0.746
L3 - low-carbon wavy-laminated mixed shale	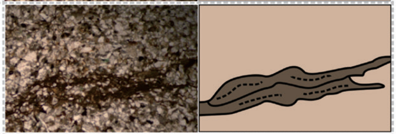	39.8	4.9	49.7	3.5	2.9	0.874
L4 - carbon-poor graded-laminated mixed shale	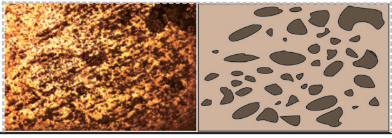	46.5	6.3	45.2	0.5	1.5	0.338

3.2. Pore type characteristics from scanning electron microscopy

For the shale fabrics of different lithofacies types, the differences in pore types and development characteristics were analyzed via SEM observations. The classification of pore types adhered to the previous research scheme [31]. The pores observed under SEM were categorized into intergranular pores, intragranular pores, organic-matter pores, and microfractures [32].

In the study area, samples of lithofacies types L1, L2, and L3 commonly exhibit the distribution of organic matter and clay minerals, with well-developed microstructures. Minerals such as feldspar and flaky mica are distributed along bedding planes, within which intragranular pores have developed. Intergranular and intragranular pores are the most prominently developed pore types. Some intragranular pores have transformed into clay minerals, while others are filled with honeycomb-like illite/smectite mixed layers. The intergranular pores are filled with scaly kaolinite. The sample surfaces are relatively dense. In L4-type samples, organic matter is mainly present in interstitial form, while pyrite is dispersed and locally aggregated (Fig. 3).

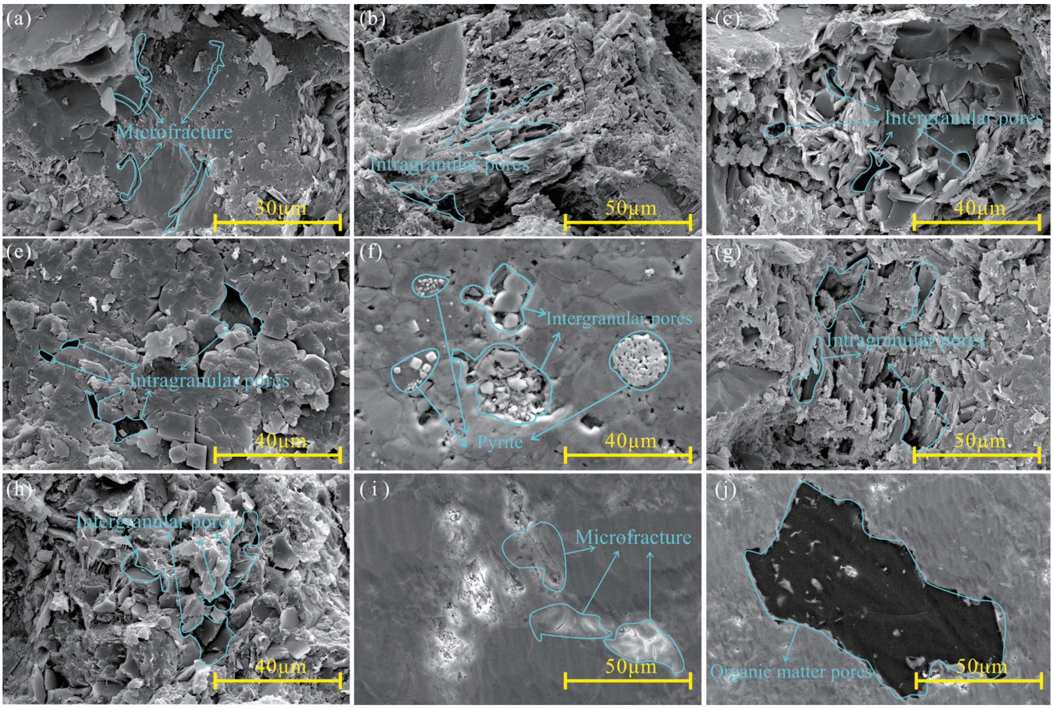

Fig. 3. Shale pore types of the Lianggaoshan Formation, Northeast Sichuan Basin: (a) organic matter associated with clay minerals, with developed micropores; (b) feldspar dissolved along cleavage forming intragranular pores; (c) scale-like kaolinite and a small amount of illite filling intergranular pores, with dense cementation; (d) granular calcite associated with a small amount of illite, with developed intergranular pores; (e) clay minerals developing intergranular pores, partially filled by organic matter, with strawberry-shaped pyrite visible; (f) feldspar dissolved to form intergranular pores, partially transformed into clay minerals; (g) scale-like kaolinite filling intragranular pores, with a small number of intergranular pores developed; (h) clastic minerals dissolved to form intergranular pores, partially transformed into clay minerals, with intercrystalline pores in clay minerals visible; (i) massive organic matter enclosing fine clastic mineral particles, with clay minerals developing a small number of micropores; (j) blocky organic matter developing pores.

3.3. Gas adsorption and high-pressure mercury intrusion experiments

CO_2 adsorption, nitrogen adsorption, and high-pressure mercury intrusion experiments can effectively characterize the pore structure of shale across the entire pore-size range [33]. Based on the IUPAC standards and previous research, pores with diameters of 0–2 nm are classified as micropores, those with diameters of 2–10 nm are classified as mesopores, and pores with diameters greater than 10 nm are classified as macropores [34, 35].

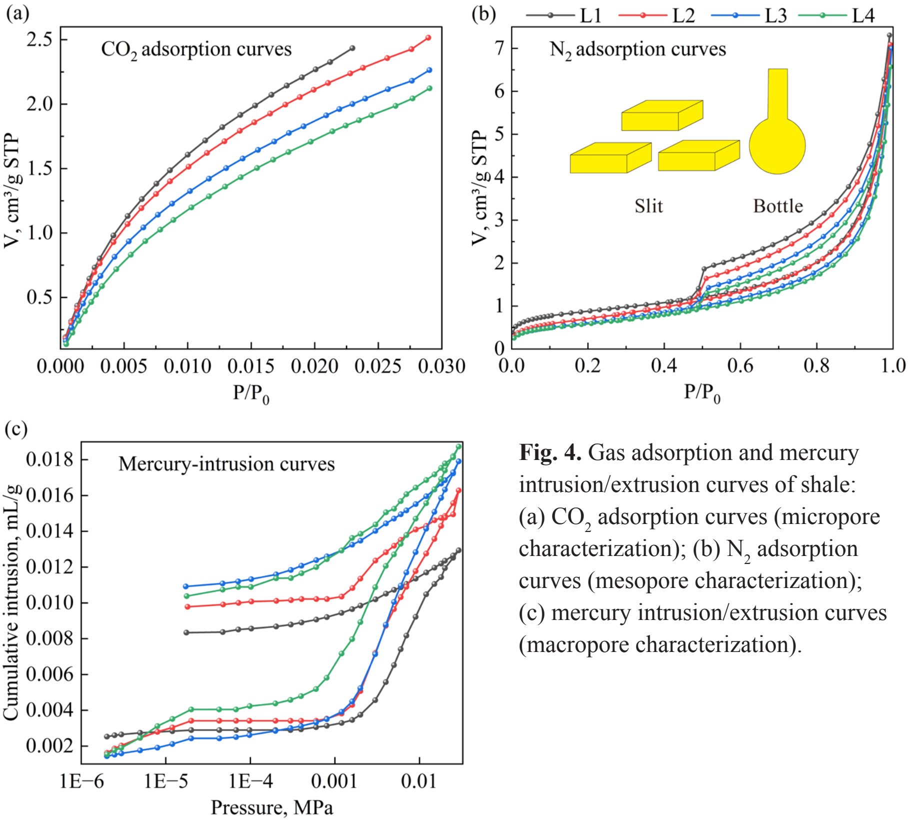

Fig. 4. Gas adsorption and mercury intrusion/extrusion curves of shale: (a) CO_2 adsorption curves (micropore characterization); (b) N_2 adsorption curves (mesopore characterization); (c) mercury intrusion/extrusion curves (macropore characterization).

The shapes of the CO_2 adsorption curves of shale samples remain essentially unchanged, indicating that the micropore morphologies of shale samples of different lithofacies are similar (Fig. 4a). According to the IUPAC classification [34], the nitrogen adsorption curves correspond to type IV, and the hysteresis loops exhibit characteristics of both types H2 and H3, reflecting the presence of slit-shaped and bottle-shaped mesopores (Fig. 4b). For all samples, during the mercury-injection stage of the mercury-intrusion curves, the mercury-injection volume first increases slowly and then rapidly with increasing pressure. During the mercury-withdrawal stage, the decrease in the mercury-withdrawal volume is relatively gentle (Fig. 4c).

The CO_2 adsorption, nitrogen adsorption, and high-pressure mercury intrusion experiments were respectively combined to characterize the pore-size distributions of micropores, mesopores, and macropores in shale samples of different lithofacies. Shale of various lithofacies in the Lianggaoshan Fm shows a certain degree of development of various pore types, mainly concentrated in micropores and macropores. The micropores of shale samples in the Lianggaoshan Fm are primarily in the pore-size range of 0.73–1.22 nm, the mesopores in the range of 2.08–6.27 nm, and the macropores in the range of 11–100 nm (Fig. 5).

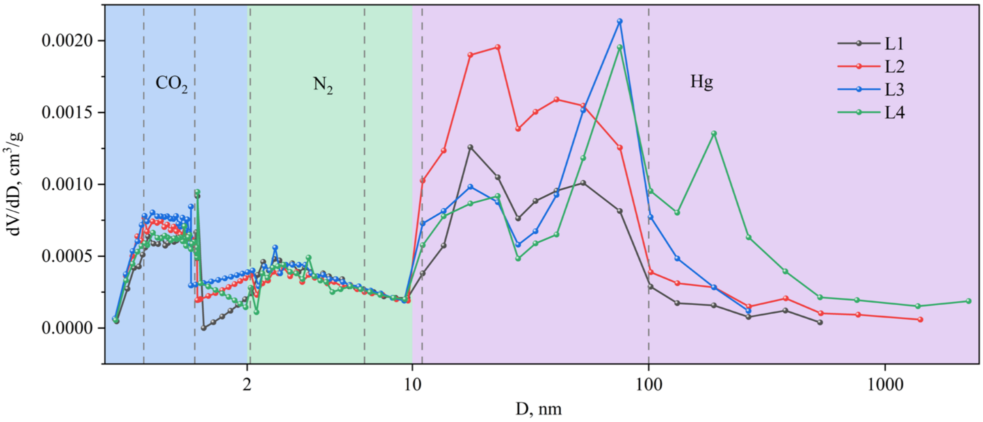

Fig. 5. Pore-size distribution of shale reservoir space in the Lianggaoshan Formation, Northeast Sichuan Basin. Abbreviations: D = pore diameter (nm), dV = differential pore volume (cm^3/g), dD = differential pore diameter interval (nm).

4. Discussion

4.1. Difference mechanism of pore structure in different lithofacies shales

In this study, the pore volume was calculated employing the Barrett–Joyner–Halenda (BJH) model, while the specific surface area was determined by the Brunauer–Emmett–Teller (BET) model. For the shale within the Lianggaoshan Fm, the micropore volume ranges from 0.0044 to 0.0051 cm^3/g, the mesopore volume varies between 0.00227 and 0.00259 cm^3/g, and the macropore volume spans from 0.00818 to 0.00876 cm^3/g. The micropore specific surface area lies between 2.13902 and 2.29159 m^2/g, the mesopore specific surface area ranges from 2.71345 to 2.943879 m^2/g, and the macropore specific surface area is within 1.96937–2.72285 m^2/g. These results indicate that macropores make the most substantial contribution to the overall pore structure (Fig. 6).

This phenomenon can be ascribed to the combined effects of relatively low TOC in this region and the presence of an adequate quantity of brittle minerals (quartz and feldspar, with a combined content exceeding 40%) and clay minerals (content > 50%) [36]. The relatively low TOC content makes it difficult for shale to generate irregular micropores, resulting in a pore structure of low complexity. A certain proportion of brittle minerals helps preserve the integrity of the pore structure and facilitates the formation of intergranular and intercrystalline pores, as well as microfractures within inorganic minerals. This, in turn, is conducive to enhancing the pore connectivity of shale [37].

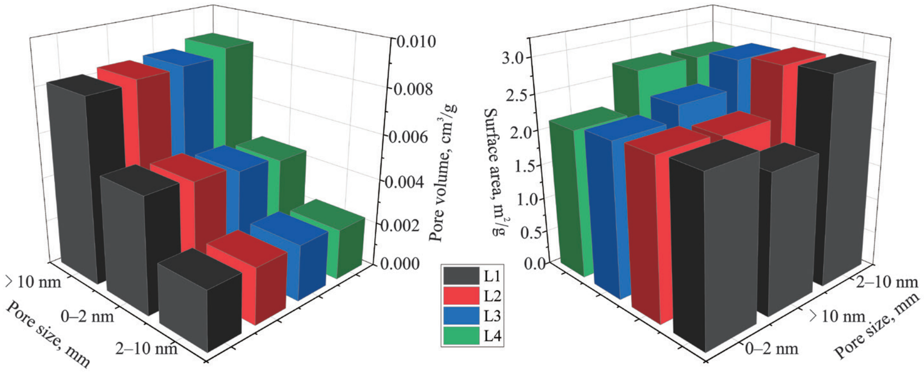

Fig. 6. Distribution map of shale pore volume and specific surface area of the Lianggaoshan Formation, Northeast Sichuan Basin.

In lacustrine shale, the rough surfaces of clay minerals promote the development of additional micropores, exerting a relatively pronounced influence on the micropore structure. Simultaneously, they contribute to maintaining reservoir stability and the optimal functionality of shale [38]. Additionally, carbonate minerals can impact the pore structure of shale [39], presumably because carbonate cements fill pores during the diagenetic process [40].

Based on the experimental results, this study summarizes the mechanisms through which the pore structure is influenced under different lithofacies.

For L1 – low-carbon flat-laminated clay shale, it exhibits the highest TOC and clay-mineral contents, along with the lowest brittle-mineral content, suggesting a relatively high organic-matter content [41]. Micropores and mesopores have a more favorable development potential compared to macropores [42]. Moreover, this lithofacies is more prone to the formation of numerous pores and microfractures, which significantly impact pore volume and specific surface area [43]. This phenomenon exerts a notable influence on the adsorption capacity of oil and gas resources within micropores [44]. Specifically, the quantity of micropores reflects, to a certain degree, the hydrocarbon-generation capacity of shale reservoirs [45].

In contrast, for L4 – carbon-poor graded-laminated mixed shale, its lower clay-mineral content makes it challenging to form micropores and mesopores [46]. As a consequence, the corresponding specific surface area and pore volume are reduced. However, the increase in the volume and specific surface area of macropores improves, to a certain extent, the transport and diffusion of oil and gas resources within shale reservoirs [47].

The distinct pore-structure differences among the four lithofacies (L1–L4) essentially reflect variations in their sedimentary environments and diagenetic processes [48]. For L1 (low-carbon straight-laminated clay shale) and L2 (low-carbon wavy-laminated clay shale), their high clay-mineral and TOC contents are attributed to deposition in a semi-deep to deep lake environment (Section 2.1). This environment featured stable water columns, weak hydrodynamic conditions, and strong reducing conditions – favorable for the preservation of organic matter and the accumulation of fine-grained clay minerals [25, 28]. During early diagenesis, compaction of clay minerals promoted the formation of intercrystalline micropores, while thermal maturation of organic matter (R_o: 0.9–1.9%; Section 1) generated additional organic matter pores, collectively enhancing micropore and mesopore development [20, 35]. In contrast, L4 (carbon-poor graded-laminated mixed shale) was deposited in a delta-front transitional environment, where intermittent hydrodynamic disturbances led to the sorting and accumulation of quartz and feldspar (brittle minerals) [25]. During diagenesis, the low compressibility of brittle minerals prevented the collapse of intergranular spaces, forming macropores dominated by intergranular and dissolution pores (Fig. 3h). Meanwhile, the lack of organic matter (TOC $<0.5\%$; Table 1) limited the formation of organic micropores, resulting in a macropore-dominated pore structure [32, 40].

4.2. Relationship between shale TOC content, mineral composition, and pore-structure parameters

Based on the preceding mechanism analysis, this section conducts a correlation analysis between TOC content, clay minerals, quartz, and pore-structure parameters. It quantitatively evaluates the relationships between shale lithofacies characteristics and pore-structure parameters, and explores the differential characteristics of pore structures at different scales in shales of various lithofacies.

TOC is positively correlated with the pore volume and specific surface area of micropores and mesopores, and negatively correlated with those of macropores. The pore volume of macropores and the specific surface area of micropores and mesopores are more significantly affected by TOC content. The correlation between the pore volume of micropores and TOC content is slightly stronger than that of mesopores (Fig. 7a, c). This is because organic matter is a significant contributor to micropore development, and TOC content is closely related to the presence of organic matter [49]. During shale reservoir formation, organic matter forms micropores during kerogen pyrolysis and hydrocarbon generation [23]. These processes generate a large number of tiny pores, increasing both pore volume and specific surface area of micropores. Meanwhile, hydrocarbons generated during the maturation of organic matter may cause some micropores to expand into mesopores, and direct mesopore formation within organic matter may also occur, further increasing the pore volume and specific surface area of mesopores [50].

Quartz content is negatively correlated with the pore volume and specific surface area of micropores and mesopores, and positively correlated with those

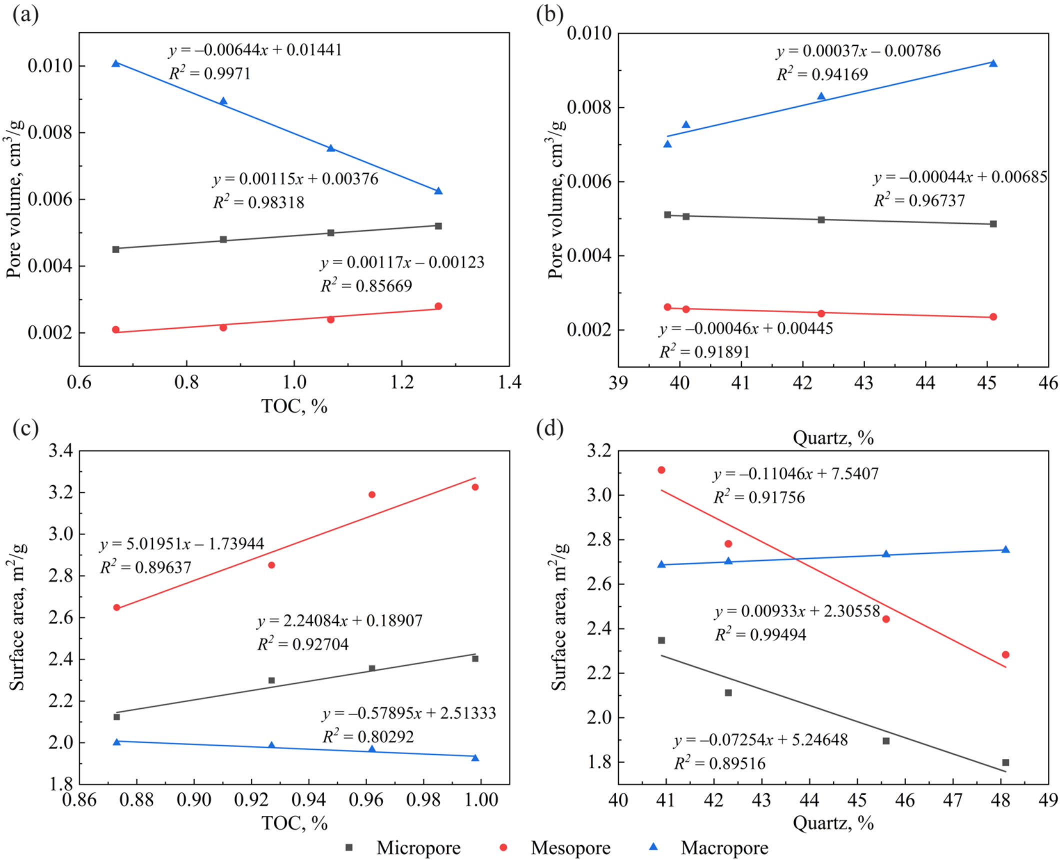

Fig. 7. Correlation analysis between TOC, quartz content, and pore-structure parameters. Left column (a, c): Correlations between TOC content and pore parameters – TOC vs. pore volume (a) and TOC vs. specific surface area (b). Right column (b, d): Correlations between quartz content and pore parameters – quartz content vs. pore volume (b) and quartz content vs. specific surface area (d).

of macropores (Fig. 7b, d). Quartz is relatively compact, and when its content increases, it occupies space, potentially leading to a reduction in the pore volume of micropores and mesopores in shale. Macropores, however, are mainly composed of large intergranular pores, fractures, and some dissolution pores. Therefore, their pore volume is more easily affected by quartz content [24]. The specific surface area of shale pores is mainly contributed by micropores and mesopores. An increase in quartz content dilutes, to a certain extent, the contributions of other minerals with large specific surface areas – such as clay minerals and organic matter – thus reducing the overall specific surface area of the shale [51].

Quartz, being an inert mineral with low chemical activity, rarely undergoes dissolution during diagenesis. Thus, its increase occupies the space originally available for clay minerals and organic matter, reducing micropore and mesopore volume [36]. In contrast, feldspar – a reactive mineral found in L3 and L4 lithofacies – is prone to dissolution under acidic diagenetic fluids generated during organic matter maturation, forming intragranular dissolution pores (Fig. 3b, f) [52]. This explains why L3 (feldspar content: 4.9%; Table 1) has a slightly higher mesopore volume than L2 (feldspar content: 4.2%) – feldspar dissolution partially compensates for the reduction in micropores caused by quartz [40].

4.3. Relationship between TOC content, mineral composition, and fractal dimension of shale

The fractal dimension is an effective method for quantitatively characterizing the microscopic pore structure of shale reservoirs. It can be used to evaluate the complexity and heterogeneity of shale pores. In this paper, the fractal theory is applied to quantitatively characterize the pore-structure features of the Lianggaoshan Fm shale. Based on experimental low-temperature nitrogen adsorption data, the Frenkel–Halsey–Hill (FHH) fractal model was established, and the fractal dimension parameters were calculated using the established model [53, 54]. The formula for the FHH fractal dimension is as follows:

$$\ln V = k \ln\left(\ln\left(\frac{P_0}{P}\right)\right) + C \tag{1}$$

where V represents the gas adsorption volume at adsorption equilibrium pressure (cm^3/g), k is the linear correlation coefficient (a constant related to the adsorption mechanism), and C is a constant (the intercept of the linear fitting curve for the FHH model). In this study, the entire relative-pressure curve was analyzed using the low-temperature nitrogen adsorption data, with capillary condensation as the adsorption mechanism. The fractal dimension D is calculated as follows:

$$D = k + 3 \tag{2}$$

In this research, a quantitative analysis was conducted to examine the relationships among TOC content, mineral components, and fractal dimension. The objective was to explore differences in pore structures across diverse shale lithofacies and to assess the impacts exerted by TOC content and mineral components shale pore characteristics.

The calculated fractal dimension (D) of the Lianggaoshan Fm shale spans from 2.51123 to 2.53098, while the coefficient of determination (R^2) ranges between 0.97061 and 0.98639. These values indicate a relatively high degree of fitting (Fig. 8).

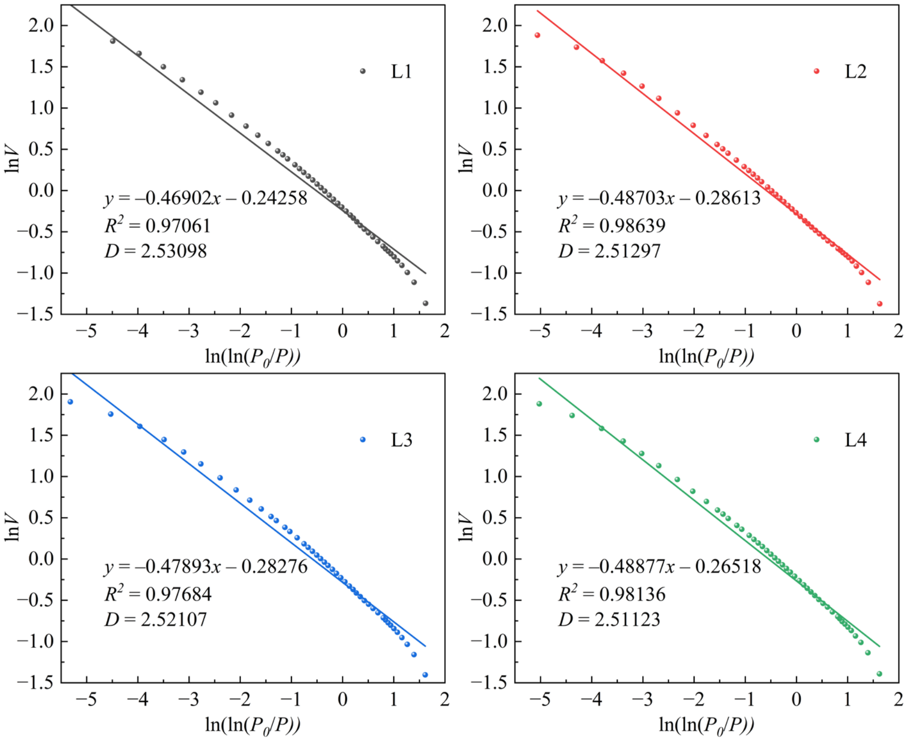

Fig. 8. Fractal fitting curves of shale samples with different lithofacies in the Lianggaoshan Formation, Northeast Sichuan Basin.

A positive correlation exists between the fractal dimension and TOC content. Specifically, as TOC content increases, the fractal dimension becomes larger, signifying a more intricate pore structure (Fig. 9). Because micropores are predominantly developed within organic matter, a lower TOC content corresponds to a smaller fractal dimension, leading to a simpler pore structure [55].

Conversely, a negative correlation is observed between the fractal dimension and quartz content. Owing to the stable crystal structure of quartz, it presents a relatively regular and less complex pore structure. Hence, an increase in quartz content results in a decrease in the fractal dimension [12].

The fractal dimension is positively correlated with feldspar content. This is attributed to the fact that feldspar dissolution generates secondary pores, augmenting the overall complexity of the shale pore structure [52].

Moreover, the fractal dimension also demonstrates a positive correlation with clay-mineral content. This can be explained by the large specific surface area of clay minerals, within which micropores and mesopores are predominantly distributed, thereby contributing to a high level of pore complexity [55].

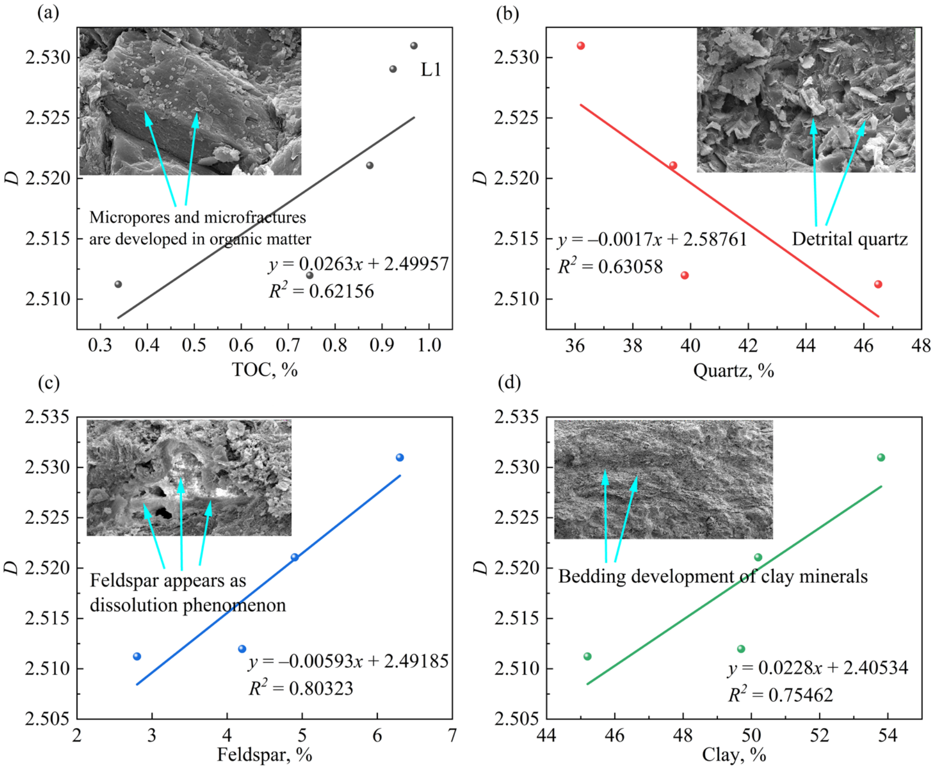

Fig. 9. Correlation analysis between the fractal dimension of Lianggaoshan Formation shale and TOC, quartz, feldspar, and clay-mineral contents.

4.4. Relationship between pore characteristics and shale reservoir potential

The pore-structure parameters (volume, specific surface area, and connectivity) of the Lianggaoshan Fm shale directly determine their shale oil reservoir potential, as verified by experimental data. Micropores and mesopores serve as the primary carriers for adsorbed shale oil, whereas macropores facilitate the storage of free oil [32, 52]. The L1 facies exhibits the largest micropore volume (0.0051 cm^3/g) and the highest mesopore specific surface area (2.94 m^2/g), endowing it with strong adsorption capacity. This is further supported by its TOC content (0.968%), as organic pores can absorb two to three times more oil than inorganic pores [12, 50].

Macropores (diameter > 10 nm) and microfractures serve as key flow pathways for shale oil [37]. Facies L4 exhibits the largest macropore volume (0.00876 cm^3/g) and the highest brittle-mineral content (quartz + feldspar = 52.8%; Table 1), indicating superior pore connectivity.

Within the study area, facies L1–L3 – characterized by well-developed micropores and mesopores with strong oil-trapping capacity – are suitable as oil-rich reservoirs, whereas facies L4, dominated by macroporosity with good fluid mobility, can serve as oil migration pathways. This reservoir–channel coupling provides a geological basis for selecting favorable exploration sections in the Lianggaoshan Fm of Northeast Sichuan [19, 23].

This study advances lacustrine shale reservoir research in three key aspects. First, unlike previous studies focused on high-TOC marine shales (e.g., Longmaxi Formation, Barnett Shale), this work systematically characterizes the pore structure of low-TOC lacustrine shales (TOC: 0.338–0.968%) in the Lianggaoshan Fm. The findings demonstrate that even low-TOC lacustrine shales can form effective reservoirs via clay interstitial pores and brittle-mineral macropores, thereby supplementing understanding of lacustrine shale reservoir genesis mechanisms [10, 24]. Second, by establishing an lithological facies–pore structure–reservoir potential correlation model (Figs 6, 7, 9), this study provides a quantitative method for evaluating low-TOC lacustrine shale reservoirs, improving upon the qualitative facies classifications of earlier studies [29, 31]. Third, the findings clarify the influence of sedimentary environments (semi-deep lake and deltaic foreland) on pore development in the Lianggaoshan Fm, providing a reference for predicting pore structures in analogous global lacustrine shale sequences (e.g., Denver Basin, Wakamulta Fm).

5. Conclusions

Through a series of physical experiments and in-depth data analyses, this study meticulously investigated the microscopic structural characteristics of shale in the Lianggaoshan Formation. Lithofacies classification was accomplished by comprehensively integrating the outcomes of thin-section analysis, X-ray diffraction experiments, and TOC content measurements. Pore and fracture features were examined microscopically using scanning electron microscopy. Quantitative characterization of shale microstructures was conducted through carbon dioxide adsorption, nitrogen adsorption, and high-pressure mercury intrusion experiments. Based on nitrogen adsorption data, the fractal dimension was calculated to explore the pore-structure features of the Lianggaoshan Formation shale. Drawing on experimental results and subsequent analyses, the following conclusions were reached:

1. The laminated shale of the Lianggaoshan Formation can be taxonomically divided into four distinct lithofacies: L1 – low-carbon straight-laminated clay shale, L2 – low-carbon wavy-laminated clay shale, L3 – low-carbon wavy-laminated mixed shale, and L4 – carbon-poor graded-laminated mixed shale. L1 shale exhibits the highest average TOC and clay-mineral contents, whereas L4 shale contains the greatest quartz and feldspar content. Organic matter and clay minerals are widely distributed in L1–L3 samples, where microfractures are well developed.

2. In the Lianggaoshan Formation shale, the micropore volume ranges from 0.0044 to 0.0051 cm^3/g, the mesopore volume from 0.00227 to 0.00259 cm^3/g, and the macropore volume from 0.00818 to 0.00876 cm^3/g. The specific surface area of micropores extends from 2.13902 to 2.29159 m^2/g, that of mesopores varies from 2.71345 to 2.943879 m^2/g, and that of macropores ranges from 1.96937 to 2.72285 m^2/g. TOC content and mineral composition exert a profound influence on shale pore structure. TOC is positively correlated with the pore volume and specific surface area of micropores and mesopores but negatively correlated with those of macropores. Quartz content exhibits a negative correlation with the pore volume and specific surface area of micropores and mesopores, while demonstrating a positive correlation with those of macropores.
3. The fractal dimension (D) of the Lianggaoshan Formation shale ranges from 2.51123 to 2.53098, and the coefficient of determination (R^2) ranges from 0.97061 to 0.98639, signifying a relatively high degree of fitting. The fractal dimension is positively correlated with TOC content – lower TOC content corresponds to a simpler pore structure. Quartz, with its relatively regular and less complex pore structure, exhibits a negative correlation with the fractal dimension. Feldspar dissolution enhances the complexity of the shale pore structure, thereby presenting a positive correlation with the fractal dimension. Clay-mineral content, characterized by high pore complexity, is also positively correlated with the fractal dimension.

Data availability statement

All data used in this article are publicly available. No new data were created or analyzed in this study.

Acknowledgments

This research was supported by the Chongqing Natural Science Foundation of China (project No. CSTB2022NSCQ-MSX0333) and the Science and Technology Research Program of the Chongqing Municipal Education Commission (projects Nos KJZD-K202401205 and KJQN202401214). The publication costs of this article were partially covered by the Estonian Academy of Sciences.

References

1. Sun, S., Liang, S., Liu, Y., Liu, D., Gao, M., Tian, Y. et al. A review on shale oil and gas characteristics and molecular dynamics simulation for the fluid behavior in shale pore. *Journal of Molecular Liquids*, 2023, **376**, 121507. https://doi.org/10.1016/j.molliq.2023.121507
2. Lv, J., Jiang, F., Hu, T., Zhang, C., Huang, R., Hu, M. et al. Control of complex lithofacies on the shale oil potential in ancient alkaline lacustrine basins: the Fengcheng Formation, Mahu Sag, Junggar basin. *Geoenergy Science and Engineering*, 2023, **224**, 211501. https://doi.org/10.1016/j.geoen.2023.211501
3. Chen, H., Fang, D., Gu, H., Huang, W. Comprehensive evaluation of shale reservoir reconstruction based on microseismic and multidisciplinary integration. *Adsorption Science & Technology*, 2022, 5095254. https://doi.org/10.1155/2022/5095254
4. Cheng, G., Wu, C., Jiang, B., Li, F., Li, M., Song, Y. Pore structure evolution of organic-rich shale induced by structural deformation based on shale deformation experiments. *Energy*, 2024, **306**, 132463. https://doi.org/10.1016/j.energy.2024.132463
5. Jiang, X., Chen, M., Li, Q., Liang, L., Zhong, Z., Yu, B. et al. Study on the feasibility of the heat treatment after shale gas reservoir hydration fracturing. *Energy*, 2022, **254**, 124422. https://doi.org/10.1016/j.energy.2022.124422
6. Hu, S., Zhao, W., Hou, L., Yang, Z., Zhu, R., Wu, S. et al. Development potential and technical strategy of continental shale oil in China. *Petroleum Exploration and Development*, 2020, **47**(4), 877–887. https://doi.org/10.1016/S1876-3804(20)60103-3
7. Hu, L., Zhu, Y., Chen, S., Du, Z. Fractal characteristics of pore structure of shale in Shuanghe Longmaxi Formation, southern Sichuan Basin. *Xinjiang Petroleum Geology*, 2013, **34**(1), 79–82.
8. Sun, L., Liu, H., He, W., Li, G., Zhang, S., Zhu, R. et al. An analysis of major scientific problems and research paths of Gulong shale oil in Daqing Oilfield, NE China. *Petroleum Exploration and Development*, 2021, **48**(3), 527–540. https://doi.org/10.1016/S1876-3804(21)60043-5
9. Geng, Y., Liang, W., Liu, J., Cao, M., Kang, Z. Evolution of pore and fracture structure of oil shale under high temperature and high pressure. *Energy & Fuels*, 2017, **31**(10), 10404–10413. https://doi.org/10.1021/acs.energyfuels.7b01071
10. Liu, Z., Meng, Q., Dong, Q., Zhu, J., Guo, W., Ye, S. et al. Characteristics and resource potential of oil shale in China. *Oil Shale*, 2017, **34**(1), 15–41. https://doi.org/10.3176/oil.2017.1.02
11. Atchley, S. C., Crass, B. T., Prince, K. C. The prediction of organic-rich reservoir facies within the Late Pennsylvanian Cline shale (also known as Wolfcamp D), Midland Basin, Texas. *AAPG Bulletin*, 2021, **105**(1), 29–52. https://doi.org/10.1306/07272020010
12. Zheng, X., Zhang, B., Sanei, H., Bao, H., Meng, Z., Wang, C. et al. Pore structure characteristics and its effect on shale gas adsorption and desorption behavior.

Marine and Petroleum Geology, 2019, **100**, 165–178. https://doi.org/10.1016/j.marpetgeo.2018.10.045

13. Cheng, G., Wu, C., Jiang, B., Li, F., Li, M., Song, Y. Pore structure evolution of organic-rich shale induced by structural deformation based on shale deformation experiments. *Energy*, 2024, **306**, 132463. https://doi.org/10.1016/j.energy.2024.132463
14. Wang, Q., Hu, Q., Zhao, C., Zhang, C., Ilavsky, J., Yu, L. et al. Integrated experimental studies of pore structure and fluid uptake in the Bossier Shale in eastern Texas, USA. *Fuel*, 2025, **384**, 133926. https://doi.org/10.1016/j.fuel.2024.133926
15. Chen, S., Gong, Z., Li, X., Wang, H., Wang, Y., Zhang, Y. Pore structure and heterogeneity of shale gas reservoirs and its effect on gas storage capacity in the Qiongzhusi Formation. *Geoscience Frontiers*, 2021, **12**(6), 101244. https://doi.org/10.1016/j.gsf.2021.101244
16. Wang, X., Hou, J., Li, S., Dou, L., Song, S., Kang, Q. et al. Insight into the nanoscale pore structure of organic-rich shales in the Bakken Formation, USA. *Journal of Petroleum Science and Engineering*, 2020, **191**, 107182. https://doi.org/10.1016/j.petrol.2020.107182
17. Chen, X., Tang, X., Liu, C., Zhou, X., Guo, S., Yin, H. Implications of temperature for the modification of high-overmature shale reservoirs: experimental and numerical analysis. *SPE Journal*, 2024, **29**(08), 4218–4231. https://doi.org/10.2118/219762-PA
18. Hu, D., Wei, Z., Liu, R., Wei, X., Chen, F., Liu, Z. Enrichment control factors and exploration potential of lacustrine shale oil and gas: a case study of Jurassic in the Fuling area of the Sichuan Basin. *Natural Gas Industry B*, 2022, **9**(1), 1–8. https://doi.org/10.1016/j.ngib.2021.08.012
19. Hu, D., Wei, Z., Liu, R., Wei, X., Liu, Z., Chen, F. Major breakthrough of shale oil and gas in Well Taiye 1 in Bashansi Syncline in the Sichuan Basin and its significance. *China Petroleum Exploration*, 2021, **26**(2), 21–32. https://doi.org/10.3969/j.issn.1672-7703.2021.02.003
20. Fang, R., Jiang, Y., Sun, S., Luo, Y., Qi, L., Dong, D. et al. Controlling factors of organic matter accumulation and lacustrine shale distribution in Lianggaoshan Formation, Sichuan Basin, SW China. *Frontiers in Earth Science*, 2023, **11**, 1218215. https://doi.org/10.3389/feart.2023.1218215
21. Bai, X., Wang, X., Wang, M., Li, J., Lu, S., Yang, X. et al. Occurrence characteristics and factors that influence shale oil in the Jurassic Lianggaoshan Formation, northeastern Sichuan Basin. *Marine and Petroleum Geology*, 2025, **171**, 107197. https://doi.org/10.1016/j.marpetgeo.2024.107197
22. Wang, X., Wang, M., Zhao, C., Yang, X., Jia, Y., Wu, R. et al. Reservoir characteristics and controlling factors of the middle–high maturity multiple lithofacies reservoirs of the Lianggaoshan Formation shale strata in the northeastern Sichuan basin, China. *Marine and Petroleum Geology*, 2024, **161**, 106692. https://doi.org/10.1016/j.marpetgeo.2024.106692
23. He, W., He, H., Wang, Y., Cui, B., Meng, Q., Guo, X. et al. Major breakthrough

and significance of shale oil of the Jurassic Lianggaoshan Formation in Well Ping'an 1 in northeastern Sichuan Basin. *China Petroleum Exploration*, 2022, **27**(1), 40–49. https://doi.org/10.3969/j.issn.1672-7703.2022.01.004

24. Chen, S., Gao, X., Wang, L., Lu, J., Liu, C., Tang, H. et al. Factors controlling oiliness of Jurassic Lianggaoshan tight sands in central Sichuan Basin, SW China. *Petroleum Exploration and Development*, 2014, **41**(4), 468–474. https://doi.org/10.1016/S1876-3804(14)60053-7
25. Kane, O. I., Hu, M., Cai, Q., Deng, Q., Yang, W., Zuo, M. Sedimentary facies, lithofacies paleogeography, and an evaluation of the Ordovician sequences in the Sichuan Basin, southwest China. *Marine and Petroleum Geology*, 2023, **149**, 106096. https://doi.org/10.1016/j.marpetgeo.2023.106096
26. He, W., Bai, X., Meng, Q., Li, J., Zhang, D., Wang, Y. Accumulation geological characteristics and major discoveries of lacustrine shale oil in Sichuan Basin. *Acta Petrolei Sinica*, 2022, **43**(7), 885–898. https://doi.org/10.7623/syxb202207001
27. Schlanser, K., Grana, D., Campbell-Stone, E. Lithofacies classification in the Marcellus Shale by applying a statistical clustering algorithm to petrophysical and elastic well logs. *Interpretation*, 2016, **4**(2), 31–49. https://doi.org/10.1190/INT-2015-0128.1
28. Bhattacharya, S., Carr, T. R., Pal, M. Comparison of supervised and unsupervised approaches for mudstone lithofacies classification: case studies from the Bakken and Mahantango-Marcellus Shale, USA. *Journal of Natural Gas Science and Engineering*, 2016, **33**, 1119–1133. https://doi.org/10.1016/j.jngse.2016.04.055
29. Wang, D., Chen, C., Liu, Z., Yang, S., Liu, M., Xie, J. Main controlling factors for oil and gas enrichment in Jurassic laminated shale in Fuxing area of Sichuan Basin. *Petroleum Geology & Experimentation*, 2024, **46**(2), 319–332. https://doi.org/10.11781/sysydz202402319
30. Cheng, D., Zhang, Z., Hong, H., Zhang, S., Qin, C., Yuan, X. et al. Sequence structure, sedimentary evolution and their controlling factors of the Jurassic Lianggaoshan Formation in the East Sichuan Basin, SW China. *Petroleum Exploration and Development*, 2023, **50**(2), 293–305. https://doi.org/10.1016/S1876-3804(23)60388-X
31. Wang, Y., Zhou, S., Liang, F., Huang, Z., Li, W., Yan, W. et al. Reservoir space characterization of Ordovician Wulalike Formation in northwestern Ordos Basin, China. *Processes*, 2023, **11**(9), 2791. https://doi.org/10.3390/pr11092791
32. Zhou, X., Zhao, Z. Digital evaluation of nanoscale-pore shale fractal dimension with microstructural insights into shale permeability. *Journal of Natural Gas Science and Engineering*, 2020, **75**, 103137. https://doi.org/10.1016/j.jngse.2019.103137
33. Yan, H., Zhou, T., Zhou, X., Liu, X., Tang, X. Non-monotonic evolution and spatial reorganization mechanism of thermally induced micro-damage in sandstone. *Advances in Geo-Energy Research*, 2025, **17**(2), 135–148. https://doi.org/10.46690/ager.2025.08.05
34. IUPAC, I.U.O.P. Physical Chemistry Division Commission on Colloid and Surface Chemistry, Subcommittee on Characterization of Porous Solids:

Recommendations for the characterization of porous solids (technical report). *Pure and Applied Chemistry*, 1994, **66**(8), 1739–1758.

35. Pan, Y., Ji, B., Zhang, W., Knott, K., Xia, Y., Li, Q. et al. Topography and structural regulation-induced enhanced recovery of lithium from shale gas produced water via polyethylene glycol functionalized layered double hydroxide. *Journal of Industrial and Engineering Chemistry*, 2025, **145**, 372–383. https://doi.org/10.1016/j.jiec.2024.10.032
36. Wang, J., Zhang, P., Lu, S., Lin, Z., Li, W., Zhang, J. et al. Insights into microscopic oil occurrence characteristics in shales from the Paleogene Funing Formation in Subei Basin, China. *Petroleum Science*, 2025, **22**(1), 55–75. https://doi.org/10.1016/j.petsci.2024.07.025
37. Su, S., Cheng, C., Jiang, Z., Shan, X., Makeen, Y. M., Gao, Z. et al. Microscopic pore structure and connectivity of lacustrine shale of the Shahejie Formation, Zhanhua Sag, Bohai Bay Basin. *Geoenergy Science and Engineering*, 2023, **226**, 211800. https://doi.org/10.1016/j.geoen.2023.211800
38. Xu, Q., Liu, B., Ma, Y., Song, X., Wang, Y., Chen, Z. Geological and geochemical characterization of lacustrine shale: a case study of the Jurassic Da'anzhai member shale in the central Sichuan Basin, southwest China. *Journal of Natural Gas Science and Engineering*, 2017, **47**, 124–139. https://doi.org/10.1016/j.jngse.2017.09.008
39. Loucks, R. G., Ruppel, S. C., Wang, X., Ko, L., Peng, S., Zhang, T. et al. Pore types, pore-network analysis, and pore quantification of the lacustrine shale-hydrocarbon system in the Late Triassic Yanchang Formation in the southeastern Ordos Basin, China. *Interpretation*, 2017, **5**(2), 63–79. https://doi.org/10.1190/INT-2016-0094.1
40. Liang, F., Zhang, Q., Lu, B., Chen, P., Su, C., Zhang, Y. et al. Pore structure in shale tested by low pressure N_2 adsorption experiments: mechanism, geological control and application. *Energies*, 2022, **15**(13), 4875. https://doi.org/10.3390/en15134875
41. Medina-Rodriguez, B. X., Alvarado, V. Use of gas adsorption and inversion methods for shale pore structure characterization. *Energies*, 2021, **14**(10), 2880. https://doi.org/10.3390/en14102880
42. Mostefai, R., Kadri, M. M., Senoussi, E., Hacini, M., Awadh, S. M. Pore structure characterization of shale reservoir using nitrogen adsorption-desorption. *Iraqi Geological Journal*, 2023, **56**(1D), 1–13. https://doi.org/10.46717/igj.56.1D.1ms-2023-4-10
43. Spacapan, J. B., Ruiz, R., Manceda, R., D'Odorico, A., Rocha, E., Vera, E. R. et al. Oil production from a sill complex within the Vaca Muerta Formation. In *Integrated Geology of Unconventionals: The Case of the Vaca Muerta Play, Argentina* (Minisini, D., Fantín, M., Noguera, I. L., Leanza, H. A., eds). AAPG Memoir 121, 2020, Tulsa.
44. Gale, J. F. W., Fall, A., Yurchenko, I. A., Ali, W. A., Laubach, S. E., Eichhubl, P. et al. Opening-mode fracturing and cementation during hydrocarbon generation in shale: an example from the Barnett Shale, Delaware Basin, West Texas. *AAPG Bulletin*, 2022, **106**(10), 2103–2141. https://doi.org/10.1306/01062219274

45. Iltaf, K. H., Hu, Q., Fan, M., Oware, P., Wang, Q., Zhao, C. et al. Multiscale pore characterization of the New Albany Shale: insights from complementary analytical techniques. *Energy & Fuels*, 2025, **39**(22), 10356–10373. https://doi.org/10.1021/acs.energyfuels.5c00862
46. Garum, M., Glover, P. W. J., Lorinczi, P., Micklethwaite, S., Hassanpour, A. Integration of multiscale imaging of nanoscale pore microstructures in gas shales. *Energy & Fuels*, 2021, **35**(13), 10721–10732. https://doi.org/10.1021/acs.energyfuels.1c00554
47. Ruppert, L. F., Jubb, A. M., Headen, T. F., Youngs, T. G. A., Bandli, B. Impacts of mineralogical variation on CO_2 behavior in small pores from producing intervals of the Marcellus Shale: results from neutron scattering. *Energy & Fuels*, 2020, **34**(3), 2765–2771. https://doi.org/10.1021/acs.energyfuels.9b03744
48. Garum, M., Glover, P. W. J., Lorinczi, P., Drummond-Brydson, R., Hassanpour, A. Micro-and nano-scale pore structure in gas shale using Xμ-CT and FIB-SEM techniques. *Energy & Fuels*, 2020, **34**(10), 12340–12353. https://doi.org/10.1021/acs.energyfuels.0c02025
49. Fatah, A., Mahmud, H. B., Bennour, Z., Gholami, R., Hossain, M. The impact of supercritical CO_2 on the pore structure and storage capacity of shales. *Journal of Natural Gas Science and Engineering*, 2022, **98**, 104394. https://doi.org/10.1016/j.jngse.2021.104394
50. Sun, Y., Wang, Y., Liu, J., Wang, Y. A pyrolysis study of kerogen and extracted bitumen from a lacustrine shale of the Shahejie Formation and implications for in-situ conversion processes. *Journal of Analytical and Applied Pyrolysis*, 2024, **183**, 106735. https://doi.org/10.1016/j.jaap.2024.106735
51. Shi, S., Wang, Y., Chen, C., Liu, J., Peng, P. Influence of tectonic evolution processes on burial, thermal maturation and gas generation histories of the Wufeng-Longmaxi shale in the Sichuan Basin and adjacent areas. *International Journal of Coal Geology*, 2024, **295**, 104642. https://doi.org/10.1016/j.coal.2024.104642
52. Slatt, R. M., O'Brien, N. R. Pore types in the Barnett and Woodford gas shales: contribution to understanding gas storage and migration pathways in fine-grained rocks. *AAPG Bulletin*, 2011, **95**(12), 2017–2030. https://doi.org/10.1306/03301110145
53. Pfeifer, P., Avnir, D. Chemistry in noninteger dimensions between two and three. I. Fractal theory of heterogeneous surfaces. *The Journal of Chemical Physics*, 1983, **79**(7), 3558–3565. https://doi.org/10.1063/1.446210
54. Li, K., Zeng, F., Cai, J., Sheng, G., Xia, P., Zhang, K. Fractal characteristics of pores in Taiyuan formation shale from Hedong coal field, China. *Fractals*, 2018, **26**(02), 1840006. https://doi.org/10.1142/S0218348X18400066
55. Yang, F., Ning, Z., Liu, H. Fractal characteristics of shales from a shale gas reservoir in the Sichuan Basin, China. *Fuel*, 2014, **115**, 378–384. https://doi.org/10.1016/j.fuel.2013.07.040

Oil Shale, 2026, 43, 1, 54–74 https://doi.org/10.3176/oil.2026.1.03

Major, trace, and rare earth elements geochemistry and enrichment in the Neogene organic-rich sediments from the Aleksinac deposit (Serbia): Part A

Gordana Gajica(a)*, Aleksandra Šajnović(a), Ksenija Stojanović(b), Milan D. Antonijević(c), Aleksandar Kostić(d), Branimir Jovančićević(b)

(a) Center of Chemistry – Institute of Chemistry, Technology and Metallurgy, University of Belgrade, Njegoševa 12, 11000 Belgrade, Serbia
(b) Faculty of Chemistry, University of Belgrade, Studentski trg 12-16, 11000 Belgrade, Serbia
(c) School of Chemistry and Chemical Engineering, University of Surrey, Guildford, Surrey GU2 7XH, United Kingdom
(d) Faculty of Mining and Geology, University of Belgrade, Đušina 7, 11000 Belgrade, Serbia

Received 30 April 2025, accepted 23 January 2026, available online 29 January 2026

Abstract. *The composition of inorganic matter and the enrichment of trace and rare earth elements (TEs and REEs) in the Neogene organic matter-rich sediments in the Upper layer of the Aleksinac deposit (Dubrava block, Serbia) were analysed. Correlation analysis clearly showed that TEs and REEs are associated with* SiO_2, Al_2O_3, K_2O, *and* TiO_2, *clastic minerals, clay, and feldspar, as well as zeolite minerals natrolite and analcime, indicating that the TEs and REEs were brought into the basin mainly by clastic material. Their distribution indicates certain changes in the depositional environment during the formation of these sediments. According to enrichment factors (calculated in relation to World Oil Shales, Upper Continental Crust, and Post-Archaean Australian Shale) and the degree of enrichment (relative to argillaceous rocks), the Aleksinac oil shale shows significant enrichment in Mo, a lesser degree in Sr, and possible enrichment in Cu. Therefore, there are no concerns regarding toxic trace elements in the Aleksinac oil shale.*

Keywords**:** *mineral composition, geochemical association of elements, enrichment factors, degree of enrichment.*

---

* Corresponding author, gordana.gajica@ihtm.bg.ac.rs

1. Introduction

Oil shales are the subject of numerous research activities due to their economic importance as a potential energy source and industrial raw material, since they represent an important reservoir of organic carbon and trace elements. The inorganic matter makes up the largest part of the oil shale, while the organic matter (OM) is dispersed within it, most often forming a homogeneous mixture. Generally, oil shales are characterised by fine lamination in which laminae of mixed organic and mineral matter, and pure mineral material alternate [1]. Oil shales vary in the content of the inorganic part, which commonly ranges from 60% to 90% [2].

As the prevalent part of oil shale comprises inorganic matter, the analysis of mineral and chemical composition (major, trace, and rare earth elements) is important for utilisation, economic-geological, environmental, and geochemical aspects. Oil shales enriched in certain elements can be used as a mineral raw material in metallurgy. From the economic-geological assessment of oil shale deposits, the content of certain individual elements (e.g. V, Zn, Cu, and U) may contribute to its greater value. On the other hand, during the exploitation and processing of oil shales, there is a possible mobilisation and concentration of elements, leading to their release into the water, air, and soil. This is undesirable from the aspect of environmental protection and can have a negative impact on the environment and health, especially if certain elements are present in high concentrations [3–9].

The trace and rare earth elements (TEs and REEs, respectively) are present in low concentrations in oil shale; they do not exist independently and can be found in the form of organometallic compounds, embedded in the crystal structure of minerals, or in a dispersed state on clay and oxyhydroxide particles [10]. It has been proven that oil shales can be enriched in certain TEs and REEs, as can other OM-rich sediments, e.g. coals [7, 11, 12]. Elevated concentrations of certain elements in oil shales can be determined by comparing their contents with some ‘standard values’. The most commonly used ‘standard values’ are the composition of the Upper Continental Crust (UCC) [13–18], Post-Archaean Australian Shale (PAAS) [13], North American Shale (NASC) [19–21], the average World Oil Shales (WOS) [22–26], and argillaceous rocks [26]. The TEs enrichment and geochemical investigation of OM-rich sediments also require an analysis of major element distribution, as these elements are diagenetically stable and can reflect the sedimentary background (terrigenous detrital influence) [27].

The Aleksinac oil shale deposit is the largest and richest oil shale deposit in Serbia and has significant economic importance [4, 28]. Therefore, it is the most investigated oil shale in Serbia, but studies on its inorganic composition are rare. The aims of this study were to determine: (i) the composition of inorganic matter; (ii) the geochemical association of elements; and (iii) the enrichment of TEs and REEs. Outcrop samples from the Upper layer of the Dubrava block of the Aleksinac deposit were selected for this study. The study's findings may be useful for future exploration and utilisation of oil shales.

2. Samples and analytical methods

2.1. Samples and geological background

The Aleksinac deposit was formed within the Great Moravian–South Moravian Depression during the Neogene, within a lake basin that developed due to tectonic activities, climatic conditions, and the inflow of water and clastic material [28, 29]. According to some authors [29, 30], the area of the Aleksinac basin was located on two geotectonic units, the Carpatho-Balkanides and the Serbian–Macedonian Massif, and the lake sediments were deposited in tectonic depressions formed by the fragmentation of these two geotectonic units. The Aleksinac basin is filled with Lower and Upper Miocene lake sediments. However, oil shales were formed only during the Lower Miocene [3]. These sediments are characterised by the rhythmic appearance of different lithological units and oil shales, indicating frequent sedimentation changes [29]. The Lower Miocene sediments are of lacustrine origin: they start with red conglomerates, overlain by alluvial–lacustrine sandstones, with some sandy shale and siltstone in the upper layers. Above these sediments, two layers of oil shales (Lower and Upper) were deposited, with the Aleksinac Main coal seam located between them. A layer of Upper Miocene marl, clay, sand, and conglomerate unconformably covers the Lower Miocene complex. As a result of complex tectonic movements, the Aleksinac deposit is divided by fault zones into three main blocks from north to south: Dubrava, Morava, and Logorište [3, 30, 31]. According to certain characteristics of organic matter and mineral base, the Aleksinac deposit is closest to the Green River shale, in which the deposition of sedimentary rocks took place in a shallow reducing environment of a stratified, brackish–saline alkaline lake [3, 29].

For this study, sediment samples were taken from the Dubrava block, from the outcropping Upper oil shale layer. Sixteen samples (D1–D16) were collected as discontinuous channel samples comprising a 250 m thick series, from the top of the bituminous marl sequence to the bottom of the Upper oil shale layer, just above the Main coal seam. The Upper oil shale layer is much thicker and more accessible, and thus easier for exploitation and processing. A detailed description of the lithostratigraphic column of the analysed samples is provided in previous publications [32, 33].

Based on mineral composition, eight samples are defined as marlstones (D2, D3, D5, D8, D12–D15), five as mudstones (D1, D4, D6, D7, D9), two as calcareous mudstones (D10, D11), and one as calcareous marlstone (D16; Table 1) [33].

2.2. Analytical methods

2.2.1. Inductively coupled plasma optical emission spectroscopy

The content of major elements was determined by inductively coupled plasma optical emission spectroscopy (ICP-OES, Thermo iCAP 6500). Lithium metaborate ($LiBO_2$) fusion was used to prepare sample solutions for the analysis. The samples were mixed with $LiBO_2$ flux in graphite crucibles, and the crucibles were then fused in a furnace at 900 °C for 15 min. After cooling, the content from the crucibles was transferred into plastic bottles and dissolved with 150 cm^3 of 3.5% HNO_3. The samples were mixed using a magnetic stirrer for an hour, then filtered and dissolved with deionised water to a volume of 250.00 cm^3.

2.2.2. Inductively coupled plasma mass spectrometry

The content of 39 TEs and REEs was determined by inductively coupled plasma mass spectrometry (ICP-MS, Thermo X Series II ICP-MS). The samples were prepared in the same way as for ICP-OES analysis. From the obtained solution, 0.25 cm^3 was placed in a test tube and supplemented with an internal standard solution to a volume of 5.00 cm^3. The internal standard solution contained 1.05 cm^3 of Rh solution (concentration 10 ppm Rh in 3% HNO_3), 60 cm^3 of concentrated nitric acid, and deionised water to a total volume of 2000 cm^3. A rack of samples on both instruments (ICP-OES and ICP-MS) comprised, in addition to samples, three analytical blanks, one internal reference material (BEN), four certified reference materials (OU, SCO, ACE, and GCN), and two standards (QC1 and QC2), which enabled a quick check of analytical quality. Before analysing the prepared blanks, standards, and samples, a high-purity standard (SD12) was used for instrument calibration and stabilisation. ICP-OES and ICP-MS measurements were carried out in triplicate.

2.2.3. Rock-Eval pyrolysis, elemental analysis, and XRD analysis

The total organic carbon (TOC) content was determined by Rock-Eval pyrolysis using a Rock-Eval 6 Standard analyser. The content of total sulphur (TS) was measured with an elemental analyser (Vario EL III, CHNOS Elemental Analyser, Elementar Analysensysteme GmbH). The mineral composition was analysed with an XRD analyser (Bruker D8 Advance diffractometer). The semi-quantitative mineral composition was obtained using TOPAS Rietveld refinement software. Detailed procedures for these analyses are provided in a previous paper [33].

2.3. Data analysis and calculation

Cluster analysis was performed using SPSS 20 to group the samples based on similarities and differences. The same program was also used for the correlation analysis of parameters, while Microsoft Excel 2013 and Origin 2016 were applied for correlation between a smaller number of elements and for graphical presentation. Principal component analysis (PCA) was performed in Minitab 17 to reduce the number of variables necessary to describe the dataset, to visualise the data structure, and to determine the association of elements more easily.

Due to the low concentrations of TEs and REEs, an enrichment factor (EF) is used to follow their distributions. The EF is used to describe the enrichment of an element in sedimentary rocks ($EF_{\text{element X}}$), calculated as the ratio of the concentration of an element (X) in the analysed sample to its content in certain 'standard samples'. To minimise the dilution effect of OM and authigenic minerals, element concentrations are normalised to Al, due to its resistance to alteration processes. If Al resides within the detrital clay fraction of the sediments (determined by the correlation of Al with Ti), it is appropriate to use Al content for normalisation [34, 35]:

$$EF_{\text{element X}} = (X/Al)_{\text{sample}}/(X/Al)_{\text{standard}}. \tag{1}$$

Furthermore, solid fossil fuels can be characterised based on the degree of enrichment with a certain element (Q_i) in relation to the concentration of that element ($K1i$) in argillaceous rocks (the most abundant sedimentary rock type, including oil shale) [25]:

$$Q_i = C_i/K_{1i}, \tag{2}$$

where C_i is the average concentration of the i^{th} element in the dry samples. According to Q_i values, caustobiolites (fossil combustible substances) are classified into five groups: (i) < 0.6 = noticeably depleted in TEs; (ii) 0.6–1.4 = differ little in the amount of TEs; (iii) 1.4–2.0 = enriched in TEs to a certain extent; (iv) 2.0–3.5 = noticeably enriched in TEs; and (v) > 3.5 = considerably enriched in TEs [25].

3. Results and discussion

3.1. Mineralogy and geochemistry of the investigated samples

3.1.1. Mineral composition

The semi-quantitative mineral composition of samples is presented in Figure 1. Samples D1–D15 have similar mineral compositions, while sample D16 notably differs.

Samples D1–D15 show variations in the concentrations of clays, feldspars, quartz, carbonates, analcime, and natrolite (Fig. 1). The elevated content of carbonate minerals distinguishes D2 and D13. The highest content of clay minerals is found in samples D1, D6, D7, D9, and D10. The highest amount of quartz is observed in samples D2, D5, and D13; it is present in a very low

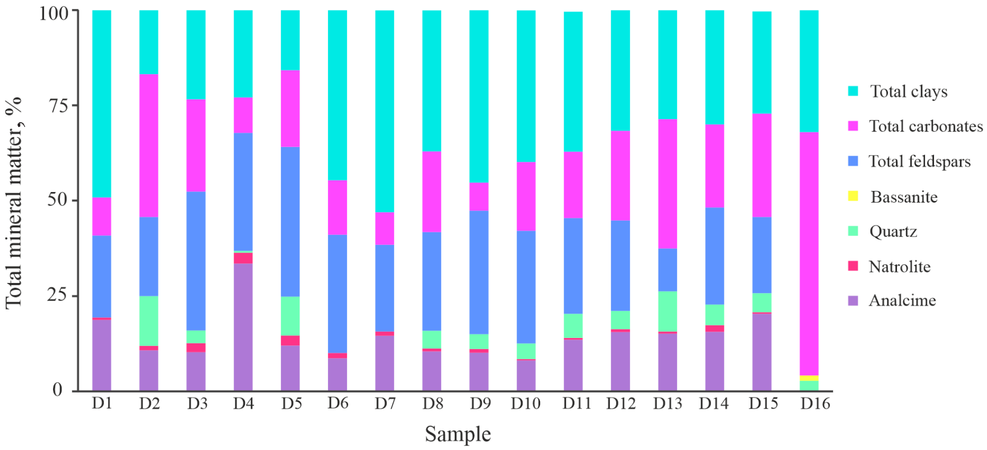

Fig. 1. Semi-quantitative mineral composition.

amount (0.48 wt%) in sample D4, while quartz is absent in samples D1, D6, and D7. The highest content of feldspar minerals characterises samples D3–D6 and D9. An elevated content of analcime is found in sample D4, followed by samples D1 and D15. The highest content of natrolite is present in samples D3–D5.

The uniqueness of sample D16 is reflected in its significantly higher content of authigenic carbonate minerals (accounting for 63.87 wt% of the total mineral matter), the absence of terrigenous detrital minerals (feldspars) and zeolite minerals (analcime and natrolite), and the presence of the sulphate mineral bassanite, which is identified only in this sample.

3.1.2. Major elements

The contents of major elements in the analysed samples, together with TOC and TS, are listed in Table 1.

Among the major elements, SiO_2, Al_2O_3, Fe_2O_3, and CaO are the most abundant, whereas TiO_2, MnO, and P_2O_5 are the least abundant (concentration <1 wt%; Table 1). SiO_2 and Al_2O_3 prevail in samples D1–D15, while CaO dominates in sample D16. This is consistent with the mineral composition of the analysed samples (Fig. 1). Samples D1–D15 are characterised by increased content of constituents of clastic minerals SiO_2, Al_2O_3, K_2O, and TiO_2, followed by Fe_2O_3. Al_2O_3 and SiO_2 are most abundant in clay minerals and quartz (SiO_2). In contrast, sample D16 is characterised by the prevalence of CaO, which is in accordance with the dominance of carbonate minerals (Fig. 1; Table 1). Furthermore, sample D16 has a lower content of all other major elements. The elevated content of MgO in samples D1–D15 compared to D16 (Fig. 1; Table 1) can be explained by the presence of dolomite in all samples except D16 [33].

Table 1. Lithology, total organic carbon, total sulphur, and major elements, wt%

Sample	Lithology	TOC	TS	Al_2O_3	SiO_2	TiO_2	Fe_2O_3	K_2O	Na_2O	MgO	CaO	MnO	P_2O_5
D1	Mdst	2.85	0.13	17.85	42.98	0.76	8.35	3.27	3.69	3.42	5.35	0.10	0.40
D2	Mrl	7.06	0.21	9.09	31.99	0.45	4.90	2.10	1.69	7.80	13.08	0.12	0.15
D3	Mrl	3.87	0.18	13.23	36.32	0.66	7.57	3.41	1.63	6.12	9.89	0.11	0.12
D4	Mdst	1.79	0.13	17.93	44.57	0.77	9.67	3.18	4.28	2.53	4.26	0.11	0.27
D5	Mrl	5.44	0.23	13.63	42.27	0.62	5.24	3.68	1.45	4.66	8.08	0.08	0.06
D6	Mdst	1.31	0.13	17.50	43.99	0.87	7.13	4.36	2.10	3.63	7.36	0.12	0.17
D7	Mdst	1.88	0.13	17.31	45.30	0.79	8.83	3.31	3.17	3.56	4.76	0.11	0.20
D8	Mrl	5.20	0.15	12.97	38.11	0.62	6.16	3.44	2.08	4.43	10.78	0.11	0.14
D9	Mdst	5.10	0.09	16.05	45.45	0.75	7.90	3.79	2.13	4.48	4.20	0.10	0.05
D10	CalcMdst	8.22	0.08	13.08	34.91	0.67	6.75	3.07	1.69	4.77	7.70	0.10	0.43
D11	CalcMdst	3.83	0.07	14.02	40.95	0.63	8.23	3.35	2.14	4.99	7.37	0.09	0.04
D12	Mrl	7.20	0.08	12.30	36.07	0.59	6.23	2.82	2.17	5.01	9.99	0.11	0.09
D13	Mrl	13.10	0.21	8.67	29.93	0.43	4.62	1.76	2.02	6.87	10.92	0.08	0.06
D14	Mrl	4.01	0.06	13.05	39.00	0.64	7.50	2.98	1.94	7.52	8.32	0.11	0.05
D15	Mrl	8.61	0.14	11.76	33.48	0.57	6.53	2.77	2.61	5.81	10.20	0.10	0.19
D16	CalcMrl	29.10	6.11	5.13	17.74	0.15	2.54	1.08	0.25	1.63	36.13	0.04	0.05

Abbreviations: Mdst – mudstone; Mrl – marlstone; CalcMdst – calcareous mudstone; CalcMrl – calcareous marlstone.

Samples D1, D4, D6, D7, and D9 show the highest content of clastic mineral constituents such as Al_2O_3, SiO_2, and TiO_2 [36–38]. Some of these samples (D4, D6, D7) have the lowest TOC, probably due to the dilution effect of OM with clastic material (Table 1). The highest TOC content characterises sample D16, while samples D2, D10, D12, D13, and D15 also have relatively high TOC.

On the basis of the major element contents, the same conclusion can be drawn as from the mineral composition: there was a significant change in the diagenetic environment after the deposition of the sediments represented by sample D16, and also certain less pronounced variations during the formation of the sediments represented by samples D15–D1.

3.1.3. Trace elements

The contents of TEs in the analysed samples are listed in Table 2. Based on TE contents, sample D16 again differs significantly from samples D1–D15 (Table 2). Sample D16 is characterised by lower concentrations of almost all analysed TEs, while only Cs, Sr, Cr, and Ni are found in higher concentrations compared to samples D1–D15 (Table 2).

The obtained result can be attributed to changes in the origin of sedimentary material and/or depositional conditions after the sediment deposition represented by sample D16 (see Sections 3.1.1 and 3.1.2) [33]. Moreover, this sample originated from the oil shale layer just above the Main coal seam. In sedimentological terms, this shift indicates a change in the depositional environment, since different conditions are necessary for their formation, probably reflecting a transition from a wetland to a lacustrine environment.

The variations in analysed TE concentrations among samples D1–D15 indicate certain changes in the depositional environment during sediment formation. Within this group, samples D1, D4, D6, and D7 stand out due to their elevated concentrations of most analysed TEs. In contrast, samples D2 and D13 are characterised by the lowest TE concentrations. This pattern is more visible on the dendrogram, which shows that the analysed samples are divided into two main clusters: D1–D15 (I) and D16 (II; Fig. 2a).

Samples D1–D15 are further divided into two subclusters. The first subcluster (Ia) includes samples D3, D5, D8, D10–D12, D14, and D15, as well as samples D2 and D13, which show slight separation, more pronounced in sample D13. The second subcluster (Ib) comprises samples D1, D4, D6, D7, and D9. The results are almost identical whether the cluster analysis is conducted based only on TE contents (Fig. 2a) or using the contents of major, trace, and rare earth elements, total organic carbon, and total sulphur (Fig. 2b).

Table 2. Contents of trace elements, ppm

Element	D1	D2	D3	D4	D5	D6	D7	D8	D9	D10	D11	D12	D13	D14	D15	D16
Rb	107.15	74.71	109.65	89.14	118.05	120.25	102.55	104.05	134.45	102.95	121.95	91.65	70.82	127.45	90.35	68.56
Cs	8.60	5.75	7.45	9.69	7.95	8.26	8.72	7.07	9.32	7.91	9.32	6.49	4.84	8.94	6.20	41.55
Be	2.31	1.30	2.04	2.45	1.71	2.25	2.25	1.91	2.28	2.03	1.96	1.65	1.19	1.93	1.63	0.66
Sr	297.00	743.00	581.00	260.00	469.00	444.00	365.00	585.00	256.00	470.00	458.00	504.00	644.00	480.00	532.00	1592.00
Ba	473.67	391.05	490.85	512.30	412.10	592.64	536.33	437.62	425.90	481.22	406.74	427.79	381.51	435.34	420.84	339.91
Sc	12.94	11.02	17.48	26.58	9.86	16.01	16.12	13.71	15.73	15.84	13.17	12.95	11.73	16.64	13.74	5.70
Zr	47.78	31.34	40.29	44.31	41.46	74.79	51.72	59.29	47.08	43.02	46.78	39.71	30.11	46.48	38.07	21.30
Hf	1.36	1.08	1.35	1.38	1.36	2.26	1.54	1.90	1.75	1.31	1.32	1.30	0.95	1.63	1.20	0.78
V	156.00	98.00	145.00	217.00	129.00	117.00	183.00	135.00	187.00	144.00	149.00	134.00	104.00	174.00	142.00	55.00
Nb	9.92	5.95	8.59	9.73	8.46	11.03	9.94	8.22	9.48	8.77	8.41	7.80	5.70	8.60	7.48	3.24
Ta	0.71	0.42	0.62	0.72	0.61	0.80	0.73	0.64	0.70	0.62	0.60	0.57	0.41	0.62	0.53	0.23
Cr	92.23	53.66	82.06	99.85	75.69	91.42	92.83	74.77	93.17	79.61	85.81	76.72	57.73	84.94	74.18	179.64
Mo	56.67	4.85	10.96	18.65	12.81	7.12	19.64	5.18	10.93	6.34	26.71	8.32	22.81	12.82	12.21	1.48
W	2.77	0.91	1.52	2.10	0.43	1.74	2.44	0.79	1.66	1.03	0.67	0.83	0.38	1.20	0.68	1.47
Co	22.34	13.03	19.91	18.07	16.22	16.21	20.25	16.69	20.47	13.94	22.94	19.86	14.12	23.42	20.70	19.83
Ni	51.27	27.50	45.52	33.11	42.35	35.85	48.43	38.75	50.49	39.88	54.17	46.85	35.77	49.04	40.25	372.09
Cu	112.34	60.58	82.52	136.17	77.30	76.49	107.10	57.71	112.64	79.38	98.72	86.41	53.90	86.36	70.51	21.59
Zn	141.00	57.00	92.00	110.00	85.00	91.00	131.00	89.00	112.00	96.00	104.00	83.00	75.00	103.00	91.00	30.00
Ga	24.25	12.55	18.43	24.07	18.72	23.40	23.00	17.68	21.63	18.53	18.95	16.78	12.10	18.48	16.56	5.94
Tl	0.56	0.28	0.41	0.48	0.37	0.59	0.57	0.39	0.46	0.36	0.45	0.33	0.23	0.40	0.33	0.27
Sn	2.81	1.39	2.15	2.82	2.66	2.77	2.76	2.07	2.50	2.17	2.48	1.88	1.35	2.21	2.12	0.72
Pb	29.78	12.07	21.82	44.05	16.61	27.57	34.98	14.83	21.43	14.60	20.14	17.62	7.62	14.91	13.79	2.65
Th	12.46	8.50	10.54	18.26	6.87	12.42	14.99	11.03	6.55	16.39	3.30	8.20	8.57	4.77	10.12	3.22
U	10.66	5.59	3.62	7.54	1.95	4.07	4.74	3.54	2.36	6.83	1.57	2.43	2.36	1.64	6.04	1.75
Y	24.99	16.29	20.28	34.12	11.99	25.74	26.62	20.00	16.28	28.39	10.95	16.49	15.12	12.02	18.61	7.27

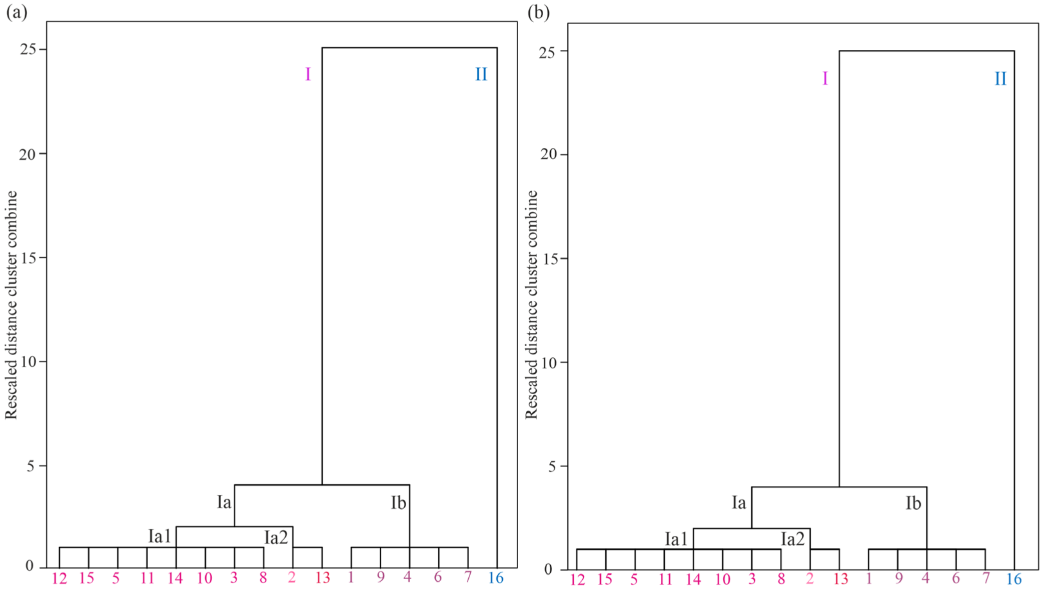

Fig. 2. Dendrograms of the studied samples derived from cluster analysis: (a) contents of trace elements and (b) contents of major, trace, and rare earth elements, total organic carbon, and total sulphur.

3.1.4. Rare earth elements

The contents of REEs in the analysed samples are listed in Table 3. REEs are present at lower concentrations in sample D16 compared to samples D1–D15 (Table 3; Fig. 3). Differences among samples D1–D15 can also be observed. Samples D4, D6, and D7, followed by sample D1, have higher concentrations of REEs, whereas samples D2, D5, D11, D13, and D14 contain lower amounts. Furthermore, sample D4 shows elevated concentrations of all REEs except Yb, which has the highest concentration in sample D1. Since samples D4, D6, and D7 are characterised by relatively high contents of clastic constituents (see Sections 3.1.1 and 3.1.2), it can be assumed that the REEs were probably delivered into the depositional environment with clastic material.

Generally, in the analysed samples, light earth elements (LREEs) are more abundant than heavy rare earth elements (HREEs; Table 3), which is in agreement with the typical distribution of REEs in oil shale [20, 37–40]. Based on PAAS-normalised REEs curves [13], it is also evident that sample D16 is clearly distinguished, as are samples D4, D6, and D7 (Fig. 3). The samples show no strong Ce anomalies, whereas several samples display negative Eu anomalies (D2–D4, D9, D11, D12, D14; Fig. 3).

Table 3. Contents of rare earth elements, ppm

Element	D1	D2	D3	D4	D5	D6	D7	D8	D9	D10	D11	D12	D13	D14	D15	D16
La	28.71	19.80	27.45	37.36	22.02	33.54	35.73	27.22	25.09	24.84	17.37	25.98	20.40	20.88	24.92	10.60
Ce	51.95	35.44	51.78	73.98	40.62	70.89	66.75	49.23	44.09	48.43	34.44	48.15	35.25	35.89	45.23	16.59
Pr	6.52	4.43	6.40	9.03	4.77	8.31	8.49	5.98	5.51	6.07	4.29	5.92	4.41	4.35	5.55	1.91
Nd	24.73	16.72	24.14	34.56	17.93	32.27	32.27	22.60	20.64	23.92	16.18	22.65	17.45	16.32	21.08	6.98
Sm	5.14	3.49	5.13	7.38	3.59	6.81	6.69	4.69	4.14	5.21	3.06	4.43	3.60	3.27	4.36	1.46
Eu	1.04	0.69	1.00	1.48	0.71	1.35	1.33	0.95	0.80	1.11	0.58	0.89	0.75	0.63	0.89	0.34
Gd	4.42	3.10	4.35	6.59	3.02	5.78	5.79	4.21	3.55	5.02	2.50	3.99	3.31	2.82	3.93	1.30
Tb	0.76	0.50	0.73	1.13	0.47	0.96	0.94	0.70	0.59	0.89	0.40	0.65	0.57	0.45	0.65	0.21
Dy	4.64	2.99	4.08	6.57	2.58	5.42	5.47	3.96	3.32	5.44	2.20	3.55	3.20	2.46	3.68	1.22
Ho	0.95	0.63	0.80	1.34	0.48	1.00	1.03	0.79	0.63	1.11	0.45	0.66	0.61	0.48	0.71	0.25
Er	3.09	1.94	2.24	3.92	1.29	2.81	2.87	2.22	1.74	3.13	1.29	1.76	1.61	1.36	2.08	0.73
Tm	0.49	0.30	0.32	0.54	0.18	0.38	0.39	0.33	0.24	0.46	0.19	0.23	0.21	0.20	0.30	0.10
Yb	3.66	2.00	1.98	3.17	1.18	2.40	2.38	2.07	1.57	3.12	1.26	1.44	1.29	1.35	1.89	0.71
Lu	0.56	0.29	0.29	0.44	0.18	0.35	0.34	0.33	0.23	0.44	0.19	0.22	0.19	0.20	0.27	0.10
LREEs	118.09	80.57	115.9	163.79	89.64	153.17	151.26	110.67	100.27	109.58	75.92	108.02	81.86	81.34	102.03	37.88
HREEs	18.57	11.75	14.79	23.70	9.38	19.10	19.21	14.61	11.87	19.61	8.48	12.50	10.99	9.32	13.51	4.62
∑REEs	136.66	92.32	130.69	187.49	99.02	172.27	170.47	125.28	112.14	129.19	84.40	120.52	92.85	90.66	115.54	42.50

Light rare earth elements (LREEs) = (La + Ce + Pr + Nd + Sm + Eu); heavy rare earth elements (HREEs) = (Gd + Tb + Dy + Ho + Er + Tm + Yb + Lu); ∑REEs = LREEs + HREEs.

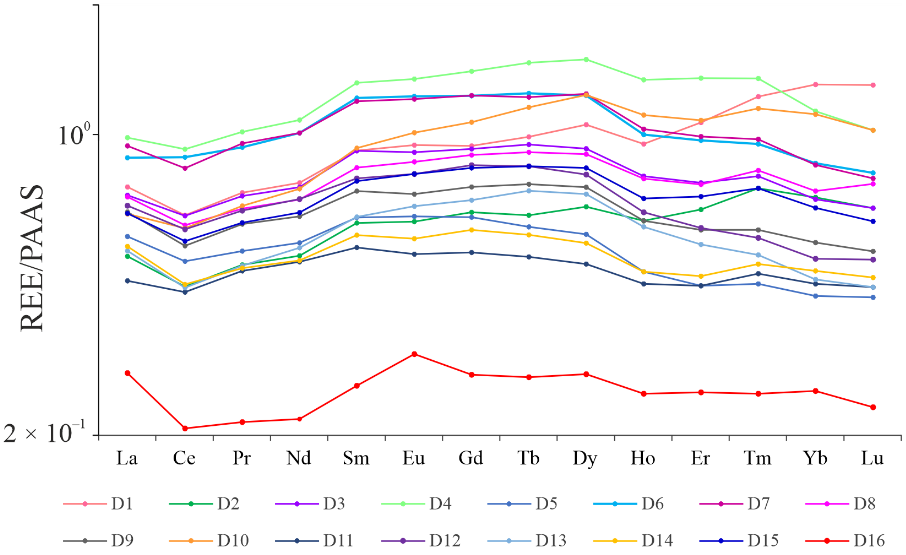

Fig. 3. Distribution of rare earth elements.

3.2. Geochemical association of trace and rare earth elements

The organic and inorganic matter of oil shale may host sedimentary accumulations of TEs and REEs. Their correlations with OM (i.e. TOC content) and the contents of inorganic components were performed for samples D1–D15, which originated from the same facies.

Regarding the OM, the correlation analysis shows that almost all TEs and REEs exhibit statistically significant negative correlations with TOC. A statistically significant positive correlation with TOC is observed for Sr only (at a significance level $p < 0.05$), whereas Cs, Be, Ba, Zr, Nb, Ta, Cr, W, Cu, Ga, Tl, Sn, and Pb ($p < 0.01$); Rb, Hf, V, and Zn ($p < 0.05$) from TEs; and La, Ce, Pr, Nd, and Sm ($p < 0.05$) from REEs showed significant negative correlations with TOC. This leads to the assumption that TEs are not associated with the OM of the examined sediments.

Statistically significant positive correlations with TOC are observed for major elements CaO and MgO ($p < 0.05$), as well as for carbonates and quartz ($p < 0.01$), whereas SiO_2, Al_2O_3, K_2O, TiO_2, and Fe_2O_3 exhibited negative correlations ($p < 0.01$). Considering that carbonate minerals have an authigenic origin, while quartz can have both authigenic and detrital origins, these correlations could imply that part of the quartz in the investigated samples has an authigenic origin [41, 42].

This is clearly evident in the loading plot obtained from the PCA (Fig. 4). The PCA resulted in a two-component model explaining 44.44% of the total

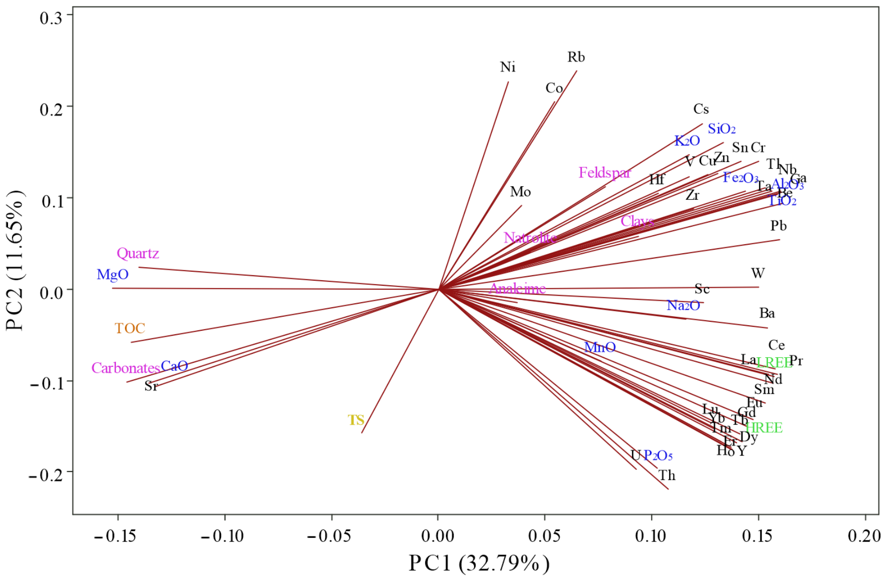

Fig. 4. Loading plot based on principal component analysis of minerals, major, trace and rare earth elements, TOC, and TS composition.

variance in the investigated dataset (minerals, major, trace, and rare earth elements, TOC, TS). The first principal component (PC1) accounted for 32.79% of the overall data variance, whereas the second (PC2) accounted for 11.65%.

Regarding the inorganic part, most of the examined TEs show statistically significant positive correlations with constituents of clastic minerals (SiO_2, Al_2O_3, K_2O, and TiO_2), clastic minerals (clay and feldspar), the zeolite mineral natrolite, and some TEs with analcime. On the other hand, negative correlations are observed between TEs and TOC, CaO, MgO, carbonate minerals, and quartz (Fig. 4). This confirms that TEs were brought into the basin mainly by clastic material, as expected.

The concentration of REEs shows statistically significant positive correlations with constituents of clastic minerals (Al_2O_3, TiO_2, SiO_2), followed by P_2O_5, Fe_2O_3, and Na_2O, but negative correlations with TOC, CaO and MgO, carbonate minerals, and quartz. Furthermore, LREEs and HREEs exhibit some differences in correlations. Namely, LREEs and HREEs show different significance of positive correlations with Na_2O: the LREEs demonstrate a positive correlation with SiO_2 ($p < 0.05$) and TiO_2 ($p < 0.01$), whereas the HREEs display a positive correlation with P_2O_5 ($p < 0.01$) and TiO_2 ($p < 0.05$; Fig. 4). Positive correlations of U and Th with P_2O_5 might indicate the presence of phosphate minerals monazite, xenotime, and apatite, together with heavy minerals (ilmenite, leucoxene, rutile, zircon) [43]. It is known that these minerals can be the source of REEs, as well as U and Th [44, 45]. Since XRD analysis is not sensitive to less than 5 wt% of the crystalline phase present in the sample, it can be presumed that this technique did not identify the minerals mentioned above due to their low content.

3.3. Trace and rare earth elements enrichment

The average trace element concentrations of the analysed oil shales (AOS), the average World Oil Shales (WOSsp [25], WOSw [21, 22]), Upper Continental Crust (UCC, [12, 13, 16]), Post-Archaean Australian Shale (PAAS, [12]), and argillaceous rocks (K1i, [25]) are presented in Table 4. The enrichment factor (EF) and the degree of enrichment (Qi) are used to assess elemental enrichment in sedimentary rocks. The calculated EF and Qi of the analysed elements in the Aleksinac oil shales are given in Table 4. Furthermore, the range of element concentrations in oil shale ash from different deposits in Jordan (JOSa; Attarat Umm Al-Ghudran, El-Lajjun, Sultani, Jurf Al-Drawaish, Assfar Al-Mahata, Wadi Abu-Hmam, and Al-Shalaleh, [46]) are also presented in Table 4.

Based on the EF, meaningful enrichment of an element starts from values >3 [10], while if EF > 1, it can be only considered as a detectable enrichment [47]. In the analysed sample set for TEs, EF >3 is found for Mo (in relation to WOSsp*, WOSw, UCC, PAAS), Sr (PAAS), and Cu (UCC; Table 4; Fig. 5). Therefore, it can be said that Mo shows significant enrichment, Sr to a lesser degree, and Cu to a possible degree.

Among REEs, some elements (Pr, Sm, Eu, Tb, Ho, Tm, Lu) show enrichment with respect to WOSw (Table 4; Fig. 5). The total average concentration of REEs in AOS is 118.88 ppm, which is lower than in WOSw (216.80 ppm), [21, 22], UCC (146.37 ppm) [12, 13, 16], and PAAS (183 ppm) [12]. The degree

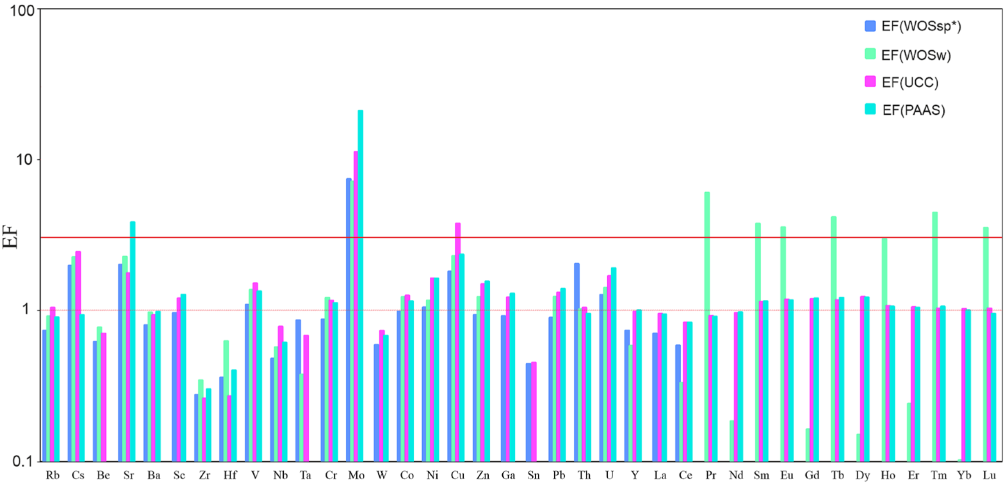

Fig. 5. Enrichment factors.

Table 4. Mean values of trace element concentrations in analysed oil shales (AOS), World Oil Shales (WOS), Upper Continental Crust (UCC), Post-Archaean Australian Shale (PAAS) and argillaceous rocks (K1i), enrichment factors (EFs), and degree of enrichment (Qi); range of concentrations in oil shale ashes from Jordan (JOSa)

TEs	AOS	WOSsp	WOSw	UCC	PAAS	K1i	EF(WOSsp*)	EF(WOSw)	EF(UCC)	EF(PAAS)	*Qi*	JOSa
Rb	102.11	139.1	140	112	160	130	0.73	0.91	1.04	0.90	0.79	-
Cs	9.88	5	5.5	4.60	15	2	1.98	2.25	2.44	0.93	4.94	-
Be	1.85	3	3	3	-	3	0.62	0.77	0.70	/	0.62	0.06–0.43
Sr	542.50	270	300	350	200	450	2.01	2.26	1.76	3.84	1.21	-
Ba	447.86	560	580	550	650	800	0.80	0.97	0.93	0.98	0.56	-
Sc	14.33	15	13	13.60	16	10	0.96	/	1.20	1.27	1.43	0.28–2.6
Zr	43.97	160	160	190	210	200	0.27	0.34	0.26	0.30	0.22	-
Hf	1.40	3.9	2.8	5.80	5	3	0.36	0.63	0.27	0.40	0.47	-
V	141.81	130	130	107	150	130	1.09	1.36	1.51	1.34	1.09	35.45–16178
Nb	8.21	17.2	18	12	19	11	0.48	0.57	0.78	0.61	0.75	-
Ta	0.60	0.7	2	1	-	-	0.86	0.38	0.68	/	/	-
Cr	87.14	100	90	85	110	100	0.87	1.21	1.16	1.12	0.87	10.90–163.76
Mo	14.84	2	2.6	1.50	1	2	7.42	7.14	11.24	21.01	7.42	-
W	1.29	2.2	1.8	2	2.70	1.8	0.59	/	0.73	0.68	0.72	-
Co	18.63	19	19	17	23	19	0.98	1.23	1.25	1.15	0.98	0.23–1.52
Ni	63.21	60.5	68	44	55	95	1.04	1.16	1.63	1.63	0.67	7.20–73.05
Cu	82.48	45.6	45	25	50	57	1.81	2.29	3.75	2.34	1.45	3.30–28.09
Zn	93.13	100	95	71	85	80	0.93	1.23	1.49	1.55	1.16	-
Ga	18.19	20	19	17	20	20	0.91	/	1.22	1.29	0.91	-

Continued on the next page

Table 4. *Continued*

TEs	AOS	WOSsp	WOSw	UCC	PAAS	K1i	EF(WOSsp*)	EF(WOSw)	EF(UCC)	EF(PAAS)	*Qi*	JOSa
Sn	2.18	5	6	5.5	-	10	0.44	/	0.45	/	0.22	-
Pb	19.65	22	20	17	20	20	0.89	1.23	1.31	1.39	0.98	-
Th	9.76	4.8	12	10.70	14.60	12	2.03	1.02	1.04	0.95	0.81	-
U	4.17	3.3	3.7	2.80	3.10	3.7	1.26	1.41	1.69	1.90	1.13	-
Y	19.07	26	41	22	27	26	0.73	0.58	0.98	1.00	0.73	1.8–39.7
La	25.12	36	40	30	38	90	0.70	0.00	0.95	0.94	0.28	1.55–27.4
Ce	46.79	80	95	64	80	50	0.58	0.33	0.83	0.83	0.94	1.8–15.7
Pr	5.75	-	9.7	7.10	8.90	7.1	/	6.03	0.92	0.91	0.81	0.3–3.8
Nd	21.90	-	39	26	32	26	/	0.18	0.96	0.97	0.84	1.26–40.3
Sm	4.53	-	7.3	4.50	5.60	4.5	/	3.75	1.14	1.15	1.01	0.25–4.1
Eu	0.91	-	1.6	0.88	1.10	0.95	/	3.54	1.18	1.17	0.96	0.15–0.6
Gd	3.98	-	7	3.80	4.70	3.8	/	0.16	1.19	1.20	1.05	0.26–2.9
Tb	0.66	-	1.2	0.64	0.77	-	/	4.15	1.17	1.21	/	0.04–0.6
Dy	3.80	-	5.5	3.50	4.40	-	/	0.15	1.23	1.22	/	0.12–2.0
Ho	0.75	-	1.6	0.80	1.00	-	/	2.97	1.07	1.06	/	0.05–0.6
Er	2.13	-	3.9	2.30	2.90	-	/	0.24	1.05	1.04	/	0.14–2.2
Tm	0.30	-	0.6	0.33	0.40	-	/	4.44	1.03	1.06	/	0.02–2.6
Yb	1.97	-	3.7	2.20	2.80	2.2	/	0.10	1.02	1.00	0.89	0.12–2.7
Lu	0.29	-	0.7	0.32	0.43	-	/	3.52	1.03	0.95	/	0.02–0.6
∑REEs	118.88	-	216.8	146.37	183	-	/	/	/	/	/	8.72–148.31

- – not determined; / – cannot be calculated; the enrichment factors EF(WOSw), EF(UCC) and EF(PAAS) were calculated using the content of aluminium (Section 2.3), since for these sediments Al content (16.7%, 15.17%, 18.90%, respectively) was available, whereas for EF(WOSsp*) it was not available.

of enrichment for the investigated TEs was also determined based on Qi values (Table 4). Results suggest that the analysed oil shales are noticeably enriched in Mo and Cs and belong to the fifth group according to the classification proposed by Shpirt and Punanova [25]. Furthermore, they are enriched to a certain extent with Cu, U, and Sc, belonging to the third group, while analysed samples are noticeably depleted in Ba, Zr, Hf, Sn, La, and Yb and belong to the first group. The remaining TEs are in the second group, which indicates that the examined oil shales and argillaceous rocks differ slightly in the concentrations of these TEs.

Comparing the range of concentrations in oil shale ash from different deposits in Jordan with values in the analysed samples, it is notable that most elements fall within the range, while the following elements show higher concentrations in the analysed samples: Be, Sc, Co, Cu, Ce, Pr, Sm, Eu, Gd, Tb, Dy, and Ho [46].

4. Conclusions

The detailed inorganic geochemical characterisation of the Upper layer of Aleksinac oil shale in the Dubrava block was performed. The cluster analysis of major, trace, and rare earth elements, total organic carbon, and total sulphur showed that the analysed samples are divided into two main clusters, indicating certain changes in the depositional environment during the formation of these sediments.

Correlation analysis clearly showed that TEs and REEs are associated with SiO_2, Al_2O_3, K_2O, and TiO_2, clastic minerals, clay, and feldspar, as well as zeolite minerals natrolite and analcime, indicating that TEs and REEs were brought into the basin mainly by clastic material. Taking into account both the enrichment factors (calculated in relation to World Oil Shales, Upper Continental Crust, and Post-Archaean Australian Shale) and the degree of enrichment (concerning argillaceous rocks), it can be concluded that the Aleksinac oil shale is slightly enriched only in Cu, Cs, Sr, V, Ni, Zn, Pb, and U, whereas more significant enrichment is observed for Mo exclusively. The mentioned elements, except Cs, Sr, and Pb, are redox-sensitive, and therefore their enrichment is in accordance with the OM-richness of the studied samples.

Compared with ‘standard values’, there is no significant enrichment of elements potentially toxic to the environment and health in the analysed sediments, except for Mo and Cu. Therefore, there is a low risk of trace element pollution if the Aleksinac oil shale were to be further exploited.

Data availability statement

The data supporting the findings of this study are available within the article.

Acknowledgements

The study was financed by the Ministry of Education, Science and Technological Development of the Republic of Serbia (contract No. 451-03-136/2025-03/200168, project No. 451-03-136/2025-03/200026). We dedicate this paper to the memory of our colleague, Prof. Dr Aleksandar Kostić, who passed away during the preparation of this manuscript. The publication costs of this article were partially covered by the Estonian Academy of Sciences.

References

1. Tissot, B. P., Welte, D. H. *Petroleum Formation and Occurrence*. 2nd ed. Springer-Verlag, Heidelberg, 1984.
2. Dyni, J. R. *Geology and Resources of Some World Oil Shale Deposits*. U.S. Geological Survey Scientific Investigations Report 2005–5295, Reston, 2006.
3. Ercegovac, M. *Geologija uljnih škriljaca (Geology of Oil Shales)*. Građevinska knjiga, Beograd, 1990.
4. Ercegovac, M., Grgurović, D., Bajc, S., Vitorović, D. Oil shale in Serbia: geological and chemical-technological investigations, actual problems of exploration and feasibility studies. In *Mineral Material Complex of Serbia and Montenegro at the Crossings of Two Millenniums* (Vujić, S., ed.). Margo-Art, Belgrade, 2003, 368–378.
5. Song, D. Y., Ma, Y. J., Qin, Y., Wang, W. F., Zheng, C. G. Volatility and mobility of some trace elements in coal from Shizuishan Power Plant. *Journal of Fuel Chemistry and Technology*, 2011, **39**(5), 328–332. https://doi.org/10.1016/S1872-5813(11)60024-8
6. Fu, X., Wang, J., Zeng, Y., Tan, F., Feng, X. Concentration and mode of occurrence of trace elements in marine oil shale from the Bilong Co area, northern Tibet, China. *International Journal of Coal Geology*, 2011, **85**(1), 112–122. https://doi.org/10.1016/J.COAL.2010.10.004
7. Fu, X., Wang, J., Zeng, Y., Tan, F., Feng, X. Trace elements and their behaviour during the combustion of marine oil shale from Changliang Mountain, northern Tibet, China. *Environmental Earth Sciences*, 2012, **70**, 1125–1134. https://doi.org/10.1007/s12665-012-2199-5
8. Vallner, L., Gavrilova, O., Vilu, R. Environmental risks and problems of the optimal management of an oil shale semi-coke and ash landfill in Kohtla-Järve, Estonia. *Science of The Total Environment*, 2015, **524–525**, 400–415. https://doi.org/10.1016/j.scitotenv.2015.03.130
9. Han, Y. W, Ma, Z. D., Zhang, H. F., Zhang, B. R., Li, F. L., Gao, S. et al. *Geochemistry*. Geological Publishing House, Beijing, 2003.
10. Gluskoter, H. J., Ruch, R. R., Miller, W. G., Cahill, R. A., Dreher, G. B., Kuhn, J. K. *Trace Elements in Coal: Occurrence and Distribution*. Illinois State Geological Survey, Circular 499, Urbana, 1977.

11. Fu, X., Wang, J., Tan, F., Feng, X., Zeng, S. The geochemistry of trace elements in marine oil shales and their combustion residues: occurrence and environmental aspects. *Energy Sources A: Recovery Utilization, and Environmental Effects*, 2016b, **38**(3), 410–419. https://doi.org/10.1080/15567036.2013.769036
12. Taylor, S. R., McLennan, S. M. *The Continental Crust: Its Composition and Evolution*. Blackwell Scientific, Oxford, 1985.
13. Taylor, S. R., McLennan, S. M. The geochemical evolution of the continental crust. *Reviews of Geophysics*, 1995, **33**(2), 241–265. https://doi.org/10.1029/95RG00262
14. Patterson, J. H., Ramsden, A. R., Dale, L. S., Fardy, J. J. Geochemistry and mineralogical residences of trace elements in oil shales from Julia Creek, Queensland, Australia. *Chemical Geology*, 1986, **55**(1–2), 1–16. https://doi.org/10.1016/0009-2541(86)90123-3
15. Gao, S., Luo, T.-C., Zhang, B.-R., Zhang, H.-F., Han, Y.-W., Hu, Y.-K. et al. Chemical composition of the continental crust as revealed by studies in East China. *Geochimica et Cosmochimica Acta*, 1998, **62**(11), 1959–1975. https://doi.org/10.1016/S0016-7037(98)00121-5
16. McLennan, S. M. Relationships between the trace element composition of sedimentary rocks and upper continental crust. *Geochemistry, Geophysics, Geosystems*, 2001, **2**(4), 2000GC00010. https://doi.org/10.1029/2000GC000109
17. Rudnick, R., Gao, S. Composition of the Continental Crust. In *Treatise on Geochemistry 3* (Holland, H. D, Turekian, K. K., eds). Elsevier-Pergamon, Oxford, 2003, 1–64.
18. Haskin, L. A., Wildeman, T. R., Haskin, M. A. An accurate procedure for the determination of the rare earths by neutron activation. *Journal of Radioanalytical and Nuclear Chemistry*, 1968, **1**, 337–348. https://doi.org/10.1007/BF02513689
19. Boynton, W. V. Cosmochemistry of the rare earth elements: meteorite studies. In *Rare Earth Element Geochemistry* (Henderson, P., ed.). Elsevier, New York, 1984, 63–114.
20. Gromet, L. P., Haskin, L. A., Korotev, R. L., Dymek, R. F. The "North American shale composite": its compilation, major and trace element characteristics. *Geochimica et Cosmochimica Acta*, 1984, **48**(12), 2469–2482. https://doi.org/10.1016/0016-7037(84)90298-9
21. Wedepohl, K. H. Environmental influences on the chemical composition of shales and clays. *Physics and Chemistry of the Earth*, 1971, **8**, 307–331. https://doi.org/10.1016/0079-1946(71)90020-6
22. Wedepohl, K. H. The composition of the upper Earth's crust and the natural cycles of selected elements. Metals in natural raw materials. Natural resources. In *Metals and Their Compounds in the Environment* (Merian, E., ed.). VCH, Weinheim, 1991, 3–17.
23. Heinrichs, H., Schulz-Dobrick, B., Wedepohl, K. H. Terrestrial geochemistry of Cd, Bi, Tl, Pb, Zn and Rb. *Geochimica et Cosmochimica Acta*, 1980, **44**(10), 1519–1533. https://doi.org/10.1016/0016-7037(80)90116-7
24. Brumsack, H.-J. The trace metal content of recent organic carbon-rich

sediments: implications for Cretaceous black shale formation. *Palaeogeography, Palaeoclimatology, Palaeoecology*, 2006, **232**(2–4), 344–361. https://doi.org/10.1016/j.palaeo.2005.05.011

25. Shpirt, M. Y., Punanova, S. A. Comparative assessment of the trace-element composition of coals, crude oils, and oil shales. *Solid Fuel Chemistry*, 2007, **41**, 267–279. https://doi.org/10.3103/S0361521907050023
26. Ross, D. J. K., Bustin, R. M. Investigating the use of sedimentary geochemical proxies for paleoenvironment interpretation of thermally mature organic-rich strata: examples from the Devonian–Mississippian shales, Western Canadian Sedimentary Basin. *Chemical Geology*, 2009, **260**(1–2), 1–19. https://doi.org/10.1016/j.chemgeo.2008.10.027
27. Jelenković, R., Kostić, A., Životić, D., Ercegovac, M. Mineral resources of Serbia. *Geologica Carpathica*, 2008, **59**(4), 345–361.
28. Obradović, J., Djurdjević-Colson, J., Vasić, N. Phytogenic lacustrine sedimentation – oil shales in Neogene from Serbia, Yugoslavia. *Journal of Paleolimnology*, 1997, **18**, 351–364. https://doi.org/10.1023/A:1007907109399
29. Obradović, J., Vasić, N. *Jezerski baseni u neogenu Srbije (Neogene Lacustrine Basins from Serbia)*. Srpska akademija nauka i umetnosti, Beograd, 2007.
30. Marović, M. Neotektonski sklop Aleksinačkog Pomoravlja (Neotectonic complex of Aleksinac Pomoravlje). *Geološki Anali Balkanskoga Poluostrva*, 1988, **51**, 215–219.
31. Ercegovac, M., Vitorović, D., Kostić, A., Životić, D., Jovančićević, B. Geology and Geochemistry of the "Aleksinac" oil shale deposit (Serbia). In *Joint 61st ICCP/26th TSOP Meeting, Advances in Organic Petrology and Organic Geochemistry*, 19–26 September 2009, Gramado, Brazil, 13.
32. Gajica, G., Šajnović, A., Stojanović, K., Antonijević, M., Aleksić, N., Jovančićević, B. The influence of pyrolysis type on shale oil generation and its composition (Upper layer of Aleksinac oil shale, Serbia). *Journal of the Serbian Chemical Society*, 2017b, **82**(12), 1461–1477. https://doi.org/10.2298/JSC170421064G
33. Gajica, G., Šajnović, A., Stojanović, K., Kostić, A., Slipper, I., Antonijević, M. et al. Organic geochemical study of the Upper layer of Aleksinac oil shale in the Dubrava block, Serbia. *Oil Shale*, 2017, **34**(3), 197–218. https://doi.org/10.3176/oil.2017.3.01
34. Tribovillard, N., Algeo, T. J., Lyons, T., Riboulleau, A. Trace metals as paleoredox and paleoproductivity proxies: an update. *Chemical Geology*, 2006, **232**(1–2), 12–32. https://doi.org/10.1016/j.chemgeo.2006.02.012
35. Ferriday, T., Montenari, M. Chemostratigraphy and chemofacies of source rock analogues: a high-resolution analysis of black shale successions from the lower Silurian Formigoso Formation (Cantabrian Mountains, NW Spain). In *Stratigraphy & Timescales* (Montenari, M., ed.). Elsevier Science, Amsterdam, 2016, 123–255.
36. Mukhopadhyay, P. K., Goodarzi, F., Crandlemire, A. L., Gillis, K. S., MacNeil, D. J., Smith, W. D. Comparison of coal composition and elemental

distribution in selected seams of the Sydney and Stellarton Basins, Nova Scotia, Eastern Canada. *International Journal of Coal Geology*, 1998, **37**(1–2), 113–141. https://doi.org/10.1016/S0166-5162(98)00020-2

37. Fu, X., Wang, J., Zeng, Y., Tan, F., Feng, X. REE geochemistry of marine oil shale from the Changshe Mountain area, northern Tibet, China. *International Journal of Coal Geology*, 2010, **81**(3), 191–199. https://doi.org/10.1016/j.coal.2009.12.006
38. Tao, S., Xu, Y., Tang, D., Xu, H., Li, S., Chen, S. et al. Geochemistry of the Shitoumei oil shale in the Santanghu Basin, Northwest China: implications for paleoclimate conditions, weathering, provenance and tectonic setting. *International Journal of Coal Geology*, 2017, **184**, 42–56. https://doi.org/10.1016/j.coal.2017.11.007
39. Wang, Z., Fu, X., Feng, X., Song, C., Wang, D., Chen, W. et al. Geochemical features of the black shales from the Wuyu Basin, southern Tibet: implications for palaeoenvironment and palaeoclimate. *Geological Journal*, 2017, **52**(2), 282–297. https://doi.org/10.1002/gj.2756
40. Zhao, M., Liu, Y., Jiao, X., Zhou, D., Meng, Z., Yang, Y. Major, trace and rare earth element geochemistry of the Permian Lucaogou oil shales, eastern Junggar Basin, NW China: implications for weathering, provenance and tectonic setting. *Australian Journal of Earth Sciences*, 2023, **70**(4), 585–602. https://doi.org/10.1080/08120099.2023.2186951
41. Wu, C., Tuo, J., Zhang, M., Liu, Y., Xing, L., Gong, J. et al. Multiple controlling factors of lower Palaeozoic organic-rich marine shales in the Sichuan Basin, China: evidence from minerals and trace elements. *Energy Exploration & Exploitation*, 2017, **35**(5), 627–644. https://doi.org/10.1177/0144598717709667
42. Liang, Y., Zhang, J., Liu, Y., Tang, X., Li, Z., Ding, J. et al. Evidence for biogenic silica occurrence in the Lower Silurian Longmaxi shale in southeastern Chongqing, China. *Minerals*, 2020, **10**(11), 945. https://doi.org/10.3390/min10110945
43. Pipe, A. B., Leybourne, M. I., Johannesson, K. H., Hannigan, R. E., Layton-Matthews, D. Trace and rare earth element geochemistry of black shales from the Upper Ordovician Utica Shale magnafacies. *Chemical Geology*, 2025, **672**, 122507. https://doi.org/10.1016/j.chemgeo.2024.122507
44. Dar, S. A., Khan, K. F., Birch, W. D. Sedimentary: phosphates. In *Reference Module in Earth Systems and Environmental Sciences* (Elias, S. A., ed.). Elsevier, 2017.
45. Wall, F. Rare earth elements. In *Encyclopedia of Geology, 2nd ed.* (Alderton, D., Elias, S. A., eds). Academic Press, London, 2021, 680–693.
46. Al-Ayed, O. S., Qawaqneh, M. K., Abu-Nameh, E. S. M. Tracing rare earth elements in oil shale ash. *Oil Shale*, 2024, **41**(2), 132–143. https://doi.org/10.3176/oil.2024.2.04
47. Algeo, T. J., Tribovillard, N. Environmental analysis of paleoceanographic systems based on molybdenum–uranium covariation. *Chemical Geology*, 2009, **268**(3–4), 211–225. https://doi.org/10.1016/j.chemgeo.2009.09.001

Oil Shale, 2026, 43, 1, 75–103 https://doi.org/10.3176/oil.2026.1.04

Genesis and depositional environment of organic-rich sediments in the Neogene organic-rich sediments from the Aleksinac deposit (Serbia): Part B

Gordana Gajica(a)*, Aleksandra Šajnović(a), Ksenija Stojanović(b), Milan D. Antonijević(c), Aleksandar Kostić(d), Branimir Jovančićević(b)

(a) Center of Chemistry – Institute of Chemistry, Technology and Metallurgy, University of Belgrade, Njegoševa 12, 11000 Belgrade, Serbia
(b) Faculty of Chemistry, University of Belgrade, Studentski trg 12-16, 11000 Belgrade, Serbia
(c) School of Chemistry and Chemical Engineering, University of Surrey, Guildford, Surrey GU2 7XH, United Kingdom
(d) Faculty of Mining and Geology, University of Belgrade, Đušina 7, 11000 Belgrade, Serbia

Received 30 April 2025, accepted 23 January 2026, available online 29 January 2026

Abstract. *To determine the characteristics of the palaeoenvironment that affected organic richness, the Neogene organic-rich sediments in the Upper layer of the Aleksinac deposit (Dubrava block, Serbia) were examined. The studied samples are presumed to be of andesitic to felsic origin, with evidence of volcanic activity. Sediment generation was influenced by hydrothermal fluids, which promoted the productivity of aquatic organisms and led to organic enrichment. Clastic input brought trace and rare earth elements into the basin. Palaeoenvironmental indicators derived from concentrations of major, trace, and rare earth elements show good accordance with organic geochemical data obtained in previous detailed studies, indicating deposition of the sediments in an anoxic lacustrine environment of variable salinity under warm, arid, and semiarid/semihumid climatic conditions. Such settings favoured primary bioproductivity in the lake, whereas a stable, stratified water column with highly reducing bottom water enhanced organic matter preservation. The lowering of total organic carbon content was mainly controlled by more humid episodes that promoted clastic influx and decreased organic matter concentration, rather than by changes in anoxic redox conditions.*

Keywords**:** *organic-rich sediments, inorganic proxies, palaeoenvironment.*

---

* Corresponding author, gordana.gajica@ihtm.bg.ac.rs

1. Introduction

Oil shale is mostly composed of inorganic matter, with organic matter (OM) dispersed within it, forming a homogeneous mixture. It is often characterised by fine lamination that alternates between laminae of mixed organic and mineral materials and pure mineral material. Although OM is present in a seemingly small percentage, it is very important, since it mainly contains kerogen types I and II, which have great potential to produce liquid hydrocarbons under suitable geological conditions or through thermal processing [1]. Low concentrations of trace and rare earth elements (TEs and REEs, respectively) can be found in oil shale. These elements do not exist independently and may be present as organometallic compounds, embedded in mineral crystal structures, or in a dispersed state on clay and oxyhydroxide particles [2]. Their distributions are mainly influenced by the geochemical cycle of elements and controlled by the physical and chemical characteristics of their atoms or ions, as well as by biotic and abiotic factors in the depositional environment [3, 4].

The analysis of the inorganic matter in oil shale can be used to reconstruct the geological history of the study area based on the content and distribution of elements, as well as corresponding geochemical parameters. This, in turn, allows us to determine the source material and palaeoconditions in the depositional environment that contributed to OM supply, its preservation, and the formation of organic-rich sediments, such as oil shales [1]. The main factors that control OM enrichment are palaeobioproductivity, conditions in the palaeoenvironment (climate, salinity, and redox potential), and the influx of clastic material [5–12].

Although the Aleksinac oil shale deposit is the largest and richest oil shale deposit in Serbia and of economic significance [13, 14], there are only a few studies on its inorganic composition. Therefore, the aims of this study were: (i) to establish comprehensive characteristics of the palaeoenvironment that affected the organic richness of the sediments based on inorganic proxies, and (ii) to examine the compatibility between inorganic and organic geochemical parameters. The results of this study may serve as a valuable archive of palaeoenvironmental information on the area and can be transposed to other geological scenarios.

2. Samples and analytical methods

2.1. Samples

Outcrop samples from the Upper layer of the Dubrava block of the Aleksinac deposit were selected for this study. In previous publications, a detailed description of the lithostratigraphic column of the analysed samples has been provided [15, 16], as well as in Part A of this study (see this issue).

2.2. Previous results

The origin, depositional environment, maturity and hydrocarbon generation potential of the organic matter, derived from the comprehensive OM characterisation of the analysed samples, are detailed in prior studies [15–17]. To have a better understanding of the depositional environment, these results are utilised to correlate with inorganic geochemical parameters but are not presented in this work. In this section, the main findings obtained previously are summarised, as they will be used to correlate with inorganic parameters.

The OM is uniformly immature, with total organic carbon (TOC) content varying between 1.31 and 29.10 wt% (corresponding to vitrinite reflectance of 0.36–0.44% and a production index of 0.01–0.02). Sample D16 has the highest OM content, whereas samples D4, D6, and D7 have the lowest. According to Rock-Eval data, the OM mainly consists of a mixture of kerogen types I and II. The samples that stand out are sample D13, which contains exclusively kerogen type I, and samples D4, D6, and D7, which contain kerogen type II with a certain input of kerogen type III.

The biomarker patterns are in accordance with the Rock-Eval data, revealing a significant presence of aquatic organisms, including green and brown algae, as well as bacteria, with a moderate influence from higher-plant organic matter [16, 17]. Based on the thermal decomposition of kerogen, all samples show a high potential for oil generation. Only samples D4, D6, and D7 have a slightly lower potential, which agrees with the type of kerogen in these samples [15–17].

The OM was deposited in a reducing lacustrine environment characterised by alkaline, brackish to freshwater conditions and water-column stratification, most likely as a result of variations in water depth, salinity, and temperature during the formation of the analysed sediments [16]. According to biomarker patterns in the samples under investigation, sample D16 differs most from the others [16, 17]. A shallow water column may have contributed to the relative abundance of C_{29} hopane in sample D16, whereas a steranes/hopanes ratio < 1 suggests a higher presence of prokaryotic OM than algal.

2.3. Analytical methods

For the determination of major elements, inductively coupled plasma optical emission spectroscopy (ICP-OES, Thermo iCAP 6500) was used, whereas for TEs and REEs, inductively coupled plasma mass spectrometry (ICP-MS, Thermo X Series II ICP-MS) was applied. The mineral composition was analysed using an XRD analyser (Bruker D8 Advance diffractometer). A Rock-Eval 6 Standard analyser was employed for the determination of TOC, and an elemental analyser (Vario EL III, CHNOS Elemental Analyser, Elementar Analysensysteme GmbH) for total sulphur (TS) content. Detailed analytical procedures are given in Part A of this study.

3. Results and discussion

3.1. Genesis and depositional environment of organic-rich sediments

Many geochemical parameters (Table 1) were used to determine sediment provenance, tectonic settings, the influx of hydrothermal fluids, palaeobioproductivity, clastic influx, palaeoconditions in the water column (redox potential, salinity), and climatic conditions, in order to get a better insight into the depositional environment and the genesis of organic-rich sediments of the Aleksinac deposit. The element concentrations on which the parameters were calculated are given in Part A of this study (section 3.1).

3.1.1. Sediment provenance

It is well known that the nature of the parent rocks influences the composition of sedimentary rocks [18–21]. The Al/Ti ratio and the Al vs Ti diagram are used to determine the provenance of sedimentary rocks because Al and Ti have low solubility in water. Therefore, their ratio is relatively close to that of the source rocks [20, 22–24]. Most samples have Al/Ti ratio values around 20, i.e. within the range of 8–21, which indicates intermediate igneous rock sources (Table 1) [20]. A few samples (D1, D4, D11) have values slightly higher than 21, signifying an origin from felsic igneous rocks. However, all of them are plotted near the boundary line between intermediate and felsic rocks, except for sample D16 (Al/Ti = 34; Table 1), which relates to a felsic source (Fig. 1a) [20].

The Ti vs Zr, Th/Sc vs Zr/Sc, and Co/Th vs La/Sc diagrams are also used to determine sediment provenance, since La, Th, Co, and Sc are immobile elements whose distribution is less affected by the heavy-mineral fraction than TEs such as Zr, and they are only weakly influenced by diagenesis and metamorphism [18, 24, 28]. Furthermore, La and Th are more concentrated in felsic rocks, whereas Sc and Co are more abundant in mafic rocks [26, 29]. In the Ti vs Zr diagram (Fig. 1b), all samples are located in the area of intermediate igneous rocks; only sample D16 is at the border between intermediate and felsic igneous rocks. In the Th/Sc vs Zr/Sc diagram (Fig. 1c) [18], all analysed samples are plotted in the area of felsic source rocks and have not experienced sedimentary recycling. Consistent with the results from Figure 1c, the Co/Th vs La/Sc diagram (Fig. 1d) suggests that most of the analysed samples correspond to a source between andesite and felsic volcanic rocks. According to this diagram, samples D11, D14, and D16 are more closely related to andesites and can be distinguished from the others.

A volcanic origin is not surprising, since volcanic activity in the area of the Aleksinac deposit during the Miocene has been proven, and volcanic material was transported into the lake in smaller amounts but over a longer period [30, 31]. Further evidence of volcanic activity is the presence of zeolite-group minerals – analcime and natrolite – in all samples except D16 (fig. 1 in Part A).

Table 1. Values of geochemical parameters

Parameter	D1	D2	D3	D4	D5	D6	D7	D8	D9	D10	D11	D12	D13	D14	D15	D16
Al/Ti	23.49	20.20	20.05	23.29	21.98	20.11	21.91	20.92	21.40	19.52	22.25	20.85	20.16	20.39	20.63	34.20
L/H	6.36	6.86	7.84	6.91	9.56	8.02	7.87	7.57	8.45	5.59	8.95	8.64	7.45	8.73	7.55	8.20
Ce/Ce*	0.87	0.87	0.90	0.93	0.91	0.98	0.88	0.89	0.86	0.91	0.92	0.89	0.85	0.86	0.88	0.84
Eu/Eu*	1.02	0.98	0.99	0.99	1.01	1.00	1.00	1.00	0.97	1.01	0.98	0.99	1.01	0.97	1.00	1.15
Ba/Ti	623.25	869.00	743.71	665.32	664.68	681.2	678.9	705.84	567.87	718.24	645.62	725.07	887.23	680.22	738.32	2266.07
Ba/Al	26.54	43.02	37.1	28.57	30.23	33.87	30.98	33.74	26.54	36.79	29.01	34.78	44	33.36	35.79	66.26
Ti/Al	0.04	0.05	0.05	0.04	0.05	0.05	0.05	0.05	0.05	0.05	0.04	0.05	0.05	0.05	0.05	0.03
Si/Al	2.41	3.52	2.75	2.49	3.10	2.51	2.62	2.94	2.83	2.67	2.92	2.93	3.45	2.99	2.85	3.46
∑MCE	64.86	43.63	53.62	66.45	60.20	66.72	66.71	55.14	66.04	51.73	58.95	51.78	40.79	55.67	48.58	24.10
∑TCE	152.18	102.11	140.00	185.02	120.79	204.93	180.67	156.89	134.04	142.76	111.62	131.14	100.98	118.25	127.02	55.73
∑CE	217.04	145.74	193.62	251.47	180.99	271.65	247.38	212.03	200.08	194.49	170.57	182.92	141.77	173.92	175.60	79.83
C-value	0.42	0.17	0.27	0.48	0.30	0.25	0.39	0.26	0.52	0.29	0.36	0.30	0.21	0.36	0.29	0.32
Rb/Sr	0.36	0.10	0.19	0.34	0.25	0.27	0.28	0.18	0.53	0.22	0.27	0.18	0.11	0.27	0.17	0.04
Sr/Cu	2.64	12.26	7.04	1.91	6.07	5.80	3.41	10.14	2.27	5.92	4.64	5.83	11.95	5.56	7.55	73.74
Sr/Ba	0.63	1.90	1.18	0.51	1.14	0.75	0.68	1.34	0.6	0.98	1.13	1.18	1.69	1.1	1.26	4.68
Ca/(Ca + Fe)	0.39	0.73	0.57	0.31	0.61	0.51	0.35	0.64	0.35	0.53	0.47	0.62	0.70	0.53	0.61	0.93
EF_{Mo}	42.93	3.67	8.30	14.13	9.70	5.39	14.88	3.92	8.28	4.80	20.23	6.30	17.28	9.71	9.25	1.12
EF_{U}	4.33	2.27	1.47	3.06	0.79	1.65	1.92	1.44	0.96	2.77	0.64	0.99	0.96	0.67	2.45	0.71
EF_{V}	1.66	1.04	1.54	2.30	1.37	1.24	1.94	1.43	1.99	1.53	1.58	1.42	1.10	1.85	1.51	0.58
EF_{Cu}	5.11	2.75	3.75	6.19	3.51	3.48	4.87	2.62	5.12	3.61	4.49	3.93	2.45	3.93	3.20	0.98
EF_{Ni}	1.32	0.71	1.18	0.86	1.09	0.93	1.25	1.00	1.30	1.03	1.40	1.21	0.92	1.27	1.04	9.61
EF_{Zn}	2.26	0.91	1.47	1.76	1.36	1.46	2.10	1.42	1.79	1.54	1.66	1.33	1.20	1.65	1.46	0.48
V/(V + Ni)	0.75	0.78	0.76	0.87	0.75	0.77	0.79	0.78	0.79	0.78	0.73	0.74	0.74	0.78	0.78	0.13
V/Zn	1.11	1.72	1.58	1.97	1.52	1.29	1.40	1.52	1.67	1.50	1.43	1.61	1.39	1.69	1.56	1.83

LREE/HREE = light REEs / heavy REEs; Ce anomaly, $Ce/Ce^* = Ce_N / (La_N + Pr_N)^{1/2}$ (subscript $_N$ represents PAAS-normalised values) [25]; Eu anomaly, $Eu/Eu^* = Eu_N / (Sm_N + Gd_N)^{1/2}$; ∑MCE – sum of major clastic elements = Al + Si + Ti; ∑TCE – sum of trace clastic elements = Zr + Hf + Nb + Th + Th + La + Ce; ∑CE – sum of clastic elements = ∑MCE + ∑TCE; C-value = (Fe + Mn + Cr + V + Ni + Co)/(Ca + Mg + K + Na + Sr + Ba); enrichment factors (EFs) are calculated in relation to UCC (see section 3.3 in Part A) [19, 26, 27].

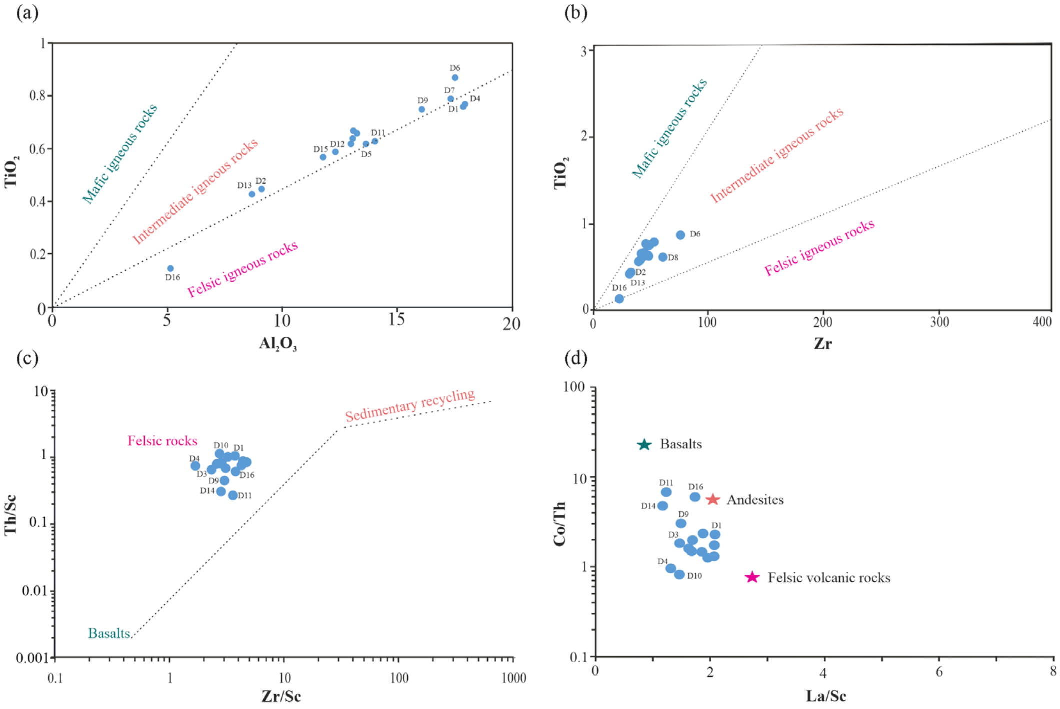

Fig. 1. Source discrimination diagrams: (a) TiO_2 vs Al_2O_3, (b) TiO_2 vs Zr, (c) Th/Sc vs Zr/Sc, and (d) Co/Th vs La/Sc.

According to Obradović and Vasić [31], analcime in the Aleksinac deposit formed through the alteration of volcanic glass, and it can also be formed by the decomposition and alteration of the earlier-phase zeolite mineral natrolite [32].

The REEs can also be used to determine sediment provenance owing to their chemical stability during different processes such as erosion, transportation, weathering, deposition, and diagenesis [18, 33, 34]. The analysed samples are characterised by high LREE/HREE ratios, which is typical of felsic rock provenance (Table 1; fig. 3 in Part A) [26, 28, 29, 35]. In oil shale, their main sources are terrigenous inherited minerals and authigenic components [36]. The statistically significant positive correlations of REEs with constituents of clastic minerals and negative correlations with carbonates (section 3.2 in Part A) indicate a terrigenous origin.

3.1.2. Tectonic settings

The plate tectonic settings of the sediment source area are important due to terrain-specific signatures and influence on the geochemical composition of deposited sedimentary rocks [23, 37–40]. Some elements are inactive during transportation and deposition, and therefore reflect different tectonic settings [39, 41].

The cross-plot K/Na vs Si (Fig. 2a) shows that most of the analysed samples were deposited in an active continental margin, while only samples D5, D6, and D9 correspond to a passive continental margin [40, 42]. Conversely, the ternary diagrams Ca–K–Na and La–Th–Sc [39] show that most of the analysed samples plot within the field of a continental island arc (Fig. 2b).

The results imply that the sediments developed in terrain with the characteristics of an active continental margin built on a continental island arc. The obtained data are not surprising, since the region of the Aleksinac deposit is known for its very complex tectonic settings, caused by the convergence of several oceanic and continental entities in the Tethyan realm between the African and European plates [43]. This resulted in the formation of four geotectonic units: the Dinarides, Carpatho-Balkanides, Serbian–Macedonian Massif, and Pannonian Basin [14, 43, 44]. According to Obradović and Vasić [31], the Aleksinac deposit was formed by the fragmentation of two geotectonic units, the Carpatho-Balkanides and the Serbian–Macedonian Massif.

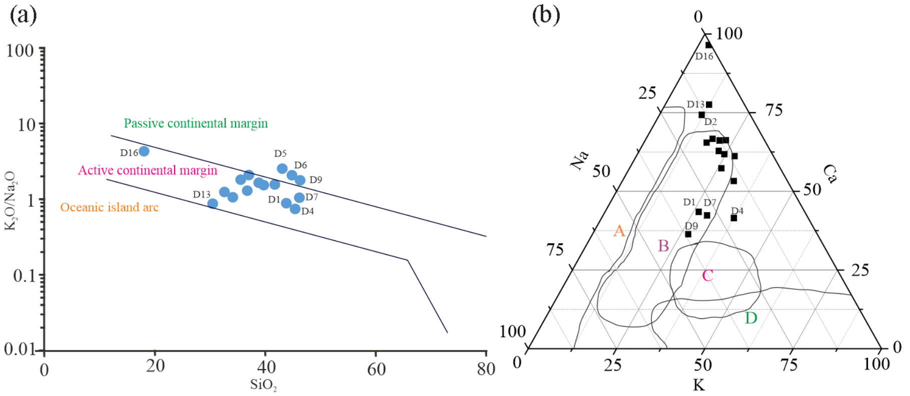

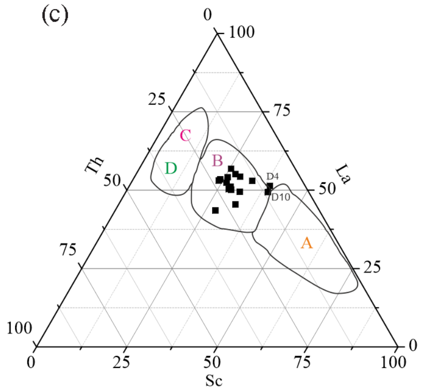

Fig. 2. Tectonic setting discrimination diagrams: (a) major elements K/Na vs Si, (b) Ca–Na–K, and (c) trace elements La–Th–Sc. Abbreviations: A – oceanic island arc; B – continental island arc; C – active continental margin; D – passive continental margin.

3.1.3. Hydrothermal fluids

Hydrothermal fluids mainly occur due to volcanic eruptions, lithification processes, and atmospheric deposition, causing the input of certain elements into deposits. They play a significant role in different geological processes. A large amount of minerals and nutrients can be transported into the lake by hydrothermal fluids, which usually promote the productivity of aquatic organisms and, consequently, may lead to OM enrichment in sediments [45, 46].

TEs (Zn, Ni, Cu) and REEs (La, Ce) can be enriched in hydrothermal fluids and, therefore, can be used to estimate whether the depositional environment was affected by hydrothermal fluids [47–49]. Furthermore, the Co/Zn vs Co + Cu + Ni (Fig. 3a) [50] and La vs Ce (Fig. 3b) [49] cross-plots, as well as the Ni–Co–Zn ternary diagram (Fig. 3c) [47, 51], were used for the estimation of hydrothermal influx.

The obtained results indicate that hydrothermal fluids influenced the analysed samples, whereas this influence was least pronounced, or absent, in sample D16 (Fig. 3). As noted previously, during the Lower Miocene there was noticeable volcanic activity (Section 3.1.1), thus the hydrothermal impact is not surprising. Additional evidence for hydrothermal fluids is provided by the presence of hydrothermal zeolite minerals, analcime and natrolite [52], identified in all samples except D16 (fig. 1 in Part A).

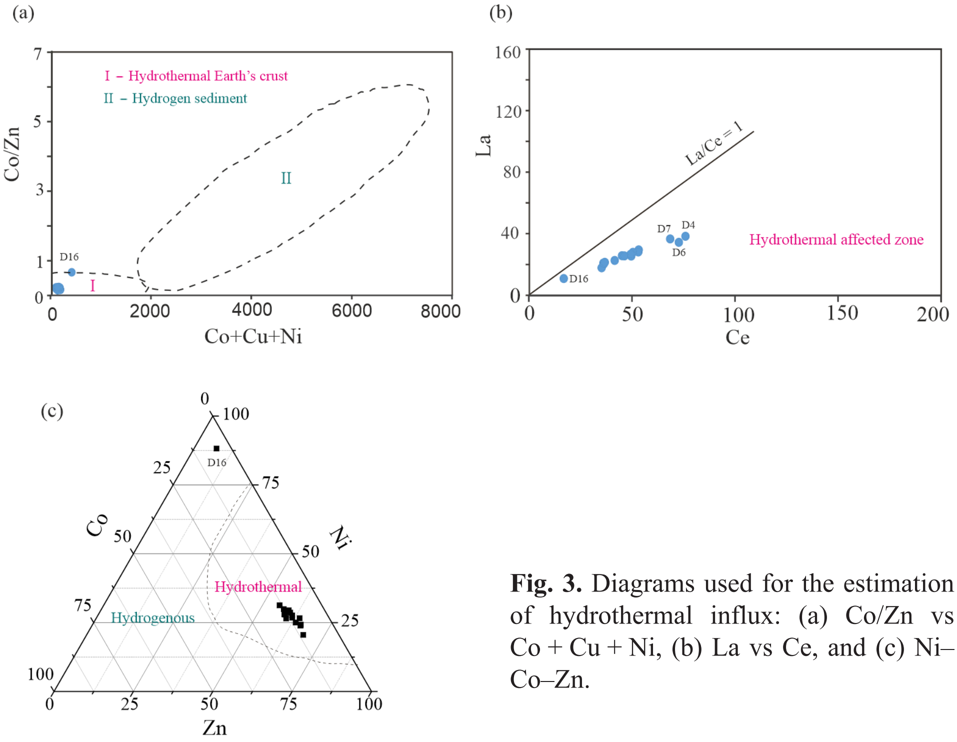

Fig. 3. Diagrams used for the estimation of hydrothermal influx: (a) Co/Zn vs Co + Cu + Ni, (b) La vs Ce, and (c) Ni–Co–Zn.

3.1.4. Palaeobioproductivity

The content of biogenic elements is associated with biological growth and can be used for the estimation of palaeobioproductivity, which is one of the main factors controlling OM content in sedimentary rocks [5, 48]. The Ba content is often used for the qualitative assessment of palaeobioproductivity, as the Ba cycle in sediments is controlled by OM content in the depositional environment [48, 53]. The Ba/Ti and Ba/Al ratios can be used to eliminate the dilution effect of OM and authigenic minerals in relation to the Ba concentration in terrigenous detrital matter [54].

The strong correlation between Ti and Al ($r = 0.97$, $p < 0.001$) in the analysed samples indicates that Al originates from terrigenous detrital matter and that biogenic processes did not affect Al concentration; thus, these ratios can be used [55]. The highest values of Ba/Ti and Ba/Al ratios are found in samples D13 and D16, which agrees with the greatest TOC content in these samples (Table 1; table 1 in Part A). Furthermore, Ba/Ti and Ba/Al ratios correlate well with TOC contents in samples D1–D15 ($r = 0.70$, $p < 0.01$; 0.68, $p < 0.01$, respectively; Fig. 4a).

The TOC content is controlled by primary bioproduction, along with redox conditions and the influx of terrigenous detrital matter into the water column. The diagram of the Cu/Mo ratio vs Cu can be used to distinguish whether the formation of organic-rich sediments resulted from increased bioproductivity or from reducing conditions [56, 57]. Specifically, high bioproductivity is usually associated with elevated Cu content, whereas Mo concentration has no impact [58]. Conversely, both Cu and Mo are enriched under anoxic conditions. Some enrichment of these elements is found in the analysed sediments (table 1 and fig. 5 in Part A). A weak statistically significant negative correlation between Cu/Mo and Cu ($r = 0.44$, $p = 0.10$; Fig. 4b) shows that, in addition to palaeobioproductivity (Fig. 4a), the enrichment of sediments in OM was also controlled by reducing conditions in the depositional environment. The same conclusion was derived from organic geochemical proxies, including the pristane/phytane ratio, gammacerane index, and abundance of β-carotane, as discussed in detail in earlier research [16].

Furthermore, the differences in TOC among D1–D15 samples can also result from varying influxes of clastic material. This is confirmed by the statistically significant positive correlation of TOC with the CaO/SiO_2 ratio ($r = 0.73$, $p < 0.01$; Fig. 4c) and will be discussed in more detail in the next section.

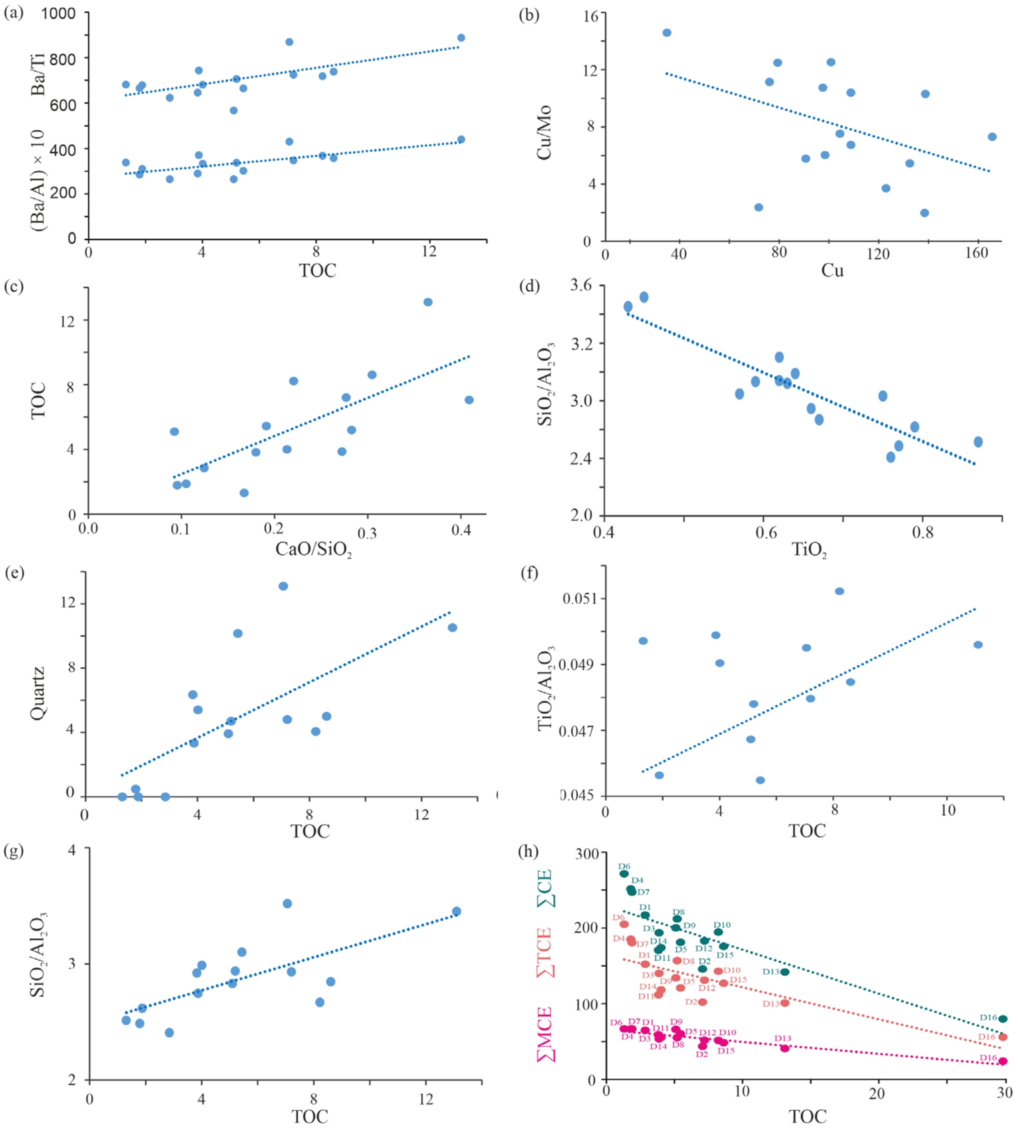

Fig. 4. Correlation diagrams between: (a) Ba/Ti and Ba/Al with TOC, (b) Cu/Mo and Cu, (c) TOC and CaO/SiO_2, (d) SiO_2/Al_2O_3 vs TiO_2, (e) quartz vs TOC, (f) TiO_2/Al_2O_3 vs TOC, g) SiO_2/Al_2O_3 vs TOC, (h) TOC and major clastic elements, trace clastic elements, and the sum of major and trace clastic elements. ∑MCE – sum of major clastic elements = (Ti + Al + Si); ∑TCE – sum of trace elements = (Zr + Th + Nb + Hf + La + Ce); ∑CE – sum of clastic elements = ∑MCE + ∑TCE.

3.1.5. Influx of clastic material

The clastic influx can induce both OM preservation (through a faster sedimentation rate, which reduces the intensity of OM degradation by aerobic microbial communities in the water column) and the dilution of OM concentration (through increased input of clastic material). In addition, clastic influx affects the type of both mineral and organic matter in the oil shale [24]. Furthermore, a greater input of clastic material increases nutrient supply, which can cause blooms of aquatic organisms and facilitate OM enrichment [9]. Concentrations of major clastic elements (MCEs; Ti, Al, and Si) and trace clastic elements (TCEs; Zr, Th, Nb, Hf, La, and Ce) are used as proxies for clastic influx [59, 60], since they are chemically stable during transportation, weathering, and diagenesis [61].

The Ti/Al ratio is used because Ti and Al mainly occur in clastic minerals of terrigenous origin, with Al representing aluminosilicate minerals and Ti occurring in clay and heavy minerals [6, 41, 62, 63]. Statistically significant positive correlations of Al with Ti, K, and Na ($r = 0.97$, $p = 2.3 \times 10^{-9}$; $r = 0.86$, $p < 0.01$; $r = 0.75$, $p < 0.01$, respectively; Fig. 1a) indicates that these elements are associated with clastic material [64], while the correlation between Ti and Al implies that the clastic influx was probably derived from a constant source (Section 3.1.4) [65, 66]. The Ti/Al ratio values in all samples are relatively uniform (0.04–0.05), with only sample D16 slightly lower (Ti/Al = 0.03; Table 1). Additionally, similar REE distributions (fig. 3 in Part A) show a consistent source during sediment formation, closely connected with terrigenous clastic rocks, implying a stable terrestrial material supply [33].

The Si/Al ratio is used as a clastic influx proxy, representing the presence of quartz in relation to clay minerals, because Si has both clastic and biogenic origins, while Al is exclusively terrigenous [62, 67]. The values of this parameter range between 2.41–3.52. Samples D1, D4, and D6 have the lowest values, whereas samples D16, D13, and D2 have the highest (Table 1). Furthermore, a statistically significant negative correlation between Ti and the Si/Al ratio ($r = 0.90$, $p < 0.01$; Fig. 4d) indicates that a certain amount of silica originates from non-detrital input [68, 69]. Moreover, a moderate positive correlation between quartz content and TOC ($r = 0.68$, $p < 0.01$; Fig. 4e) can be indicative of a partly biogenic origin of silica from siliceous organisms (e.g. SiO_2-rich plankton) [70, 71], suggesting that OM and part of the silica were deposited and buried together [69].

The obtained Ti/Al results indicate that the detrital influx was relatively constant and, therefore, could not have been a critical factor controlling variations in OM enrichment among the studied samples ($r = 0.51$, $p = 0.05$; Fig. 4f). Conversely, the Si/Al ratio values suggest certain differences among samples D1–D15 and show a stronger correlation with TOC ($r = 0.70$, $p < 0.01$; Fig. 4g). Therefore, clastic influx could have been a significant factor influencing the formation of these organic-rich sediments. This is more evident when concentrations of clastic mineral constituents are used as proxies for clastic influx (Fig. 4h). In Figure 4h, the strong negative correlations of TOC with MCEs and TCEs ($r \sum MCE = 0.86$, $p < 0.01$; $r \sum TCE = 0.70$, $p < 0.01$; $r \sum CE = 0.77$, $p < 0.01$) clearly indicate that clastic influx resulted in a decrease of OM concentration in the studied samples. Furthermore, the trend of samples in Figure 4 corresponds well with TOC values (table 1 in Part A).

3.1.6. Conditions in the palaeoenvironment

Climate, salinity, and redox potential are the main palaeoenvironmental proxies that control OM accumulation and preservation. The palaeoclimate is determined based on the C-value, and the Sr/Cu and Rb/Sr ratios; palaeosalinity is indicated by the Sr/Ba and Ca/(Ca + Fe) ratios, and REE distribution, while palaeoredox conditions are assessed by the EFs of Mo, U, V, Cu, and Ni, the V/(V + Ni) and V/Zn ratios, as well as by the Eu anomaly.

3.1.6.1. Climate

Most processes in the lacustrine depositional environment are controlled by climate, as it affects OM productivity, the influx of terrigenous material, and OM preservation during sediment formation [72, 73]. Consequently, according to some authors, climate can be a significant factor in the formation of OM-rich sediments (e.g. [6]).

The C-value is used to determine climate, since Fe, Mn, Cr, V, Ni, and Co are enriched in sedimentary rocks under humid climatic conditions, while Ca, Mg, K, Na, Sr, and Ba are representative of an arid climate [74, 75]. Most of the analysed samples have C-values between 0.21–0.39, suggesting semiarid conditions; the C-values for samples D1, D4, and D9 are in the range of 0.42–0.52, indicating semiarid–humid conditions, while the value for sample D2 (0.17) implies an arid climate (Table 1) [74, 75].

The Rb/Sr ratio is used to estimate palaeoclimate, since Rb precipitates and is adsorbed by clay minerals under humid conditions, whereas Sr is deposited with carbonates during dry periods [37, 76, 77]. Consequently, high values of the ratio indicate humid conditions, while low values reflect arid conditions. The majority of the samples have Rb/Sr ratios < 0.3, indicating semiarid conditions, whereas samples D1, D4, and D9 exhibit somewhat elevated values (0.34–0.53), reflecting semiarid–humid conditions, which is in accordance with the above-discussed C-value (Table 1).

The Sr/Cu ratio is based on the observation that the concentration of Sr increases under arid conditions, while the concentration of Cu rises under humid conditions. Accordingly, an elevated Sr/Cu ratio indicates a dry and warm climate [24, 78]. Most samples (D3, D5, D6, D10, D12, D14, D15) have Sr/Cu ratio values between 5–10, suggesting warm semiarid to semihumid conditions. Samples D1, D4, D7, D9, and D11 are characterised by a Sr/Cu ratio < 5, which indicates a warm and humid climate. However, in accordance with the above-discussed C-value and the Rb/Sr ratio, samples D1, D4, and D9 show the lowest Sr/Cu ratio values < 2.6, reflecting the highest palaeoenvironmental humidity within the studied sample set. On the other hand, samples D2, D8, D13, and D16 exhibit Sr/Cu ratio values > 10, indicating dry and hot conditions [41, 75, 79]. It should be noted that sample D16, which clearly differs from the rest, also displays the most significant difference in palaeoclimate proxy values (Rb/Sr = 0.04; Sr/Cu = 73.74; Table 1), implying the most pronounced aridity within the studied set.

The climate indices C-value, Rb/Sr, and Sr/Cu show significant correlations ($r = 0.91$, $p < 0.01$; $r = –0.89$, $p < 0.01$; $r = –0.85$, $p < 0.01$, respectively). Conversely, moderate correlations of these parameters with TOC contents in samples D1–D15 ($r = –0.51$, $p = 0.05$; $r = –0.55$, $p < 0.05$; $r = 0.67$, $p < 0.01$, respectively) are observed. This may imply that increased humidity caused a higher clastic influx, which contributed more to the decrease of OM concentration than to the increase in palaeobioproductivity (i.e. blooms of aquatic organisms). It is also documented by highly similar correlation coefficients ($r = 0.5–0.7$) between the climate proxies and TOC, as well as the S2/S3 ratio (derived from Rock-Eval data discussed in [16]), reflecting the relative input of aquatic vs terrestrial OM and thus the quality of OM to produce hydrocarbons.

3.1.6.2 Salinity

Salinity in the water column is one of the key factors that control the growth of organisms in lacustrine environments and the preservation of OM [80, 81].

The Sr/Ba ratio is commonly used to estimate palaeosalinity because Sr and Ba are sensitive to salinity variations and have different geochemical behaviour [6, 82, 83]. Sr is deposited directly from seawater, while Ba is easily adsorbed by clay minerals and fine clastic sediments [84, 85]. A high Sr concentration can be an indication of the inflow of seawater into the lake; therefore, the Sr/Ba ratio increases as water salinity rises. Most of the analysed samples have Sr/Ba > 1, which implies saline water, whereas samples D1, D4, D6, D7, and D9 have values < 1, which suggests fresh water [86, 87].

The Ca/(Ca + Fe) ratio also shows sensitivity to salinity changes [88]. Most samples have Ca/(Ca + Fe) ratio values ranging from 0.47 to 0.73, indicating brackish water. The exceptions are samples D1, D4, D7, and D9, which have values of this parameter < 0.40, suggesting a freshwater environment, and sample D16, which shows a value of 0.93, indicating saline water (Table 1) [72, 88]. This is in line with conclusions derived from biomarker proxies of the analysed samples (pristane/phytane ratio, gammacerane index, and the abundance of β-carotane), which indicate deposition of OM in a lacustrine alkaline brackish to freshwater environment under warm climatic conditions [16].

A good agreement between OM richness and salinity is observed (TOC vs Sr/Ba ratio: $r = 0.70$, $p < 0.01$; TOC vs Ca/(Ca + Fe) ratio: $r = 0.60$, $p < 0.05$, for samples D1–D15). Samples D2, D13, and D16, containing the highest TOC contents, exhibit the greatest values of both palaeosalinity proxies, whereas samples D1, D4, D6, and D7, with the lowest TOC contents (< 3%), were deposited under freshwater conditions (Table 1; table 1 in Part A). The most organic-rich sample, D16, again displays a notable difference from D1–D15, being characterised by evidently higher Sr/Ba and Ca/(Ca + Fe) ratios (4.68 and 0.93, respectively; Table 1), clearly indicating the influence of marine water. This observation is consistent with results from previous research, which also showed that during the deposition of sediments represented by D16, there was a marine inflow from the Paratethys Sea as a result of regional tilting of the area during the Lower Miocene [16].

Generally, salinity is controlled by climate, because the salinity of water increases under warm and arid conditions as a result of evaporation [89, 90]. This is also reflected within the studied sample set, since statistically significant correlations between the climate indices (C-value, Rb/Sr, Sr/Cu) and salinity proxies (Sr/Ba and Ca/(Ca + Fe)) are observed (r ranging from 0.84 to 0.94).

3.1.6.3 Redox conditions

According to some authors, anoxic conditions are the main factor regulating OM enrichment and fixation within sediments [80, 91]. Such settings are controlled by climatic and hydrographic conditions and can develop within stratified water columns due to salinity and/or temperature gradients [56]. TEs such as Cr, Ni, V, U, Th, Mo, Cu, and Co can be used as redox tracers because their oxidation state and solubility are influenced by the redox status of the palaeoenvironment [22, 56, 58, 92–94].

The analysed samples showed enrichment in Mo, U, V, Cu, Ni, and Zn (section 3.3 in Part A). The enrichment of these elements is typical of deposits formed under anoxic conditions and usually indicates that such conditions were associated with high palaeobioproductivity [7, 95]. The parameters V/(V + Ni) and V/Zn (Table 1) also indicate anoxic conditions in the depositional environment [62, 96, 97]. This agrees with conclusions drawn from biomarker proxies presented in previous studies [16, 17], which are also considered reliable indicators of redox conditions.

For more detailed monitoring, EFs for redox tracers [8, 56, 98] were calculated for each sample individually (Table 1). Interestingly, in most cases, the highest enrichment of these elements is found in samples D1, D4, and D7, which exhibit the lowest TOC contents (Table 1; table 1 in Part A). In contrast, the lowest EF values are observed for the most organic-rich sample, D16. Therefore, the obtained data may indicate that the lower TOC contents in samples D1, D4, and D7 were not caused by a change in anoxic redox conditions but rather by the dilution of OM concentration due to clastic influx (Section 3.1.5).

This interpretation is in accordance with biomarker redox proxies, which clearly indicate a stable water column level (i.e. anoxic settings) during the formation of samples D1–D15, as well as elevated values of the gammacerane index, associated with a steadily low pristane/phytane ratio, particularly in samples D1, D4, and D7 [16]. On the other hand, the lowest redox tracer EFs for sample D16 coincide with biomarker parameters implying a shallower but stratified and more saline calm water column [16], as well as with palaeoclimate indices indicating arid and warm climatic conditions (Section 3.1.6.1).

3.2. Integrative implications for the formation of organic-rich sediments in the Dubrava block

The characteristics of the lacustrine depositional environment affect the formation of organic-rich sediments and kerogen type, and therefore their potential to produce liquid hydrocarbons. These characteristics are recorded in the geochemical features of sediments and can be obtained from analyses of both organic and inorganic matter ([5, 60, 65, 99, 100] and references therein).

Both inorganic and organic data clearly show a notable difference in sample D16 (Fig. 5a) and certain differences among samples D1–D15 (Fig. 5b). Although D16 is the only sample of its type in the analysed series, it clearly reflects the transition from a swamp environment to a lacustrine one, as well as the geological evolution of the basin.

Sample D16 was formed just above the main coal seam, which indicates significant changes in sedimentary conditions. The main factors that induced this were probably tectonic activity and climate change, which have led to a transgression [31]. Sample D16 is characterised by the highest proportion of carbonate minerals (63.87 wt%; fig. 1 in Part A), the exclusive presence of the carbonate mineral aragonite and the sulphate mineral bassanite [16], and the absence of feldspar and zeolite group minerals (natrolite and analcime). It also shows lower concentrations of almost all TEs and REEs.

Geochemical data indicate differences in provenance and tectonic settings between sample D16 (more felsic) and samples D1–D15 (Sections 3.1.1 and 3.1.2), while D16 was not influenced by hydrothermal fluids (Section 3.1.3). Sample D16 is also characterised by higher palaeobioproductivity (the highest Ba/Al and Ba/Ti ratios; Section 3.1.4) and significantly lower detrital input (the highest Si/Al ratio and the lowest concentrations of constituents of clastic minerals and TEs; Section 3.1.5; sections 3.1.1 and 3.1.3 in Part A).

The salinity parameters (Sr/Ba, Ca/(Ca + Fe); Section 3.1.6.2) indicate marine water inflow into the lake. As mentioned, sample D16 has the highest content of carbonate minerals (fig. 1 in Part A), which are associated with an arid climate and alkaline environment [101]. Moreover, the enrichment in carbonate minerals also means that there was no substantial detrital or terrestrial material influx into the lake, which led not only to OM enrichment but also to the dilution of almost all TE and REE concentrations, except for Cs, Sr, Cr, and Ni [23]. The Sr enrichment is attributed to marine transgression and the formation of a large amount of the carbonate mineral aragonite [16].

Cr and Ni are redox-sensitive elements; hence, reducing conditions favoured their enrichment in sediments [57]. The high concentration of Ni can

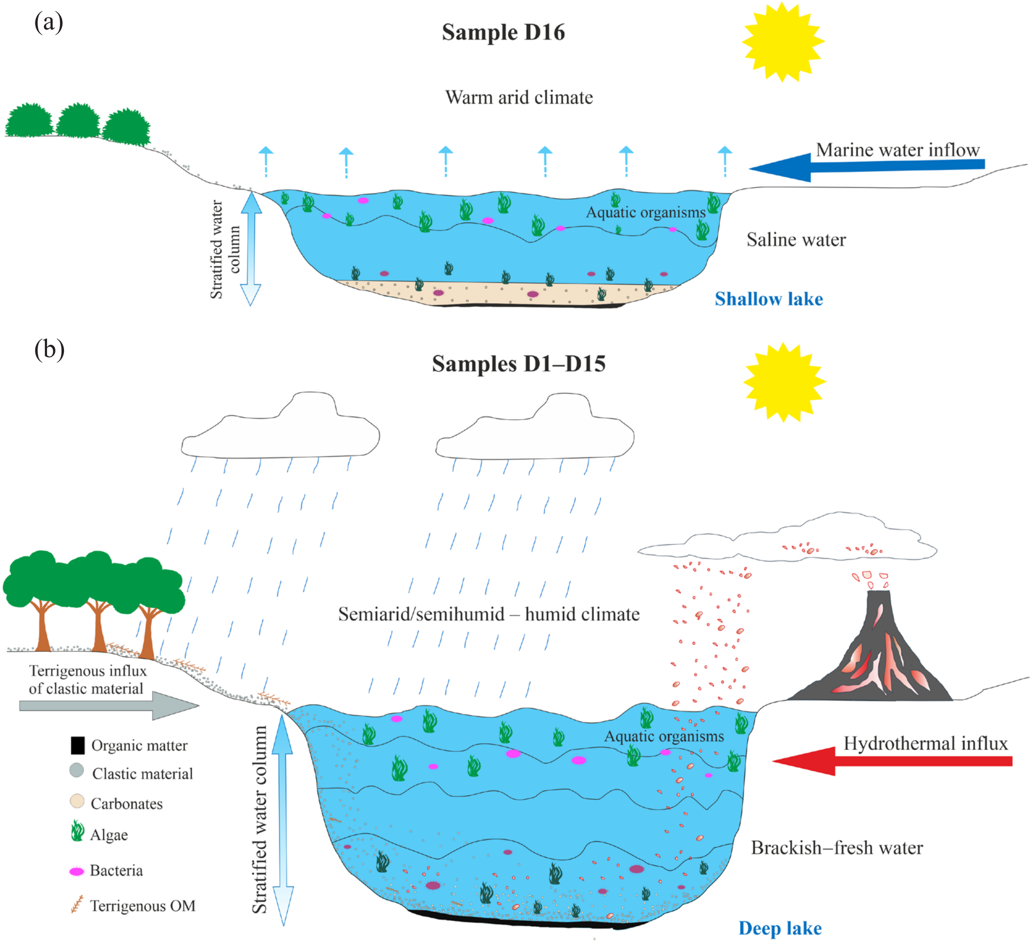

Fig. 5. Sketch illustrating the depositional environments during oil shale formation of (a) sample 16 and (b) samples D1–D15.

also originate from seawater inflow [102] and/or high OM flux [56], while a notably increased content of S can explain the enrichment of Cs in this sample only (6.11 wt%; table 1 in Part A) [103] and/or elevated water temperature [104].

During the formation of sediments represented by sample D16, the climate was warm and arid (Section 3.1.6.1; see also the presence of bassanite and aragonite in section 3.1.1 in Part A). Such conditions enhanced water evaporation, resulting in a lower water level, higher insolation, and weaker circulation within the water body, consequently favouring stratification. These conditions led to an anoxic environment at depth, which contributed to better OM preservation. Combined with high palaeobioproductivity (mainly favourable for the growth of algae and sulphur-reducing bacteria) and a low clastic input (minimising the dilution effect on OM concentration), this resulted in the highest TOC content.

All the above observations derived from the study of inorganic components are in accordance with the detailed characterisation of OM [16, 17]. The OM study also implied a calm alkaline environment and pointed out sudden ingressions of marine water into the basin. The water column was shallow but stratified due to the somewhat increased salinity and elevated temperature. Such conditions led to high palaeobioproductivity, significant deposition, and preservation of aquatic OM (mainly algae and bacterial remnants) [16, 17].

Additionally, it is well known (e.g. [105–107]) that the sudden mixing of a thermally stratified freshwater column, caused by sporadic storms or marine water ingressions, induces oxygen deprivation and/or salt stress. Such events cause environmental shock and mass mortality of aquatic biota due to their inability to adapt, thus promoting enhanced OM deposition at the sediment–water interface and the local formation of organic-rich layers. Consequently, any of the phenomena explained above can lead to the formation of sediments extremely rich in OM (TOC 29.10 wt%; table 1 in Part A), consisting of a mixture of oil-prone kerogen types I and II [16, 17].

After the deposition of sediments represented by sample D16, the lake deepened over time, probably due to further tectonic activity (Section 3.1.2) and climate change (still warm, but more humid climate; Section 3.1.6.1). Due to the semiarid/semihumid to humid climate, freshwater inflow into the lake occurred, leading to a rise in water level (brackish–fresh lake) that is usually accompanied by a higher terrigenous influx of clastic material. The clastic influx carried nutrients into the lake, causing blooms of aquatic organisms (mainly primary producers, such as green and brown algae, and bacteria) and increasing the sedimentation rate. Generally, a faster sedimentation rate contributes to better OM preservation but also leads to its reduced concentration due to dilution by clastic material [108]. Furthermore, the freshwater inflow into the lake resulted in a very low S content in samples D1–D15 (0.06–0.23 wt%; table 1 in Part A), compared with D16 (6.11 wt%).

As the lake is a dynamic system, during the formation of sedimentary rocks represented by samples D1–D15, there were fluctuations in bioproductivity, water column level, and stratification, which were consequence of changes in humidity, freshwater inflow, and hydrothermal and clastic influx. All these factors resulted in geochemical variations among samples D1–D15, grouping them into two subclusters. One subcluster (Ib) comprises samples D1, D4, D6, D7, and D9, whereas the second (Ia) includes the remaining samples, among which a slight distinction between samples D2 and D13 is observed, with more pronounced clustering of D13 (section 3.1.3 in Part A).

The samples of subcluster Ib are characterised by the lowest TOC contents (table 1 in Part A), a high content of clay minerals, a relatively high content of feldspar minerals, absence or very low content of quartz, the lowest amount of carbonate minerals (section 3.1.1 in Part A), high concentrations of REEs (section 3.1.4 in Part A), the highest humidity / the lowest salinity (Sections 3.1.6.1 and 3.1.6.2), and high clastic input (Section 3.1.5). This particularly applies to samples D4, D6, and D7, which show the highest influx of clastic terrigenous material, as indicated by the REE distributions (Section 3.1.1), kerogen type, and biomarkers [16]. The V/(V + Ni) and V/Zn ratios, EFs for redox tracers, and biomarker proxies (gammacerane index and pristane/phytane ratio; [16]) clearly imply anoxic redox conditions. Therefore, the lowering of TOC content in the samples of subcluster Ib can mostly be attributed to a decrease of OM concentration due to clastic influx (Section 3.1.5), rather than to a change in anoxic redox conditions. Furthermore, this also signifies that the reduced OM potential for liquid hydrocarbon generation in samples D4, D6, and D7 (i.e. the presence of type III kerogen; [16]) was mainly controlled by the clastic influx that resulted in an increased impact of allochthonous higher-plant biomass.

The samples from subcluster Ia are characterised by a substantial content of OM (with high hydrocarbon generation potential, i.e. kerogen types I and II), resulting from high palaeobioproductivity, further supported by hydrothermal fluids (as documented by the presence of analcime and natrolite and corresponding parameters; Section 3.1.3) and anoxic redox conditions (Section 3.1.6.3). A moderate clastic influx is observed. Both inorganic data and biomarker proxies suggest a relatively high and stable brackish water column, the stratification of which was supported by a warm semiarid/ semihumid climate.

Sample D13 differs from the other samples of subcluster Ia by a relatively higher TOC content (~13 wt%; table 1 in Part A), a higher content of carbonate minerals and quartz, a lower amount of feldspar and clay minerals, lower REE content, and a lower clastic input (Section 3.1.5; sections 3.1.1–3.1.3 in Part A). Among numerous parameters, the most evident distinguishing feature of sample D13 is its more pronounced aridity (Sections 3.1.6.1 and 3.1.6.2), which may have caused a lower clastic influx (similar to the case of sample D16), resulting in less OM dilution and a slight increase in alkalinity/ salinity. This calm, alkaline, arid environment was favourable for the deposition of carbonates, but also for the blooming of aquatic biota (increased nutrient concentration due to evaporation), as documented by the highest palaeobioproductivity index values (Section 3.1.4). Furthermore, the calm environment and warm conditions promoted water stratification and anoxic settings, contributing to good algal OM preservation. The obtained results are in accordance with OM proxies, which indicate the highest hydrocarbon generation potential and enrichment in precursor algal biomass in sample D13 (type I kerogen; [15–17]).

Finally, the slight separation of sample D2 (fig. 2 in Part A) can also be attributed to enhanced aridity and palaeobioproductivity. This sample showed almost equal values of ∑REEs (section 3.1.4 in Part A) and climate and salinity proxies as sample D13 (Sections 3.1.6.1 and 3.1.6.2). In addition, it is associated with the highest carbonate content (section 3.1.1 in Part A) and palaeobioproductivity parameters (Section 3.1.4), as well as the lowest content of MCEs and TCEs after sample D13 (Section 3.1.5), among the samples comprising subcluster Ia.

It should be noted that the classification of samples based on mineral composition and concentrations of major, trace, and rare earth elements, in addition to full accordance with Rock-Eval data and biomarker proxies, and a clear indication of the main factors causing differences in organic richness, also revealed thorough consistency with lithology (Table 1; fig. 2 in Part A).

4. Conclusions

A detailed inorganic geochemical characterisation of the Upper layer of Aleksinac oil shale in the Dubrava block was performed.

An andesite to felsic origin is presumed for the studied samples, with evident volcanic activity, also documented by the presence of zeolite group minerals (analcime and natrolite). Accordingly, sediment formation was influenced by hydrothermal fluids, which promoted the productivity of aquatic organisms and thus led to OM enrichment. The sediments developed in terrain with active continental margin characteristics and were built on a continental island arc, consistent with the complex tectonic settings of the Aleksinac deposit and its formation through fragmentation of two geotectonic units, the Carpatho-Balkanides and the Serbian–Macedonian Massif.

Palaeoenvironmental indicators derived from concentrations of major, trace, and rare earth elements showed good accordance with organic geochemical data from previous detailed studies, indicating deposition of the sediments in an anoxic lacustrine environment of variable salinity (from saline to freshwater) under warm, arid, and semiarid/semihumid climatic conditions. Such conditions favoured primary bioproductivity in the lake, whereas a stably stratified water column, with highly reducing bottom water, enhanced OM preservation.

Classification of the samples based on mineral composition and concentrations of major, trace, and rare earth elements resulted in two main clusters (I and II), showing a distinct separation of two subclusters within the first group. This classification revealed good accordance with Rock-Eval data, biomarker proxies, and lithology, clearly indicating the main factors that caused differences in organic richness.

Samples D1–D15, forming the first cluster, are characterised by variable contents of clays, feldspars, quartz, carbonates, TOC (~1–13 wt%), and S (0.06 0.23 wt%), as well as concentrations of trace and rare earth elements. Within this group, samples D1, D4, D6, D7, and D9, comprising subcluster Ib, clearly stand out from the remaining samples (subcluster Ia), based on the increased contents of all clastic constituents and rare earth elements, absence or very low content of quartz, the lowest amount of carbonate minerals, and the lowest TOC contents (~1–3 wt%).

The second cluster comprises sample D16, which notably differs from all other samples (D1–D15) and is the first sample deposited after the main coal seam. It is characterised by the highest content of carbonate minerals (63.87 wt%), OM (TOC 29.10 wt%), and S (6.11 wt%), the exclusive presence of the carbonate mineral aragonite and the sulphate mineral bassanite, the absence of feldspar and zeolite group minerals, and lower concentrations of almost all trace and rare earth elements (except Cs, Sr, Cr, and Ni). The greatest OM-enrichment in sample D16 resulted mainly from the warm and arid climate, and marine water ingressions, which created favourable conditions for primary producers, whereas the calm, alkaline, stratified anoxic water column contributed to excellent preservation of aquatic OM. Warm and arid conditions also minimised clastic input.

The main change in the depositional environment of the sediments represented by samples D1–D15 in relation to sample D16 occurred due to tectonic activity and climate change. A more humid (semiarid/semihumid, but still warm) climate, together with freshwater inflow into the lake, raised the water level (brackish–fresh lake, low S content), while maintaining the anoxic settings that promoted OM preservation, but also increasing the influx of clastic terrigenous material. Detailed analysis of palaeoenvironmental proxies, which showed accordance with biomarker parameters, clearly revealed that the lowering of TOC and the segregation of samples D1, D4, D6, D7, and D9 into a separate subcluster resulted from humid episodes that promoted clastic influx, rather than from changes in anoxic redox conditions. Furthermore, the lowering of OM potential for liquid hydrocarbon generation in samples D4, D6, and D7 (i.e. the presence of type III kerogen) was also mainly controlled by the clastic influx that resulted in the increased impact of allochthonous higher-plant biomass.

The obtained results represent valuable palaeoenvironmental records for the study area and can contribute to future exploration and utilisation of oil shale in the Aleksinac deposit.

Data availability statement

The data supporting the findings of this study are available within the article.

Acknowledgements

The study was financed by the Ministry of Education, Science and Technological Development of the Republic of Serbia (contract No. 451-03-136/2025-03/200168, project No. 451-03-136/2025-03/200026). We dedicate this paper to the memory of our colleague Prof. Dr Aleksandar Kostić, who passed away during the preparation of this manuscript. The publication costs of this article were partially covered by the Estonian Academy of Sciences.

References

1. Tissot, B. P., Welte, D. H. *Petroleum Formation and Occurrence*. 2nd ed. Springer-Verlag, Heidelberg, 1984.
2. Han, Y. W, Ma, Z. D., Zhang, H. F., Zhang, B. R., Li, F. L., Gao, S. et al. *Geochemistry*. Geological Publishing House, Beijing, 2003.
3. Aliyev, S. A., Sari, A. Organic material and trace elements of bituminous rocks in the Ozanköy Field, Ankara, Turkey. *Acta Geologica Sinica (English Edition)*, 2007, **81**(4), 658–667. https://doi.org/10.1111/j.1755–6724.2007.tb00989.x
4. Balaram, V. Rare earth elements: a review of applications, occurrence, exploration, analysis, recycling, and environmental impact. *Geoscience Frontiers*, 2019, **10**(4), 1285–1303. https://doi.org/10.1016/j.gsf.2018.12.005
5. Pedersen, T. F., Calvert, S. E. Anoxia vs. productivity: what controls the formation of organic-carbon-rich sediments and sedimentary rocks? *AAPG Bulletin*, 1990, **74**(4), 454–466. https://doi.org/10.1306/0C9B232B-1710-11D7-8645000102C1865D
6. Jia, J., Bechtel, A., Liu, Z., Strobl, S. A. I., Sun, P., Sachsenhofer, R. F. Oil shale formation in the Upper Cretaceous Nenjiang Formation of the Songliao Basin (NE China): implications from organic and inorganic geochemical analyses. *International Journal* of *Coal Geology*, 2013, **113**, 11–26. https://doi.org/10.1016/j.coal.2013.03.004
7. Song, Y., Liu, Z., Meng, Q., Xu, J., Sun, P., Cheng, L. et al. Multiple controlling factors of the enrichment of organic matter in the Upper Cretaceous oil shale sequences of the Songliao Basin, NE China: implications from geochemical analyses. *Oil Shale*, 2016, **33**(2), 142–166. https://doi.org/10.3176/oil.2016.2.04
8. Xu, S.-C., Hu, H.-B., Zhang, P., Wang, Q.-C., Kang, J., Miao, Q. Major and trace elements in mid-Eocene lacustrine oil shales of the Fushun Basin, NE China: concentration features and paleolimnological implications. *Marine and Petroleum Geology*, 2020, **121**, 104610. https://doi.org/10.1016/j.marpetgeo.2020.104610
9. Li, T.-J., Huang, Z.-L., Chen, X., Li, X.-N., Liu, J.-T. Paleoenvironment and organic matter enrichment of the Carboniferous volcanic-related source rocks in the Malang Sag, Santanghu Basin, NW China. *Petroleum Science*, 2021, **18**, 29–53. https://doi.org/10.1007/s12182-020-00514-1
10. Wu, Z., Zhao, X., Li, J., Pu, X., Tao, X., Shi, Z. et al. Paleoenvironmental modes and organic matter enrichment mechanisms of lacustrine shale in the Paleogene Shahejie Formation, Qikou Sag, Bohai Bay Basin. *Energy Reports*, 2021, **7**, 9046–9068. https://doi.org/10.1016/j.egyr.2021.11.228
11. Mallick, M., Banerjee, B., Hassan, T., Kumar, T. V., Babu, E. V. S. S. K., Krishna, K. et al. Geochemistry of Permian carbonaceous shales from Raniganj sub-basin, Damodar Valley, India: implications for provenance, weathering, tectonics and source of organic matter. *Applied Geochemistry*, 2022, **146**, 105469. https://doi.org/10.1016/j.apgeochem.2022.105469
12. Armstrong-Altrin, J. S., Ramos-Vázquez, M. A., Madhavaraju, J., Marca-

Castillo, M. E., Machain-Castillo, M. L, Márquez-García, A. Z. Geochemistry of marine sediments adjacent to the Los Tuxtlas volcanic complex, Gulf of Mexico: constraints on weathering and provenance. *Applied Geochemistry*, 2022, **141**, 105321. https://doi.org/10.1016/j.apgeochem.2022.105321

13. Ercegovac, M., Grgurović, D., Bajc, S., Vitorović, D. Oil shale in Serbia: geological and chemical-technological investigations, actual problems of exploration and feasibility studies. In *Mineral Material Complex of Serbia and Montenegro at the Crossings of Two Millenniums* (Vujić, S., ed.). Margo-Art, Belgrade, 2003, 368–378.
14. Jelenković, R., Kostić, A., Životić, D., Ercegovac, M. Mineral resources of Serbia. *Geologica Carpathica*, 2008, **59**(4), 345–361.
15. Gajica, G., Šajnović, A., Stojanović, K., Antonijević, M., Aleksić, N., Jovančićević, B. The influence of pyrolysis type on shale oil generation and its composition (Upper layer of Aleksinac oil shale, Serbia). *Journal of the Serbian Chemical Society*, 2017, **82**(12), 1461–1477. https://doi.org/10.2298/JSC170421064G
16. Gajica, G., Šajnović, A., Stojanović, K., Kostić, A., Slipper, I., Antonijević, M. et al. Organic geochemical study of the upper layer of Aleksinac oil shale in the Dubrava block, Serbia. *Oil Shale*, 2017, **34**(3), 197–218. https://doi.org/10.3176/oil.2017.3.01
17. Gajica, G., Šajnović, A., Stojanović, K., Schwarzbauer, J., Kostić, A., Jovančićević, B. A comparative study of the molecular and isotopic composition of biomarkers in immature oil shale (Aleksinac deposit, Serbia) and its liquid pyrolysis products (open and closed systems*). Marine and Petroleum Geology*, 2022, **136**, 105383. https://doi.org/10.1016/j.marpetgeo.2021.105383
18. McLennan, S. M., Hemming, S., McDaniel, D. K., Hanson, G. N. Geochemical approaches to sedimentation, provenance, and tectonics. In *Processes Controlling the Composition of Clastic Sediments* (Johnsson, M. J., Basu, A., eds). Geological Society of America, 1993, 21–40. https://doi.org/10.1130/SPE284-p21
19. Taylor, S. R., McLennan, S. M. The geochemical evolution of the continental crust. *Reviews of Geophysics*, 1995, **33**(2), 241–265. https://doi.org/10.1029/95RG00262
20. Hayashi, K.-I., Fujisawa, H., Holland, H. D., Ohmoto, H. Geochemistry of ~1.9 Ga sedimentary rocks from northeastern Labrador, Canada. *Geochimica et Cosmochimica Acta*, 1997, **61**(19), 4115–4137. https://doi.org/10.1016/S0016-7037(97)00214-7
21. Basu, A. Evolution of siliciclastic provenance inquiries: a critical appraisal. In *Sediment Provenance: Influences on Compositional Change from Source to Link* (Mazumder, R., ed.). Elsevier, Amsterdam, 2017, 5–23.
22. Fu, X., Wang, J., Feng, X., Chen, W., Wang, D., Song, C. et al. Mineralogical composition of and trace-element accumulation in lower Toarcian anoxic sediments: a case study from the Bilong Co. oil shale, eastern Tethys. *Geological Magazine*, 2016a, **153**(4), 618–634. https://doi.org/10.1017/S0016756815000758

23. Vosoughi Moradi, A., Sarı, A., Akkaya, P. Geochemistry of the Miocene oil shale (Hançili Formation) in the Çankırı-Çorum Basin, Central Turkey: implications for paleoclimate conditions, source–area weathering, provenance and tectonic setting. *Sedimentary Geology*, 2016, **341**, 289–303. https://doi.org/10.1016/j.sedgeo.2016.05.002
24. Li, Q., Wu, S., Xia, D., You, X., Zhang, H., Lu, H. Major and trace element geochemistry of the lacustrine organic-rich shales from the Upper Triassic Chang 7 Member in the southwestern Ordos Basin, China: implications for paleoenvironment and organic matter accumulation. *Marine and Petroleum Geology*, 2020, **111**, 852–867. https://doi.org/10.1016/j.marpetgeo.2019.09.003
25. Boynton, W. V. Cosmochemistry of the rare earth elements: meteorite studies. In *Rare Earth Element Geochemistry* (Henderson, P., ed.). Elsevier, Amsterdam, 1984, 63–114.
26. Taylor, S. R., McLennan, S. M. *The Continental Crust: Its Composition and Evolution*. Blackwell Scientific Publications, Oxford, 1985.
27. McLennan, S. M. Relationships between the trace element composition of sedimentary rocks and upper continental crust. *Geochemistry, Geophysics, Geosystems*, 2001, **2**(4), 2000GC00010. https://doi.org/10.1029/2000GC000109
28. Han, S., Zhang, Y., Huang, J., Rui, Y., Tang, Z. Elemental geochemical characterization of sedimentary conditions and organic matter enrichment for Lower Cambrian shale formations in northern Guizhou, South China. *Minerals*, 2020, **10**(9), 793. https://doi.org/10.3390/min10090793
29. Godoy, L. H., de Souza Sardinha, D. S., Torres Moreno, M. M. Major and trace elements redistribution in weathered claystones from the Corumbataí Formation, Paraná Sedimentary Basin, São Paulo, Brazil. *Brazilian Journal of Geology*, 2017, **47**(4), 615–632. https://doi.org/10.1590/2317-4889201720170086
30. Kašanin-Grubin, M. *Sedimentology of the Oil Shales Series of the Aleksinac Basin.* M.S. thesis. University of Belgrade, Serbia, 1996.
31. Obradović, J., Vasić, N. *Jezerski baseni u neogenu Srbije*. Srpska akademija nauka i umetnosti, Beograd, 2007.
32. Hay, R. L., Sheppard, R. A. Occurrence of zeolites in sedimentary rocks: an overview. *Reviews in Mineralogy and Geochemistry*, 2001, **45**(1), 217–234. https://doi.org/10.2138/rmg.2001.45.6
33. Wang, Q., Bai, J., Ge, J., Wei, Y., Li, S. Geochemistry of rare earth and other trace elements in Chinese oil shale. *Oil Shale*, 2014, **31**(3), 266–277. https://doi.org/10.3176/oil.2014.3.06
34. Bai, Y., Lv, Q., Liu, Z., Sun, P., Xu, Y., Meng, J. et al. Major, trace and rare earth element geochemistry of coal and oil shale in the Yuqia area, Middle Jurassic Shimengou Formation, northern Qaidam Basin. *Oil Shale*, 2020, **37**(1), 1–31. https://doi.org/10.3176/oil.2020.1.01
35. Cullers, R. L., Graf, J. L. Rare earth elements in igneous rocks of the continental crust: intermediate and silicic rocks – ore petrogenesis. In *Rare Earth Element Geochemistry* (Henderson, P., ed.). Elsevier, Amsterdam, 1984, 275–312.
36. Xu, J.-B., Cheng, B., Deng, Q., Liang, Y.-G., Faboya, O. L., Liao, Z.-W.

Distribution and geochemical significance of trace elements in shale rocks and their residual kerogens. *Acta Geochimica*, 2018, **37**, 886–900. https://doi.org/10.1007/s11631-018-0297-0

37. Bai, Y., Liu, Z., Sun, P., Liu, R., Hu, X., Zhao, H. et al. Rare earth and major element geochemistry of Eocene fine-grained sediments in oil shale- and coal-bearing layers of the Meihe Basin, Northeast China. *Journal* of *Asian Earth Sciences*, 2015, **97**, 89–101. https://doi.org/10.1016/j.jseaes.2014.10.008
38. Bhatia, M. R. Composition and classification of Paleozoic flysch mudrocks of eastern Australia: implications in provenance and tectonic setting interpretation. *Sedimentary Geology*, 1985, **41**(2–4), 249–268. https://doi.org/10.1016/0037-0738(84)90065-4
39. Bhatia, M. R., Crook, K. A. W. Trace element characteristics of graywackes and tectonic setting discrimination of sedimentary basins. *Contributions to Mineralogy and Petrology*, 1986, **92**, 181–193. https://doi.org/10.1007/BF00375292
40. Roser, B. P., Korsch, R. J. Determination of tectonic setting of sandstone-mudstone suites using SiO_2 content and K_2O/Na_2O ratio. *The Journal of Geology*, 1986, **94**(5), 635–650. https://doi.org/10.1086/629071
41. Liu, B., Song, Y., Zhu, K., Su, P., Ye, X., Zhao, W. Mineralogy and element geochemistry of salinized lacustrine organic-rich shale in the Middle Permian Santanghu Basin: implications for paleoenvironment, provenance, tectonic setting and shale oil potential. *Marine and Petroleum Geology*, 2020, **120**, 104569. https://doi.org/10.1016/j.marpetgeo.2020.104569
42. Grizelj, A., Peh, Z., Tibljaš, D., Kovačić, M., Kurečić, T. Mineralogical and geochemical characteristics of Miocene pelitic sedimentary rocks from the south-western part of the Pannonian Basin System (Croatia): implications for provenance studies. *Geoscience Frontiers*, 2017, **8**(1), 65–80. https://doi.org/10.1016/j.gsf.2015.11.009
43. Marović, M., Djoković, I., Pešić, L., Radovanović, S., Toljić, M., Gerzina, N. Neotectonics and seismicity of the southern margin of the Pannonian basin in Serbia. *EGU Stephan Mueller Special Publication Series*, 2002, **3**, 277–295. https://smsps.copernicus.org/articles/3/277/2002/
44. Dimitrijević, M. D. *Geologija Jugoslavije (Geology of Yugoslavia)*. Geological Institute–GEMINI, Belgrade, 1997.
45. Zhang, W. Z., Yang, H., Li, J. F., Ma, J. Leading effect of high-class source rock of Chang 7 in Ordos Basin on enrichment of low permeability oil-gas accumulation – hydrocarbon generation and expulsion mechanism. *Petroleum Exploration and Development*, 2006, **33**(3), 289–293.
46. Westall, F., Campbell, K. A., Bréhéret, J. G., Foucher, F., Gautret, P., Hubert, A. et al. Archean (3.33 Ga) microbe-sediment systems were diverse and flourished in a hydrothermal context. *Geology*, 2015, **43**(7), 615–618. https://doi.org/10.1130/G36646.1
47. Cronan, D. S. *Underwater Minerals*. Academic Press, London, 1980.
48. Pelleter, E., Fouquet, Y., Etoubleau, J., Cheron, S., Labanieh, S., Josso, P. et al.

Ni-Cu-Co-rich hydrothermal manganese mineralization in the Wallis and Futuna back-arc environment (SW Pacific). *Ore Geology Reviews*, 2017, **87**, 126–146. https://doi.org/10.1016/j.oregeorev.2016.09.014

49. Liu, H., Wang, C., Li, Y., Deng, J., Deng, B., Feng, Y. et al. Geochemistry of the black rock series of lower Cambrian Qiongzhusi Formation, SW Yangtze Block, China: reconstruction of sedimentary and tectonic environments. *Open Geosciences*, 2021, **13**(1), 166–187. https://doi.org/10.1515/geo-2020-0228
50. Toth, J. R. Deposition of submarine crusts rich in manganese and iron. *GSA Bulletin*, 1980, **91**(1), 44–54. https://doi.org/10.1130/0016-7606(1980)91<44:DOSCRI>2.0.CO;2
51. Wang, Z., Li, W., Wang, J., Wei, H., Fu, X., Song, C. et al. Controls on organic matter accumulation in marine mudstones from the Lower Permian Zhanjin Formation of the Qiangtang Basin (Tibet), eastern Tethys. *Marine and Petroleum Geology*, 2022, **138**, 105556. https://doi.org/10.1016/j.marpetgeo.2022.105556
52. Alderton, D. Zeolites. In *Encyclopedia of Geology*, *2nd ed.* (Alderton, D., Elias, S. A., eds). Academic Press, London, 2021, 313–325. https://doi.org/10.1016/B978-0-08-102908-4.00041-2
53. Dekov, V. M., Darakchieva, V. Y., Billström, K., Garbe-Schönberg, C. D., Kamenov, G. D., Gallinari, M. et al. Element enrichment and provenance of the detrital component in Holocene sediments from the western Black Sea. *Oceanologia*, 2020, **62**(2), 139–163. https://doi.org/10.1016/j.oceano.2019.10.001
54. Dymond, J., Suess, E., Lyle, M. Barium in deep-sea sediment: a geochemical proxy for paleoproductivity. *Paleoceanography and Paleoclimatology*, 1992, **7**(2), 163–181. https://doi.org/10.1029/92PA00181
55. Ferriday, T., Montenari, M. Chemostratigraphy and chemofacies of source rock analogues: a high-resolution analysis of black shale successions from the lower Silurian Formigoso Formation (Cantabrian Mountains, NW Spain). In *Stratigraphy & Timescales* (Montenari, M., ed.). Elsevier Science, Amsterdam, 2016, 123–255.
56. Tribovillard, N., Algeo, T. J., Lyons, T. W., Riboulleau, A. Trace metals as paleoredox and paleoproductivity proxies: an update. *Chemical Geology*, 2006, **232**(1–2), 12–32. https://doi.org/10.1016/j.chemgeo.2006.02.012
57. Goldberg, K., Humayun, M. 2016. Geochemical palaeoredox indicators in organic-rich shales of the Irati Formation, Permian of the Paraná Basin, southern Brazil. *Brazilian Journal of Geology*, 2016, **46**(3), 377–393. https://doi.org/10.1590/2317-4889201620160001
58. Algeo, T. J., Maynard, J. B. Trace-element behaviour and redox facies in core shales of Upper Pennsylvanian Kansas-type cyclothems. *Chemical Geology*, 2004, **206**(3–4), 289–318. https://doi.org/10.1016/j.chemgeo.2003.12.009
59. Murphy, A. E., Sageman, B. B., Hollander, D. J., Lyons, T. W., Brett, C. E. Black shale deposition and faunal overturn in the Devonian Appalachian Basin: clastic starvation, seasonal water-column mixing, and efficient biolimiting nutrient recycling. *Paleoceanography and Paleoclimatology*, 2000, **15**(3), 280–291. https://doi.org/10.1029/1999PA000445

60. Zhao, J., Jin, Z., Jin, Z., Geng, Y., Wen, X., Yan, C. Applying sedimentary geochemical proxies for paleoenvironment interpretation of organic-rich shale deposition in the Sichuan Basin, China. *International Journal of Coal Geology*, 2016, **163**, 52–71. https://doi.org/10.1016/j.coal.2016.06.015
61. Yamamoto, K. Geochemical characteristics and depositional environments of cherts and associated rocks in the Franciscan and Shimanto Terranes. *Sedimentary Geology*, 1987, **52**(1–2), 65–108. https://doi.org/10.1016/0037-0738(87)90017-0
62. Rimmer, S. M. Geochemical paleoredox indicators in Devonian–Mississippian black shales, Central Appalachian Basin (USA). *Chemical Geology*, 2004, **206**(3–4), 373–391. https://doi.org/10.1016/j.chemgeo.2003.12.029
63. Brumsack, H.-J. The trace metal content of recent organic carbon-rich sediments: implications for Cretaceous black shale formation. *Palaeogeography, Palaeoclimatology, Palaeoecology*, 2006, **232**(2–4), 344–361. https://doi.org/10.1016/j.palaeo.2005.05.011
64. Nagarajan, R., Madhavaraju, J., Nagendra, R., Armstrong-Altrin, J. S., Moutte, J. Geochemistry of Neoproterozoic shales of the Rabanpalli Formation, Bhima Basin, Northern Karnataka, southern India: implications for provenance and paleoredox conditions. *Revista Mexicana de Ciencias Geológicas*, 2007, **24**(2), 150–160.
65. Ross, D. J. K., Bustin, R. M. Investigating the use of sedimentary geochemical proxies for paleoenvironment interpretation of thermally mature organic-rich strata: examples from the Devonian–Mississippian shales, Western Canadian Sedimentary Basin. *Chemical Geology*, 2009, **260**(1–2), 1–19. https://doi.org/10.1016/j.chemgeo.2008.10.027
66. Sajid, Z., Ismail, M. S., Zakariah, M. N. A., Tsegab, H., Gámez Vintaned, J. A., Hanif, T. et al. Impact of paleosalinity, paleoredox, paleoproductivity/preservation on the organic matter enrichment in black shales from Triassic turbidites of Semanggol Basin, Peninsular Malaysia. *Minerals*, 2020, **10**(10), 915. https://doi.org/10.3390/min10100915
67. Kidder, D. L., Erwin, D. H. Secular distribution of biogenic silica through the Phanerozoic: comparison of silica-replaced fossils and bedded cherts at the series level. *The Journal of Geology*, 2001, **109**(4), 509–522. https://doi.org/10.1086/320794
68. Magnall, J. M., Gleeson, S. A., Paradis, S. The importance of siliceous radiolarian-bearing mudstones in the formation of sediment-hosted Zn-Pb ± Ba mineralization in the Selwyn Basin, Yukon, Canada. *Economic Geology*, 2015, **110**(8), 2139–2146. https://doi.org/10.2113/econgeo.110.8.2139
69. Liang, Y., Zhang, J., Liu, Y., Tang, X., Li, Z., Ding, J. et al. Evidence for biogenic silica occurrence in the Lower Silurian Longmaxi Shale in southeastern Chongqing, China. *Minerals*, 2020, **10**(11), 945. https://doi.org/10.3390/min10110945
70. Qin, J., Tao, G., Teng, G. Hydrocarbon-forming organisms in excellent marine source rocks in South China. *Petroleum Geology & Experiment*, 2010, **32**(3), 262–269. https://doi.org/10.11781/sysydz201003262

71. Wu, C., Tuo, J., Zhang, M., Liu, Y., Xing, L., Gong, J., Qiu, J. Multiple controlling factors of lower Palaeozoic organic-rich marine shales in the Sichuan Basin, China: evidence from minerals and trace elements. *Energy Exploration & Exploitation*, 2017, **35**(5), 627–644. https://doi.org/10.1177/0144598717709667
72. Zhang, M., Liu, Z., Xu, S., Sun, P., Hu, X. Element response to the ancient lake information and its evolution history of argillaceous source rocks in the Lucaogou Formation in Sangonghe area of southern margin of Junggar Basin. *Journal of Earth Science*, 2013, **24**, 987–996. https://doi.org/10.1007/s12583-013-0392-4
73. Ma, L., Zhang, Z., Meng, W. Climate-provenance effect on the organic matter enrichment of the Chang 9 source rocks in the Central Ordos Basin, China. *Geofluids*, 2021, **2021**(1), 1233879. https://doi.org/10.1155/2021/1233879
74. Zhao, Z. Y., Zhao, J. H., Wang, H. J., Liao, J. D., Liu, C. M. Distribution characteristics and applications of trace elements in Junggar Basin. *Natural Gas Exploration and Development*, 2007, **30**, 30–33.
75. Wang, J.-X., Sun, P.-C., Liu, Z.-J., Li, Y.-J. Characteristics and genesis of lacustrine laminar coal and oil shale: a case study in the Dachanggou Basin, Xinjiang, Northwest China. *Marine and Petroleum Geology*, 2021, **126**, 104924. https://doi.org/10.1016/j.marpetgeo.2021.104924
76. Jin, Z. D., Zhang, E. L. Paleoclimate implications of Rb/Sr ratios from lake sediments. *Science and Technology Engineering*, 2002, **2**(3), 20–22.
77. Zuo, X., Li, C., Zhang, J., Ma, G., Chen, P. Geochemical characteristics and depositional environment of the Shahejie Formation in the Binnan Oilfield, China. *Journal of Geophysics and Engineering*, 2020, **17**(3), 539–551. https://doi.org/10.1093/jge/gxaa013
78. Lerman, A. *Lakes: Chemistry, Geology, Physics*. Springer, New York, 1978.
79. Armstrong-Altrin, J., Lee, Y. I., Kasper-Zubillaga, J. J., Trejo-Ramírez, E. Mineralogy and geochemistry of sands along the Manzanillo and El Carrizal beach areas, southern Mexico: implications for palaeoweathering, provenance and tectonic setting. *Geological Journal*, 2017, **52**(4), 559–582. https://doi.org/10.1002/gj.2792
80. Tenger, B., Liu, W., Xu, Y., Gao, C., Hu, K., Gao, C. Comprehensive geochemical identification of highly evolved marine hydrocarbon source rocks: organic matter, paleoenvironment and development of effective hydrocarbon source rocks. *Chinese Journal of Geochemistry*, 2006, **25**, 333–340. https://doi.org/10.1007/s11631-006-0332-4
81. Wei, Y., Li, X., Zhang, R., Li, X., Lu, S., Qiu, Y. et al. Influence of a paleosedimentary environment on shale oil enrichment: a case study on the Shahejie Formation of Raoyang Sag, Bohai Bay Basin, China. *Frontiers of Earth Science*, 2021, **9**, 736054. https://doi.org/10.3389/feart.2021.736054
82. Liu, Y. J., Cao, L. M., Li, Z. L., Wang, H. N., Chu, T. Q., Zhang, J. R. *Element Geochemistry*. Science Press, Beijing, 1984.
83. Torres, M. E., Brumsack, H. J., Bohrmann, G., Emeis, K. C. Barite fronts in continental margin sediments: a new look at barium remobilization in the

zone of sulfate reduction and formation of heavy barites in diagenetic fronts. *Chemical Geology*, 1996, **127**(1–3), 125–139. https://doi.org/10.1016/0009-2541(95)00090-9

84. Reimann, C., Caritat, P. *Chemical Elements in the Environment*. Springer, Berlin, 1998.
85. Xu, B., Ding, S., Wang, Y., Liu, Q. F. Geochemical characteristics of illite clay rocks from the Shihezi Formation in the Hanxing mining area and its sedimentary environment. *Mining Science and Technology (China)*, 2011, **21**(4), 495–500. https://doi.org/10.1016/j.mstc.2011.06.006
86. Deng, H. W., Qian, K. *Sedimentary Geochemistry and Environment Analysis*. Gansu Technology Publishing House, Lanzhou, 1993.
87. Sun, Z. C., Yang, P., Zhang, Z. H. *Sedimentary Environment and Hydrocarbon Generation of China Cenozoic Salty Lacustrine Facies*. Petroleum Industry Press, Beijing, 1997.
88. Lan, X. H., Ma, D. X., Xu, M. G., Zhou, Q. W., Zhang, G. W. Some geochemical signs and their importance for sedimentary facies. *Marine Geology & Quaternary Geology*, 1987, **7**(1), 39–49.
89. Zheng, R. C., Liu, M. Q. Study on paleosalinity of Chang-6 oil reservoir set in Ordos Basin. *Oil and Gas Geology*, 1999, **20**(1), 20–25.
90. Meng, Q. T., Liu, Z. J., Bruch, A. A., Liu, R., Hu, F. Palaeoclimatic evolution during Eocene and its influence on oil shale mineralisation, Fushun basin, China. *Journal* of *Asian Earth Sciences,* 2012, **45**, 95–105. https://doi.org/10.1016/j.jseaes.2011.09.021
91. Hunt, J. M. *Petroleum Geochemistry and Geology*. W. H. Freeman and Company, San Francisco, 1979.
92. Holland, H. D. *The Chemistry of the Atmosphere and the Oceans*. Wiley-Interscience, New York, 1978.
93. Morford, J. L., Russell, A. D., Emerson, S. Trace metal evidence for changes in the redox environment associated with the transition from terrigenous clay to diatomaceous sediment, Saanlich Inlet, BC. *Marine Geology*, 2001, **174**(1–4), 355–369. https://doi.org/10.1016/S0025-3227(00)00160-2
94. Li, Y., Wang, Z., Gan, Q., Niu, X., Xu, W. Paleoenvironmental conditions and organic matter accumulation in Upper Palaeozoic organic-rich rocks in the east margin of the Ordos Basin, China. *Fuel*, 2019, **252**, 172–187. https://doi.org/10.1016/j.fuel.2019.04.095
95. Hetzel, A., März, C., Vogt, C., Brumsack, H.-J. Geochemical environment of Cenomanian–Turonian black shale deposition at Wunstorf (northern Germany). *Cretaceous Research*, 2011, **32**(4), 480–494. https://doi.org/10.1016/j.cretres.2011.03.004
96. Jones, B., Manning, D. A. C. Comparison of geochemical indices used for the interpretation of palaeoredox conditions in ancient mudstones. *Chemical Geology*, 1994, **111**(1–4), 111–129. https://doi.org/10.1016/0009-2541(94)90085-X
97. Wang, Z., Fu, X., Feng, X., Song, C., Wang, D., Chen, W. et al. Geochemical features of the black shales from the Wuyu Basin, southern Tibet: implications

for palaeoenvironment and palaeoclimate. *Geological Journal*, 2017, **52**(2), 282–297. https://doi.org/10.1002/gj.2756

98. Sun, Y.-Z., Jinxi, W., Shifeng, L., Kankun, J., Mingyue, L. Mechanism of uranium accumulation in the Kupferschiefer from Poland and Germany. *Energy Exploration & Exploitation*, 2005, **23**(6), 463–473. https://doi.org/10.1260/014459805776986902
99. Chen, R., Sharma, S., Bank, T., Soeder, D., Eastman, H. Comparison of isotopic and geochemical characteristics of sediments from a gas- and liquids-prone wells in Marcellus Shale from Appalachian Basin, West Virginia. *Applied Geochemistry*, 2015, **60**, 59–71. https://doi.org/10.1016/j.apgeochem.2015.01.001
100. Khan, M. Z., Feng, Q., Zhang, K., Guo, W. Biogenic silica and organic carbon fluxes provide evidence of enhanced marine productivity in the Upper Ordovician-Lower Silurian of South China. *Palaeogeography, Palaeoclimatology, Palaeoecology*, 2019, **534**, 109278. https://doi.org/10.1016/j.palaeo.2019.109278
101. Li, Y., Wang, N., Li, Z., Zhou, X., Zhang, C., Wang, Y. Carbonate formation and water level changes in a paleo-lake and its implication for carbon cycle and climate change, arid China. *Frontiers of Earth Science*, 2013, **7**, 487–500. https://doi.org/10.1007/s11707-013-0392-9
102. Glikson, M., Chappell, B. W., Freeman, R. S., Webber, E. Trace elements in oil shales, their source and organic association with particular reference to Australian deposits. *Chemical Geology*, 1985, **53**(1–2), 155–174. https://doi.org/10.1016/0009-2541(85)90028-2
103. Fu, X., Wang, J., Zeng, Y., Tan, F., Feng, X. Concentration and mode of occurrence of trace elements in marine oil shale from the Bilong Co area, northern Tibet, China. *International Journal of Coal Geology*, 2011, **85**(1), 112–122. https://doi.org/10.1016/j.coal.2010.10.004
104. Chowdhury, A. N., Handa, B. K., Das, A. K. High lithium, rubidium and cesium contents of thermal spring water, spring sediments and borax deposits in Puga valley, Kashmir, India. *Geochemical Journal*, 1974, **8**(2), 61–65. https://doi.org/10.2343/geochemj.8.61
105. Fleet, A. J., Kelts, K., Talbot, M. R. *Lacustrine Petroleum Source Rocks*. Geological Society of London, Special Publications No. 40, London, 1988.
106. Katz, B. J. Factors controlling the development of lacustrine petroleum source rocks – an update. In *Paleogeography, Paleoclimate, and Source Rocks* (Huc, A.-Y., ed.). American Association of Petroleum Geologists, Studies in Geology 40, 1995, 61–79.
107. Rosen, B. H., Loftin, K. A., Graham, J. L., Stahlhut, K. N., Riley, J. M., Johnston, B. D. et al. *Understanding the Effect of Salinity Tolerance on Cyanobacteria Associated With a Harmful Algal Bloom in Lake Okeechobee, Florida*. U.S. Geological Survey Scientific Investigations Report, 2018, 2018–5092, 32. https://doi.org/10.3133/sir20185092
108. Schwarzbauer, J., Jovančićević, B. *Fossil Matter in the Geosphere*. Springer, Heidelberg, 2015.

Oil Shale, 2026, 43, 1, 104–116 https://doi.org/10.3176/oil.2026.1.05

Ionic liquids, [EMIM]Cl and [BMIM]SCN for sulfur removal from shale oils

Omar S. Al-Ayed[(a)]*, Rasha A. Hajarat[(b)], Khaled M. A. Khalil[(a)], Deya M. M. Alshadfan[(a)], Khaled H. M. Daoud[(a)], Wesam J. Abu-Jamil[(a)], Omar. M. S. Alhajjeh[(a)], Dua'a M. R. Al-Aqtam[(a)]

[(a)] Department of Chemical Engineering, Faculty of Engineering Technology, Al-Balqa Applied University, Amman Marka 11134, Jordan
[(b)] Department of Chemical Engineering, Mutah University, Karak 61710, Jordan

Received 19 September 2025, accepted 23 January 2026, available 29 January 2026

Abstract. *Oil shales from Attarat and Sultani were pyrolyzed at 550 °C to produce shale oils for the present study. The organic sulfur content of the two shale oils was determined to be 9.3 and 10.5 wt.%, respectively. Two ionic liquids (IL), 1-ethyl-3-methylimidazolium chloride ([EMIM]Cl) and 1-butyl-3-methylimidazolium thiocyanate ([BMIM]SCN), were used in liquid–liquid extraction for desulfurization. The extraction process was carried out at room temperature. The liquid–liquid extraction resulted in two-phase formation and redistribution of sulfur compounds into the aqueous IL-rich phase and the shale oil phase. The hydrocarbon sulfur weight percent was determined using a CHNSO analyzer. The removal efficiency for Sultani and Attarat shale oils with [EMIM]Cl was calculated to be 52.4 and 58.1 wt.%, respectively. When [BMIM]SCN was employed for the extraction of sulfur compounds from Sultani and Attarat shale oils, removal efficiencies of 43.8 and 52.4 wt.% were achieved, respectively. When the surfactant T-80 was added to Sultani shale oil and heated to 60 °C, followed by addition of [EMIM]Cl, the extraction efficiency decreased to 40.9 wt.%. On the other hand, when the mixture of shale oil and IL was heated to 60 °C before adding T-80, the weight percent removal increased to 58.1%.*

Keywords: *shale oil, ionic liquid, desulfurization, Attarat, IL/oil ratio.*

1. Introduction

In general, sulfur species in crude oils/fuels are a major issue during refining and cause air pollution, which ultimately endangers public health. Particulate emissions, processing equipment, corrosion of equipment, catalyst poisoning/

---

* Corresponding author, omar.alayed@bau.edu.jo

deactivation, transportation, and storage of fuels are affected by the presence of sulfur compounds in their different forms. Hydrodesulfurization (HDS) is the conventional method of sulfur removal from crude oils or distilled fractions [1]. Alternative methods to HDS have been developed, such as oxidation. In oxidative desulfurization, the sulfur compounds in fuel are oxidized to sulfoxides in a slow reaction step, then to sulfones in a fast reaction step, which are then removed through liquid extraction [2, 3], precipitation and adsorption [4], extraction [5], and alkylation, in which the boiling point of the organosulfur compounds is increased by alkylation of thiophene with olefins, thus increasing the molecular weight to allow separation by distillation [6].

Kerogen is the organic-bearing material in oil shale composition that is also known to generate organometallic compounds [7]. Shale oil includes the known classes of hydrocarbons, as well as heteroatoms such as sulfur, nitrogen, and oxygen, in addition to metals [8–11]. The sulfur content of Jordanian shale oil can be as high as 9.0–12.0 wt.% [12]. Baird et al. [13] and Järvik et al. [14] studied the shale oil sulfur content generated from kukersite oil shale and reported sulfur content in the range of 0.4–1.2 wt.%. These authors compiled and summarized works of several researchers who employed standard hydrotreating and more advanced methods to remove sulfur, nitrogen, and oxygen organometallic compounds from shale oil. On the other hand, Rang et al. [15] discussed non-hydrodesulfurization processes, including extraction, oxidation, and adsorption, as advanced methods used to deeply desulfurize liquid fuels, reducing sulfur content to less than 50 ppm.

The sulfur content of Chinese shale oil was reported as high as 2.19 wt.% [16]. Brazilian shale oil from the Irati location contained as low as 1.0 wt.% sulfur [17]. Sulfur in shale oil is present in different forms, such as mercaptans, thiophenes, their derivatives, and also sulfides or disulfides in the lighter fractions of shale oil.

One of the recent advanced methods to remove sulfur from fuels/shale oils is the use of ionic liquids (IL). Some of these ILs have the ability to perform liquid–liquid desulfurization LLD) and oxidative desulfurization, removing the most recalcitrant compounds present in fuels/shale oils. Compounds such as thiophene, benzothiophene, dibenzothiophene, and smaller molecular weight sulfur compounds can leave the oil phase and migrate to the aqueous phase containing ILs [18]. Researchers have reported that the migration of sulfur compounds is achieved through the formation of hydrogen bonding and dipole–dipole interactions, in addition to π–π stacking interactions between the sulfur compounds in fuels and ILs [19]. ILs in the aqueous phase containing the extracted sulfur compounds can be regenerated and recycled, improving the economics of LLD [20].

The role of ILs in removing sulfur compounds from crude oils and/or fractions such as gasoline, kerosene, diesel, and others has been attracting attention for decades. The ease of availability of these solvents to remove sulfur compounds and aromatics has made them popular among researchers.

ILs such as 1-butyl-3-methylimidazolium thiocyanate ([BMIM]SCN) were used to extract dibenzothiophene and aromatics from base oil, in which certain amounts of naphthalene and dibenzothiophene were dissolved [21]. The extractions results showed that 92.0 wt.% of the dibenzothiophene was removed under the experimental optimum extraction conditions, such as temperature and IL/oil ratio. In extractive desulfurization [22], the removal efficiency of dibenzothiophene from n-dodecane model oil was 86.5% at 30 °C, with an IL/oil mass ratio of 1:1 after 30 min. An IL, 1-ethyl-3-methylimidazolium chloride ([EMIM]Cl), was used as an extractant with a model oil (dodecane) containing dibenzothiophene as the sulfur compound [23]. The extraction of the model sulfur compound dibenzothiophene was reported to be 99 wt.%. The researchers also conducted regeneration of the spent IL via toluene back-extraction.

Using ILs in shale oil LLD has not been investigated thoroughly yet. In some cases, the weight percent of sulfur present in shale oil is much higher than that of crude oils or distilled fractions such as gasoline, kerosine, diesel, and fuel oils. Due to the higher sulfur mass percent in shale oils, it is difficult to refine shale oils in ordinary refineries. The shale oil content of heteroatoms/organometallic compounds must be reduced, or the shale oil must be hydrotreated to reduce the share of these compounds to permissible limits for possible distillation in crude oil refineries.

In general, few experimental tests have been performed by mixing ILs with real shale oil to extract sulfur/nitrogen compounds. ILs such as [BMIM]SCN, in addition to others, have been tested for extracting basic and neutral nitrides from Fushun shale oil in China [24]. Recently, in a separate study, ILs, i.e., [EMIM]Cl and [BMIM]SCN, were used to extract sulfur compounds from shale oil generated by pyrolyzing Jordanian Attarat shale oil [25]. The objective of the present work is the extraction of sulfur compounds present in real shale oil obtained by pyrolyzing oil shale at 550 °C from two different locations, Attarat and Sultani. The generated shale oils were tested for sulfur extraction using two ILs.

2. Materials and methods

2.1. Oil shale pyrolysis

The targeted locations were the Attarat Um-Alghudran area (31°16′08″ N 36°26′52″ E) and the Sultani mine in the Al-Hissa location (30.7705° N 35.8761° E). Oil shale samples were crushed and sieved to the desired size, 8 mm, using the British Standard Sieves system. This section of experimental work was initiated by destructive distillation (pyrolysis) of shale oil under inert nitrogen conditions, at temperature up to 550 °C. For each oil shale sample, a mass of 400 g was placed in the retort and pyrolyzed at 550 °C until no more shale oil was condensed. This part of the work generated the shale oil required for IL extraction experiments.

The produced shale oil was separated from the retorted water using a separatory funnel. The bottom water layer was taken and discarded, while the top shale oil layer was used for the liquid–liquid extraction experiments.

2.2. Liquid–liquid extraction of shale oil

The second part of the experiment was the extraction of sulfur compounds with [EMIM]Cl (purchased from Thermo Fisher Scientific, catalog No. 354091000, CAS No. 79917-90-1, HPLC ≥98%, water ≤1.0, molecular weight = 174.67, solid) and [BMIM]SCN (purchased from Thermo Fisher Scientific, catalog No. H59493.06, CAS No. 331717-63-6, proton NMR 97.5% min., water <0.26%, molecular weight = 169.25, pale yellow liquid). The extraction of sulfur compounds from shale oil using ILs was also employed at two levels: the stand-alone level and pretreatment of shale oil with a surfactant (Tween-80, nonionic, polyoxyethylene surfactant, Thermo Fisher Scientific, catalog No. 28329, light yellow liquid, concentration 10.3%, pH = 7.59, detergent grade). The treatment steps resulted in two separate phases: a shale oil phase and an aqueous phase containing the ILs and extracted sulfur compounds.

Both phases were subjected to total sulfur determination. In the present work, only the mass of sulfur in the two phases was of interest, since these represent the total sulfur content of the shale oil.

One gram of shale oil was weighed and mixed with one gram of ILs, resulting in an IL/oil ratio of 1:1. The mixing process was conducted at room temperature; this part of the experiment was performed for both shale oil samples and both types of ILs used. To study the effect of heating, two procedures were applied: heating a mixture of IL and shale oil prior to the addition of surfactant, and heating a mixture of shale oil and surfactant before the addition of ILs. Heating was performed at 60 °C using a water bath. The heated mixture was allowed to cool and separate into two phases. The removed total sulfur was determined using a Euro Vector 3000 CHNSO elemental analyzer.

2.3. Surfactant heating treatment

In this section of the experiment, the effect of mixture heating was investigated. The surfactant was added to the shale oil and IL mixture at less than 0.1 wt.% to avoid emulsion formation. Two types of treatment were tested in this part of the work. In the first trial, the surfactant was added to the mixture before heating in a water bath, i.e., at room temperature, followed by mixing and phase separation. In the second trial, the mixture of shale oil/surfactant and shale oil/IL was placed in the water bath for 3 h at 60 °C before the addition of IL or surfactant, respectively, to induce phase separation. These experiments were conducted in conjunction with distilled water for dilution of additives and facilitation of extract and raffinate separation. This step was performed to investigate the influence of surfactants on the viscosity of shale oil and their role in reducing surface tension during the extraction of sulfur from shale oil in the presence of ILs.

3. Results and discussion

The mass balance of Attarat and Sultani oil shale pyrolysis runs indicated that more than 10% of the oil shale samples by weight were converted to shale oil. Experimental runs were conducted in a stainless steel retort. The produced shale oil was used for sulfur determination before and after IL treatment. The test results showed that the total sulfur in Attarat and Sultani oil shales was 9.3 and 10.5 wt.%, respectively. A single GC–MS analysis run of a shale oil sample from Attarat showed the presence of several sulfur compounds, including, thiophene, 2,5-dimethylthiophene, 3,4-dimethylthiophene, 2,3-dimethylthiophene, 2,3,4-trimethylthiophene, 3,4-diethylthiophene, 2,5-diethylthiophene, benzothiophenes, 2-methylbenzothiophene, and other thiophene derivatives.

Liquid–liquid extraction with ILs allowed the arbitrary redistribution of sulfur compounds from shale oil into two phases. One phase was IL-rich, containing the extracted sulfur compounds, and the other was shale oil-rich. Sulfur content determination was performed for both phases. The efficiency of the extraction process was calculated based on the original sulfur weight measured in the shale oil before liquid–liquid extraction. The weight of sulfur in each phase, i.e., the IL-rich phase (aqueous phase) and the shale oil-rich phase, were determined for efficiency calculations.

3.1. Sultani shale oil

The results of sulfur compound extraction using [BMIM]SCN and [EMIM]Cl are depicted in Figure 1. Figure 1 shows three results: the sulfur content of the freshly produced shale oil, shown by the column on the left graph under the title “Shale oil,” is 10.5 wt.%. The weight percent sulfur found in the [BMIM]SCN aqueous extract (AQL) is depicted in the middle column of the upper graph as 4.6 wt.%. The right-hand column indicates the weight percent sulfur remaining in the shale oil phase after extraction, measured as 6.1 wt.%. The lower graph depicts similar results using [EMIM]Cl. As shown, the use of [EMIM]Cl resulted in 5.5 wt.% sulfur. The efficiency of the extraction process was calculated to be 43.8% and 52.4% using [BMIM]SCN and [EMIM]Cl, respectively. As can be seen, [EMIM]Cl is a better extraction agent for sulfur compounds than [BMIM]SCN. It should be noted that the sulfur content of the [BMIM]SCN IL was not deducted from the total sulfur measured in the

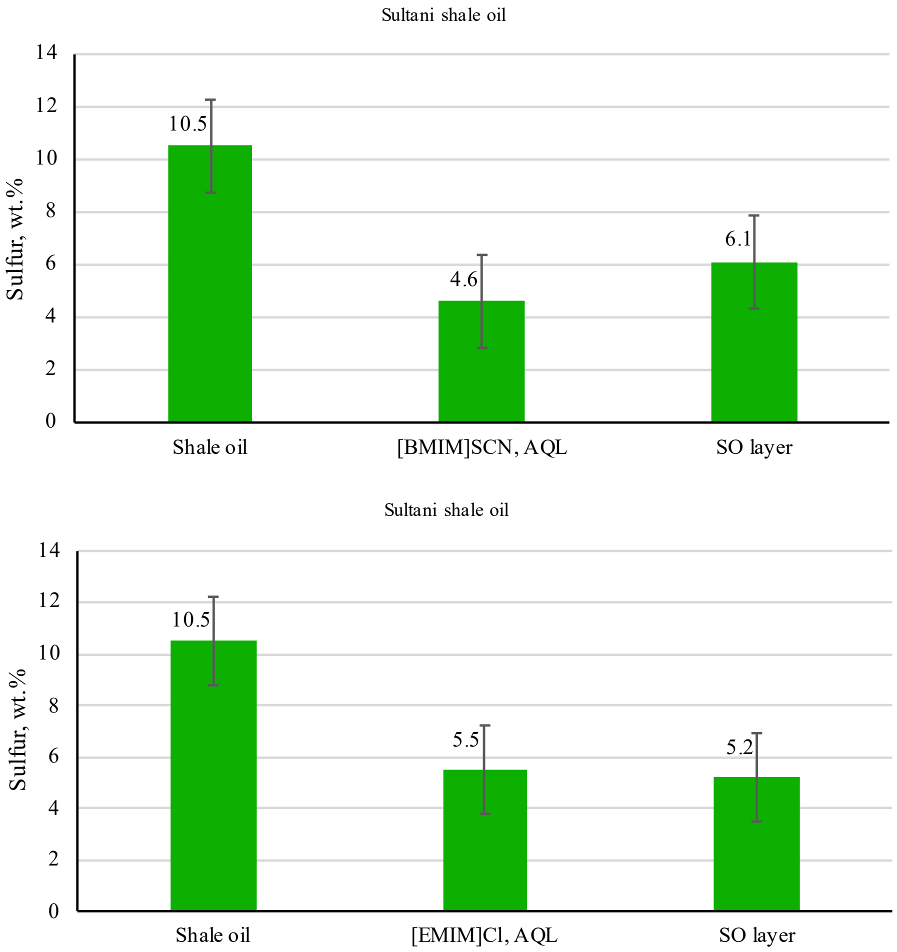

Fig. 1. Sulfur wt.% distribution in [BMIM]SCN aqueous extract (AQL) and shale oil (SO) layer.

[BMIM]SCN AQL, which may lead to an increase in removal efficiency. The unextracted sulfur remained at 6.1 and 5.2 wt.% in the shale oil layer after extraction with [BMIM]SCN and [EMIM]Cl, respectively.

3.2. Attarat shale oil

One gram of shale oil was weighed and mixed with one gram of IL to give a ratio of 1:1. The mixing process was conducted at room temperature. The formed mixture was mixed thoroughly. This part of the experiment was performed for both shale oil samples and both ILs used. The mixture was allowed 10–15 min to separate into two phases. The results of sulfur extraction from the original shale oil and the layers formed after extraction are depicted in Figure 2. The upper graph represents extraction with [BMIM]SCN, and the lower graph corresponds to [EMIM]Cl results.

The results depicted in Figure 2 show that the extracted sulfur wt.% in the [BMIM]SCN AQL was 4.9 wt.% (left graph), whereas the aqueous layer formed with [EMIM]Cl resulted in 5.4 wt.% sulfur extraction (right graph). These values indicate that 52.3 and 58.1 wt.% removal efficiency were achieved by the [BMIM]SCN and [EMIM]Cl ILs, respectively. These calculated efficiencies are higher than the corresponding removal efficiencies calculated for Sultani shale oil. These differences could be attributed to the nature of the sulfur components present in the shale oils. It should also be noted that the sulfur content of the [BMIM]SCN was not accounted for during sulfur weight percent calculations due to the nature of CHNSO analysis. The sulfur remaining in the shale oil-rich phase (SO layer), as shown in the rightmost column in Figure 2, was 4.6 and 4.3 wt.% for [BMIM]SCN and [EMIM]Cl, respectively.

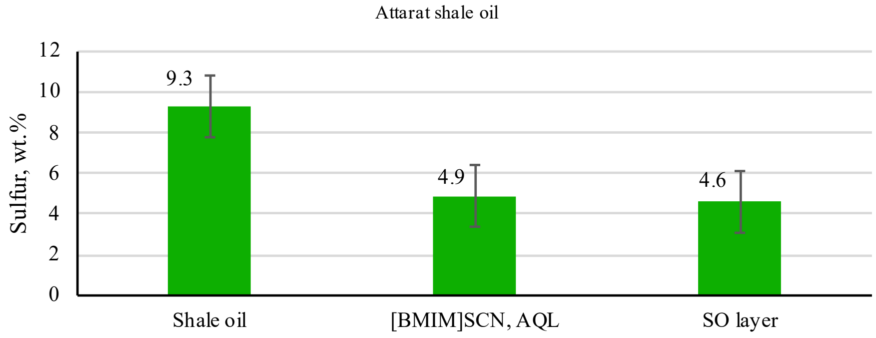

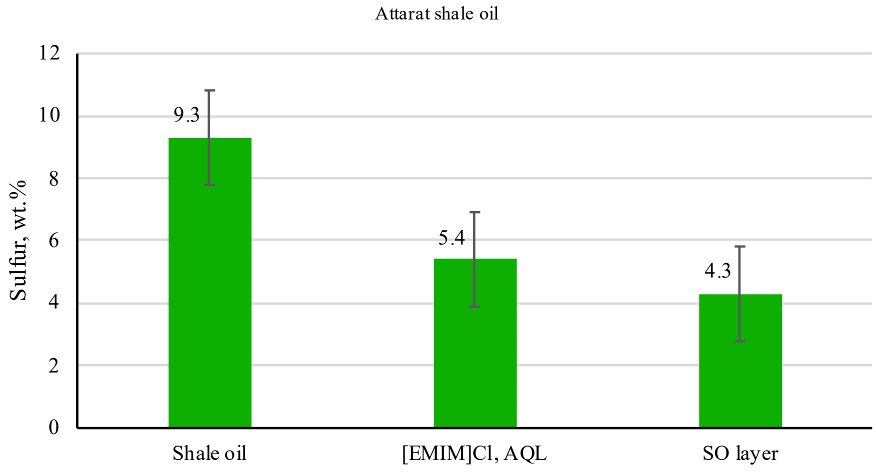

Fig. 2. Sulfur wt.% distribution after treatment with [BMIM]SCN and [EMIM]Cl.

3.3. Surfactants and heating roles

After discussing the findings of mixing ILs with shale oils, the effect of adding surfactants such as Tween-80 (T-80) was investigated. The importance of the surfactant lies in its impact on surface tension forces [26]. Shale oil is more viscous than normal crude oils; unfortunately, no reliable experimental data on viscosity measurements are reported in the literature, and it was not possible to measure viscosity in the present work.

The effect of surfactant addition to Sultani shale oil in the presence of different ILs is depicted by comparing Figures 1 and 3. As can be calculated from both figures, the addition of T-80 in the presence of [BMIM]SCN as an extraction agent increased the removal weight percent from 4.6 wt.% (Fig. 1)

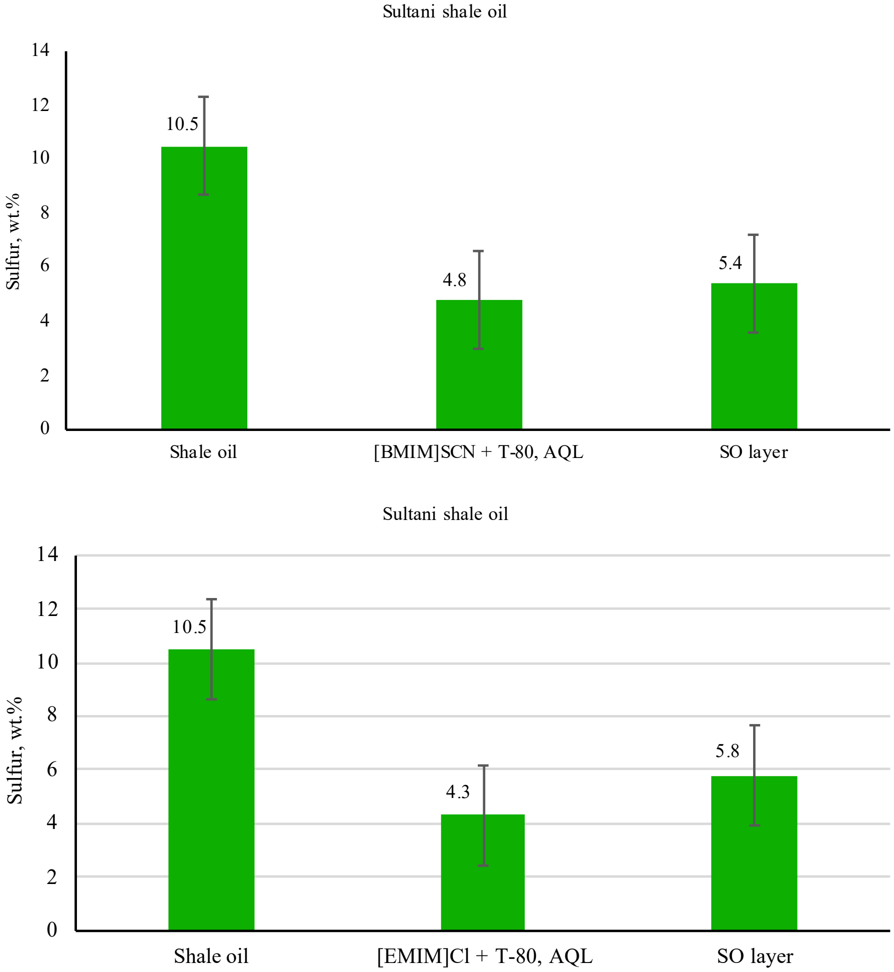

Fig. 3. Sulfur content in AQL and SO layers after adding surfactant T-80 to shale oil and ILs mixture.

to 4.8 wt.% (Fig. 3), i.e., a 4.3% increase in removal efficiency. Similarly, when the surfactant aided the extraction process in the case of [EMIM]Cl, the weight percent of sulfur removal decreased from 5.5 wt.% (Fig. 1) to 4.3 wt.% (Fig. 3), i.e., a 21.8% decrease. This indicates interactions between shale oil, the type of IL, and T-80 during the extraction process. Further investigations are required to explain the nature and type of these interactions.

The interactions of adding T-80 to shale oil and to the shale oil–IL mixture is presented in Figure 4. The T-80 effect was investigated in two cases: in the first case, T-80 was added to shale oil, followed by heating at 60 °C for 2.5 h in a water bath before adding the IL; in the second case, IL was added to shale oil, heated at 60 °C in a water bath for 2.5 h before adding T-80. The first case represents the interactions of T-80 with shale oil alone at 60 °C before IL intervention, while the second case represents the interactions of IL with shale oil at 60 °C before the addition of T-80. It should be noted here that there is a combined effect of heating and extraction at higher temperature compared with room-temperature extraction. Further investigations into these interactions are recommended.

The effect of [EMIM]Cl and T-80 was tested in the present work. As shown in Figure 4, heating shale oil with T-80 at 60 °C before adding [EMIM]Cl to the mixture resulted in 4.3 wt.% out of 10.5 wt.% from the original shale oil (AQL phase), i.e., 40.9% extraction efficiency compared with 5.5 wt.% extraction before heating and without the addition of T-80. This amounts to a reduction of 11.48% in removal efficiency. This behavior is likely due to T-80 being a nonionic surfactant with strong emulsifying and wetting ability. Unfortunately, we cannot ascribe this result to either the effect of temperature or surfactant addition. Similar studies [27] on crude oil and different ILs showed a decrease in extraction efficiency, when the temperature increased from room temperature to 60 °C, from 21% to 15%. These findings clearly support the possibility of decreased extraction efficiency due to increased temperature. This observation is in agreement with the findings of Mohammed et al. [27].

On the other hand, when shale oil and IL were mixed and heated, followed by the addition of T-80, the sulfur removed was 6.1 wt.%, corresponding to 58.1% removal efficiency. This must be compared with the results without heating and without the addition of T-80, in which 5.5 wt.% of sulfur was removed from 10.5 wt.% shale oil, indicating a removal efficiency of 52.38%, i.e., a 5.7% decrease. However, the change in removal efficiency results from the combination of heating, surfactant addition, and extraction at higher temperature. More work is needed to isolate the individual effects of temperature increase and surfactant addition on sulfur removal efficiency. Accordingly, no clear effect can be deduced in this study.

The interaction of surfactants (T-80) indicates direct interactions between IL and sulfur-containing hydrocarbons of shale oil under the influence of temperature. The decrease in extraction percentage in the presence of T-80 could be due to interactions between the IL and the surfactant and/or the effect

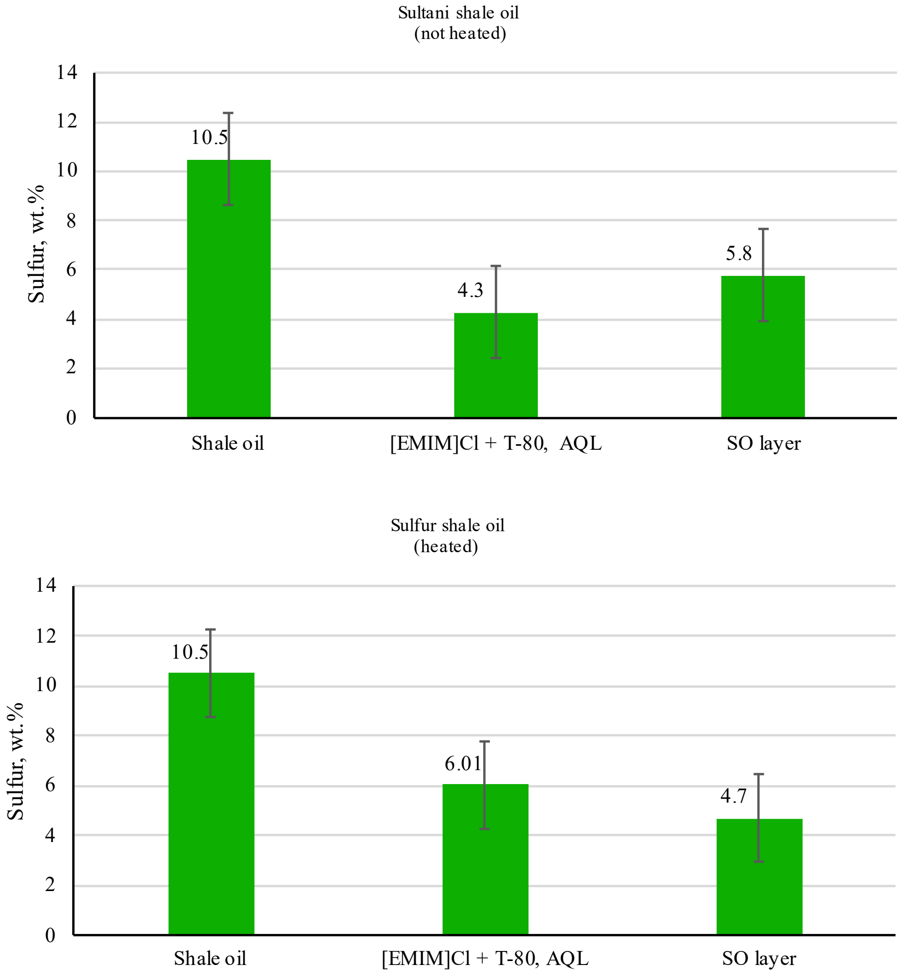

Fig. 4. Effect of heating on sulfur content in AQL with T-80 and mixture of shale oil and ILs.

of increased extraction temperature. Extraction with [EMIM]Cl in the presence of T-80 shows a decrease of sulfur in the AQL phase from 5.5 to 4.3 wt.%, i.e., a 21.8% reduction. This result could be ascribed to interactions between T-80 and [EMIM]Cl at higher temperatures than room temperature. T-80 can hydrogen-bond to Cl^- or coordinate to $EMIM^+$, leading to breaking ion–ion contacts and loosening the ionic network, which lowers viscosity [24] and can improve extraction mechanism and process efficiency, while temperature has the opposite effect [27]. Gao et al. [24] reported that denitrogenation of shale oil decreased with temperatures above 50 °C. This result aligns with the present findings. More work is needed on the effect of temperature on the extraction efficiency, equilibrium values, and the recyclability of ILs.

4. Conclusions

The extraction of sulfur compounds from shale oil is feasible using the two tested ionic liquids. 1-ethyl-3-methylimidazolium chloride ([EMIM]Cl) and 1-butyl-3-methylimidazolium thiocyanate ([BMIM]SCN) were found to be effective in sulfur removal. The extraction ability of [BMIM]SCN is less pronounced than that of [EMIM]Cl. More than 50% removal efficiency can be achieved. Extraction temperature plays a significant role in the extraction process. The Tween-80 surfactant contributes to the extraction, but a thorough investigation is required to understand the mechanism and the different interactions between sulfur components in shale oil, ionic liquids, and surfactants such as Triton-X100. Further research will focus on using other ionic liquids under different operation conditions and evaluating the recyclability of the ionic liquids for extraction.

Data availability statement

Data are contained within the article.

Acknowledgments

The authors gratefully acknowledge the Jordan Atomic Energy Commission, Analytical Chemistry Laboratories, for their assistance with experimental analyses. The publication costs of this article were covered by the Estonian Academy of Sciences.

References

1. Wang, Y., Hua, M., Zhou, S., Hu, D., Liu, F., Cheng, H. et al. Regulating the coordination environment of surface alumina on NiMo/Al_2O_3 to enhance ultra-deep hydrodesulfurization of diesel. *Applied Catalysis B: Environment and Energy*, 2024, **357**, 124265. https://doi.org/10.1016/j.apcatb.2024.124265
2. Bhutto, A. W., Abro, R., Gao, S., Abbas, T., Chen, X., Yu, G. Oxidative desulfurization of fuel oils using ionic liquids: a review, *Journal of the Taiwan Institute of Chemical Engineers*, 2016, **62**, 84–97. https://doi.org/10.1016/j.jtice.2016.01.014
3. Ahmed, H. R., Ealias, A. M., George, G. Advanced oxidation processes for desulfurization: a review of heterogeneous catalytic systems. *Journal of Industrial and Engineering Chemistry*, 2025, **150**, 231–246. https://doi.org/10.1016/j.jiec.2025.03.044
4. Haruna, A., Aljunid Merican, Z., Musa, S. G., Abubakar, S. Sulfur removal technologies from fuel oil for safe and sustainable environment. *Fuel*, 2022, **329**, 125370. https://doi.org/10.1016/j.fuel.2022.125370
5. Betiha, M. A., Rabie, A. M., Ahmed, H. S., Abdelrahman, A. A., El-Shahat, M. F.

Oxidative desulfurization using graphene and its composites for fuel containing thiophene and its derivatives: an update review. *Egyptian Journal of Petroleum*, 2018, **27**(4), 715–730. https://doi.org/10.1016/j.ejpe.2017.10.006

6. Babich, I. V., Moulijn, J. A. Science and technology of novel processes for deep desulfurization of oil refinery streams: a review. *Fuel*, 2003, **82**(6), 607–631. https://doi.org/10.1016/S0016-2361(02)00324-1
7. Maaten, B., Järvik, O., Pihl, O., Konist, A., Siirde, A. Oil shale pyrolysis products and the fate of sulfur. *Oil Shale*, 2020, **37**(1), 51–69. https://doi.org/10.3176/oil.2020.1.03
8. Baird, Z. S., Rang, H., Oja, V. Desulfurization, denitrogenation and deoxygenation of shale oil. *Oil Shale*, 2021, **38**(2), 137–154. https://doi.org/10.3176/oil.2021.2.03
9. Dijkmans, T., Djokic, M. R., Van Geem, K. M., Marin, G. B. Comprehensive compositional analysis of sulfur and nitrogen containing compounds in shale oil using GC×GC – FID/SCD/NCD/TOF-MS. *Fuel*, 2015, **140**, 398–406. https://doi.org/10.1016/j.fuel.2014.09.055
10. Abu-Nameh, E. S. M., Al-Ayed, O. S., Jadallah, A. Determination of selected elements in shale oil liquid. *Oil Shale*, 2019, **36**(2S), 179–187. https://doi.org/10.3176/oil.2019.2S.08
11. Al-Harahsheh, A., Al-Ayed, O., Al-Harahsheh, M., Abu-El-Halawah, R. Heating rate effect on fractional yield and composition of oil retorted from El-lajjun oil shale. *Journal of Analytical and Applied Pyrolysis*, 2010, **89**(2), 239–243. https://doi.org/10.1016/j.jaap.2010.08.009
12. Al-Ayed, O. S., Matouq, M. Factors affecting sulfur reactions in high sulfur oil shale pyrolysis. *Journal of Energy Resources Technology*, 2009, **131**(1), 012501. https://doi.org/10.1115/1.3068338
13. Baird, Z. S., Oja, V., Järvik, V. The composition of kukersite shale oil. *Oil Shale*, 2023, **40**(1), 25–43. https://doi.org/10.3176/oil.2023.1.02
14. Järvik, O., Baird, Z. S., Rannoveski, R., Oja, V. Properties of kukersite shale oil. *Oil Shale*, 2021, **38**(4), 265–294. https://doi.org/10.3176/oil.2021.4.01
15. Rang, H., Kann, J., Oja, V. Advances in desulfurization research of liquid fuel. *Oil Shale*, 2006, **23**(2), 164–176. https://doi.org/10.3176/oil.2006.2.09
16. Wang, Q., Liu, Q., Wang, Z. C., Liu, H. P., Bai, J. R., Ye, J. B. Characterization of organic nitrogen and sulfur in the oil shale kerogens. *Fuel Processing Technology*, 2017, **160**, 170–177. https://doi.org/10.1016/j.fuproc.2017.02.031
17. Afonso, J. C., Cardoso, J. N., Schmal, M. Distribution and origin of organic sulphur compounds in Irati shale oil. *Fuel*, 1992, **71**(4), 409–415. https://doi.org/10.1016/0016-2361(92)90030-R
18. Pham, D. D., Nguyen, T. M., Ho, T. H., Le, Q. V., Nguyen, D. L. T. Advancing hydrodesulfurization in heavy oil: recent developments, challenges, and future prospects. *Fuel*, 2024, **372**, 132082. https://doi.org/10.1016/j.fuel.2024.132082
19. Player, L. C., Bun, C., Lui, M. Y., Masters, A. F., Maschmeyer, T. Toward an understanding of the forces behind extractive desulfurization of fuels with ionic liquids. *ACS Sustainable Chemistry & Engineering*, 2019, **7**(4), 4087–4093. https://doi.org/10.1021/acssuschemeng.8b05585

20. Jiang, Z., Wang, X., Deng, H., Zhao, J., Li, Y. Molecular mechanism and experimental study of fuel oil extractive desulfurization technology based on ionic liquid. *Journal of the Energy Institute*, 2024, **112**, 101452. https://doi.org/10.1016/j.joei.2023.101452
21. Al Kaisy, G. M. J., Mutalib, M. I. A., Bustam, M. A., Leveque, J.-M., Muhammad, N. Liquid-liquid extraction of aromatics and sulfur compounds from base oil using ionic liquids. *Journal of Environmental Chemical Engineering*, 2016, **4**(4), Part A, 4786–4793. https://doi.org/10.1016/j.jece.2016.11.011
22. Dharaskar, S. A., Wasewar, K. L., Varma, M. N., Shende, D. Z. Synthesis, characterization, and application of 1-butyl-3-methylimidazolium thiocyanate for extractive desulfurization of liquid fuel. *Environmental Science and Pollution Research*, 2016, **23**, 9284–9294. https://doi.org/10.1007/s11356-015-4945-1
23. Anugwom, I., Mäki-Arvela, P., Salmi, T., Mikkola, J.-P. Ionic liquid assisted extraction of nitrogen and sulphur-containing air pollutants from model oil and regeneration of the spent ionic liquid. *Journal of Environmental Protection*, 2011, **2**(6), 796–802. http://dx.doi.org/10.4236/jep.2011.26091
24. Gao, S., Fang, S., Song, R., Chen, X., Yu, G. Extractive denitrogenation of shale oil using imidazolium ionic liquids. *Green Energy & Environment*, 2020, **5**(2), 173–182. https://doi.org/10.1016/j.gee.2020.04.002
25. Al-Daradka, M. M. A., Al-Ayed, O. S., Abu-Nameh, E. S. M. Removal of sulfur-containing compounds from shale oil using ionic liquids. *Jordanian Journal of Engineering and Chemical Industries*, 2025, **8**(2), 129–135. https://doi.org/10.48103/jjeci8142025
26. Nazar, M., Shah, M. U. H., Yahya, W. Z. N., Goto, M., Moniruzzaman, M. Surface active ionic liquid and Tween-80 blend as an effective dispersant for crude oil spill remediation. *Environmental Technology & Innovation*, 2021, **24**, 101868. https://doi.org/10.1016/j.eti.2021.101868
27. Mohammed, M. Y., Albayati, T. M., Ali, A. M. Imidazoliumbased ionic liquids for extraction of sulfur compounds from real heavy crude oil. *Chemistry Africa*, 2022, **5**, 1715–1722. https://doi.org/10.1007/s42250-022-00447-9

PUBLISHER
Estonian Academy Publishers
Kohtu 6
10130 Tallinn, ESTONIA
info@eap.ee
www.eap.ee

EDITORIAL OFFICE
Kohtu 6
10130 Tallinn, ESTONIA
hedi.tonso@eap.ee
www.eap.ee/oilshale

Subscription information is available at www.eap.ee/subscription

Subscription orders should be sent to subscription@eap.ee

ISBN 0208 189X (print)
ISSN 1736-7492 (electronic)

9 770208 189005